

1

Triplet Emitters for Organic Light-Emitting Diodes: Basic Properties

Hartmut Yersin* and Walter J. Finkenzeller

1.1

Introduction

Within the past decade, organo-transition metal compounds consisting of triplet emitters have become highly attractive, in particular, due to their applicability in electro-luminescent devices such as organic light-emitting diodes (OLEDs). With this new technology, efficient light-emitting systems are evolving. For example, in the future it will become possible to fabricate large and brilliant flat panel displays at a moderate price, to prepare illuminating wallpapers, and micro displays for all types of application. One important requirement for all of these applications is low power consumption and high efficiency of the light-emitting devices. Here, the organo-transition metal compounds offer a great advantage. The maximum obtainable efficiency may be a factor of *four* higher than for purely organic emitter materials. Thus, many research groups, both from academic and industrial laboratories, have become interested in this challenging scientific- and application-driven field [1–40].

Organo-transition metal compounds, such as the famous Ir(ppy)₃ or [Ru(bpy)₃]²⁺ complexes,¹⁾ represent triplet emitters. This means, they exhibit an emission – a phosphorescence – from the lowest excited electronic triplet state to the electronic singlet ground state. Although this electronic transition is formally forbidden, it may become sufficiently allowed by spin–orbit coupling (SOC) induced by the central metal. Depending on the specific compound, the emission can show widely differing properties. Its wavelength can lie in the spectral range from blue to red, or even from ultraviolet to infrared. Normally, at ambient temperature, the spectra are not resolved line emissions, but rather are broad and often exhibit an undesirably low color purity. The emission decay time ranges from shorter than 1 μs to as long as several milliseconds, and the photoluminescence quantum yield may be almost 100%, or unattractively low. The desire

* Author for correspondence.

1) Chemical structures are shown in Fig. 1.12.

to understand these and many other photophysical properties developed as the focal point of several research groups, and led to the investigation of these luminescent materials in greater detail. Indeed, the main subject of this chapter is to present the background for an understanding of these emission properties. This will be achieved first by discussing some relatively simple – and, with respect to the number of the involved states, sometimes even slightly oversimplified – models, in order to help to introduce also non-specialists to this field. In later sections, a more detailed description of the photophysics of the triplet state is developed. The discussion of these models, and their relationship to the observed properties, will be outlined in rather elementary terms, and illustrated by examples related to OLED emitter materials. In this respect, references relating to further studies will be given.

This chapter is organized in the following manner. Following a very brief introduction into the working principle of an OLED, exciton formation and the process of electron–hole recombination are addressed. There follows a discussion of the process leading to the population of higher excited singlet and triplet states of the doped emitter molecules, and it is shown, how finally the excitation energy is harvested in the emitting triplet state (Section 1.2). Usually, the same state can be populated either directly or indirectly by photoexcitation; therefore, electroluminescence and photoluminescence spectra result from the same electronic state(s) and thus are normally almost equal, at least for doped triplet emitters in the absence of host emission. Consequently, detailed photoluminescence studies can be applied to explore also the electro-luminescence properties of OLEDs. In Section 1.3, the different types of electronic HOMO–LUMO transitions²⁾ are introduced, which are important for organo-transition metal complexes. In particular, ligand-centered (LC), metal-centered (MC), and metal-to-ligand charge transfer (MLCT) transitions are discussed. Models that are based merely on these transitions, however, do not display energy states, such as singlets and triplets. It is possible to show, in a very simple approach, how these states and the related splittings can be deduced from experimentally supported “rules of thumb”. More accurate approaches and models, which include SOC, will also be discussed. The emitting triplet state splits almost in any case into three substates. The extent of this splitting – the zero-field splitting (ZFS) – may serve as a very useful parameter for a classification of the corresponding compound, also with respect to its suitability for OLED application. Especially, it will be shown that the magnitude of ZFS depends on the MLCT character in the emitting state, and is governed by SOC. Interestingly, the SOC routes are distinctly different for quasi-square planar as compared to quasi-octahedral complexes. These differences have direct influences on the properties of the emitting triplet state, and thus also on OLED applications. In Section 1.4, an ordering scheme is presented for triplet emitters based on the amount of ZFS, and trends are discussed, how photophysical properties are

2) HOMO=highest occupied molecular orbital; LUMO=lowest unoccupied molecular orbital.

related to the magnitude of the ZFS. In Sections 1.5 and 1.6 it is shown, in a number of case studies applied to $\text{Pt}(\text{thpy})_2$ and $\text{Ir}(\text{ppy})_3$, how triplet energy level schemes and the emission decay times of the individual triplet substates can be elucidated from highly resolved and broadband emission spectra, respectively. Phosphorescence dynamics and the effects of spin–lattice relaxation (SLR) are addressed in Section 1.7. The influence of high external magnetic fields on the triplet state splitting and the decay dynamics is discussed in Section 1.8, again as a case study focusing on $\text{Ir}(\text{btp})_2(\text{acac})$. In Section 1.9, the importance of vibronic coupling is discussed – that is, the origin of the vibrational satellite structure – which is induced by Franck–Condon (FC) and/or Herzberg–Teller (HT) activity, and which usually determines the form and width of an emission spectrum. Finally, in Sections 1.10 and 1.11, environmental effects on the triplet state energy, splitting and decay dynamics are addressed, and spectral broadening by inhomogeneous as well as by homogeneous effects are discussed. The latter effect leads to the unresolved spectral band structure at ambient temperature. These discussions are again based on case studies applied to $\text{Pt}(\text{thpy})_2$ and $\text{Ir}(\text{btp})_2(\text{acac})$. At higher temperatures, the emission generally represents a thermalized decay from the different triplet substates. In particular in Section 1.11, it is shown that it is possible to simulate the ambient temperature broadband luminescence spectra by use of the well-resolved, low-temperature spectra simply by taking basic spectral broadening mechanisms into account. The chapter is completed with a short conclusion (Section 1.12).

1.2

Electro-Luminescence and the Population of Excited States

In this section, we first present the basic principle of an OLED. Following this short introduction, attention is focused on the energetics and dynamics of electron–hole recombination in the emission layer (EML). Here, the main interest is in those processes which take place within the vicinity of the emitting center. In this context, we explain concepts of exciton formation, spin-statistics, intersystem crossing, and population of the lowest triplet substates, which is often referred to as triplet harvesting.

1.2.1

Multilayer Design of an OLED

Figure 1.1 shows a typical and well-established set-up of an OLED. It consists of a number of thin layers which are either solution-processed or vacuum-deposited, for example, on a glass substrate. In operation, holes are injected from a transparent anode, mostly consisting of a non-stoichiometric composite of SnO_2 (10–20%) and In_2O_3 (90–80%), called “indium tin oxide” (ITO). Adjacent to this anode layer, a hole injection/transport layer (HTL) is normally applied to allow for a well-

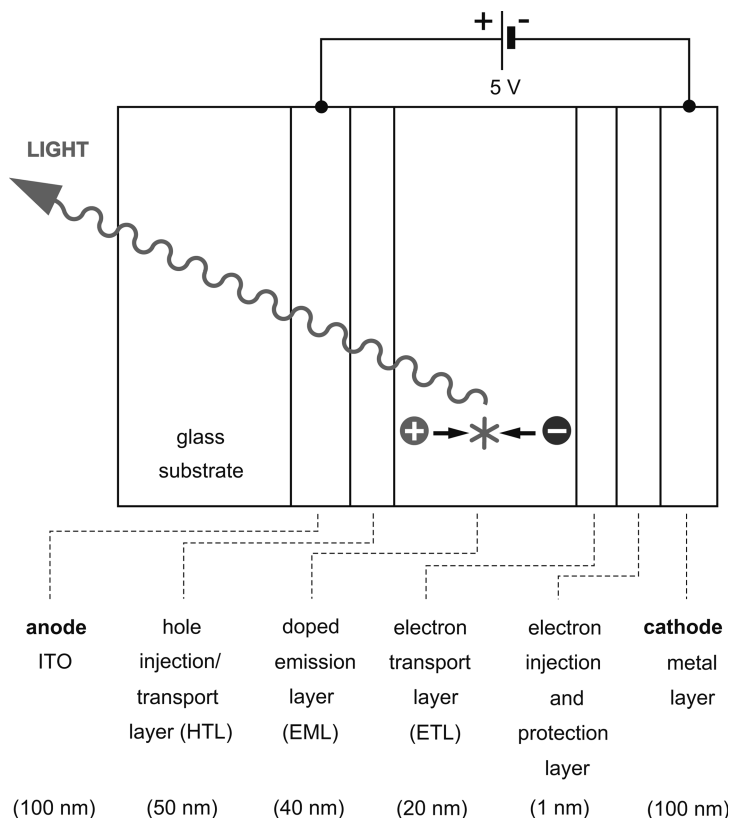


Fig. 1.1 Basic set-up of an organic light-emitting diode (OLED). The different layers are not drawn to scale. Examples of materials used for a realization of an OLED device are given in Fig. 1.2. Within the scope of this chapter, interest is mainly focused on the

process of electron(-)-hole(+) recombination and the triplet state population of the emitter molecule (depicted as a star). Further optimized OLEDs contain additional hole and/or electron blocking layers (e.g., see Ref. [42]).

balanced hole³⁾ transport into the EML. At the opposite side, a metal-cathode with a suitably chosen work function injects electrons into an electron transport layer (ETL). It has been shown that an additional, very thin layer of LiF or CsF (0.5 to

3) Note that the “hole” represents a model particle which is physically based on the movement (hopping) of an electron. The HOMO of a neutral organic molecule is usually populated with two electrons. If one electron is extracted, for example, by transferring it to the anode, a positively charged molecule is left. Subsequently, the empty electron position in the HOMO can be populated by an electron from the HOMO of a neighboring molecule. Thus, the positive charge has moved to the neighbor. An equivalent process occurs

involving the next nearest neighbor, and so on. Thus, the positive charge – called a “hole” – moves from molecule to molecule into direction of the cathode. Such a hole has properties of a particle, it carries a positive charge, a spin (the one of the residual electron) and it can move in the HOMOs with a specific hole mobility. For two molecules with different HOMO energies, the electron hops downwards, and this corresponds formally to an upwards hopping of the hole.

1 nm) strongly reduces the injection barrier and also protects the ETL from chemical reactions with the cathode material [41]. Clearly, although electron transport from the cathode to the EML must be efficient, it is also important that the electron current is well balanced with the hole current in order to avoid ohmic losses. Such losses can be minimized by introducing a hole-blocking layer (e.g., [8, 42]) between the EML and the ETL and/or an electron blocking layer (e.g., [43]) between the HTL and the EML. These additional layers (which are not shown in the diagram) prevent holes/electrons from crossing and leaving the EML without electron–hole recombination. As result, the device efficiency can be distinctly increased. However, such blockings may lead to the build-up of high charge densities at the interfaces, with unfavorable consequences for the device lifetime [44].

The materials used for an OLED device must fulfill a series of requirements, such as suitability for a specific fabrication procedure (e.g., spin-coating, inkjet printing, vacuum deposition), good film-forming properties, sufficiently high glass transition temperature to avoid crystallization of the layer material within the desired lifetime of the device, and chemical and photochemical stability. Moreover, hole and electron injection barriers must be low, and the mobilities as well as HOMO and LUMO energies must match for neighboring layers. A further requirement is that the lowest triplet state of the host material used for the EML lies significantly higher (i.e., about 3000 cm^{-1} or approximately 0.4 eV) than the triplet of the emitting complex. Otherwise, the triplet of the host can be populated, and subsequently the excitation energy can easily diffuse to quenching sites, or can be quenched at the host itself. (Compare also the other contributions to this volume [9, 10]). In particular, for high-energy blue emitters, specific matrix materials must be chosen, or even must still be developed.

Figure 1.2 illustrates one example of a device realized according to the structure depicted in Fig. 1.1. This example (which is adapted from Ref. [45]) is built up by the use of small-molecule, vacuum-depositable materials. The figure depicts the corresponding HOMO and LUMO levels in the absence of an electrical bias, as well as the chemical structures of the materials applied. The diagram shows that energy barriers occur since the hopping of holes upwards (in energy) and of electrons downwards to the EML do not seem to be favored, although this would be advantageous. The energy barriers can be overcome, however, by level shifts due to the external potential, and additionally by thermal activation processes. Level shifts induced by the external potential are not shown in Fig. 1.2. Such a device was first reported by the Forrest and Thompson groups [45] in 2001. It exhibits a relatively high external quantum efficiency of 19% and a luminous power efficiency of 60 lm W^{-1} . These values are obtained only at low current densities. With increasing currents, the efficiency gradually decreases due to a growing influence of different quenching effects [46], of which triplet–triplet annihilation is regarded as being of particular importance [45–47]. In more recent developments, much higher efficiencies have been obtained with modified devices. For example, by p-doping of the HTL and n-doping of the ETL and additionally by introducing a double emission layer (D-EML), the Leo group [48] obtained with the green-emitting $\text{Ir}(\text{ppy})_3$ a luminous power efficiency of 77 lm W^{-1} and an external quantum

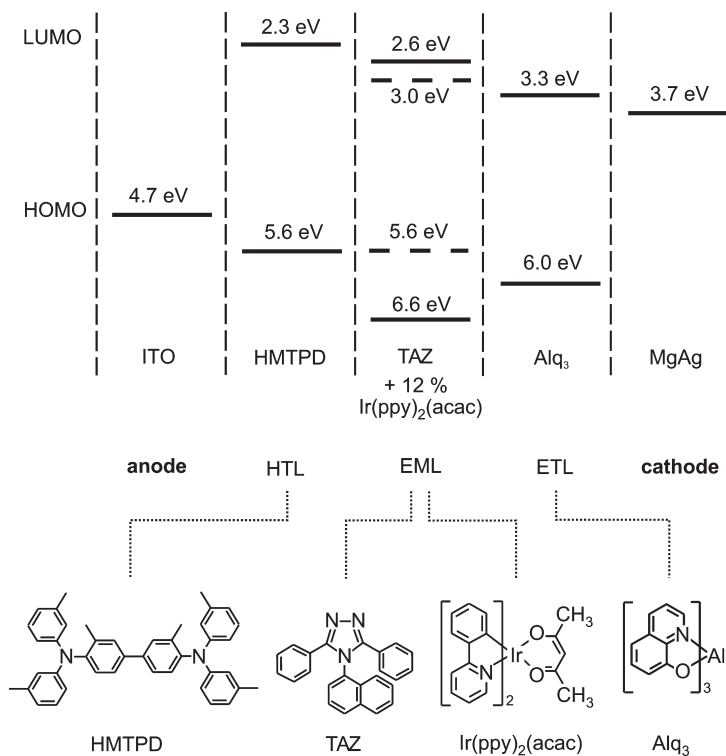


Fig. 1.2 HOMO-LUMO diagram and materials of an OLED device similar to the one shown in Fig. 1.1. The HOMO/LUMO values are given relative to the vacuum level, and therefore are negative. Values and materials are taken from Ref. [45]. For the emission layer (EML), the oxidation and reduction potentials are given for the host (TAZ, solid line) and the emitter (Ir(ppy)₂(acac), dashed line).

efficiency of more than 19% at 100 cd m^{-2} at an operating voltage of only 2.65 V. Also applying the Ir(ppy)₃ complex, the authors of Ref. [49] obtained a luminous power efficiency of 79 lm W^{-1} and a current efficiency of 81 cd A^{-1} by use of a transparent silver anode. This device structure features an enhanced hole injection, and also allows for more efficient outcoupling of light due to a microcavity structure. In Ref. [50], values of 110 lm W^{-1} at 10^3 cd m^{-2} were communicated. By use of a microcavity, two-unit tandem device, efficiencies as high as 200 cd A^{-1} at 10^3 cd m^{-2} were reported recently [51]. Interestingly, efficiencies which can be reached today with OLEDs are as high as – or even higher than – those of highly efficient inorganic LEDs.

Although, in this chapter, we do not aim to discuss further progress in the field of OLED device architectures, it is referred to some interesting recent developments reported in the literature [51–60].

1.2.2

Electron–Hole Recombination, Relaxation Paths, and Light Emission

In order to gain some general understanding of the processes in the EML, Fig. 1.3 displays a simplified model of electron–hole recombination. This layer consists of a host material (matrix) which is doped with a suitable triplet emitter complex at low concentration. For the subsequent discussion, it is assumed that both charge carriers – electron and hole – are already present in the EML. Different steps of electron–hole recombination – that is, exciton formation and population of the emitting triplet state – can take place. For example, the exciton can be formed and trapped on the host molecule with subsequent energy transfer to the triplet emitter. In an alternative process, one of the charge carriers is directly trapped on the emitter dopant itself and the recombination occurs on this molecule. This has been proposed specifically for efficient devices containing Ir(III) emitter complexes [45, 61, 62], but also for PtOEP [63], that the hole is trapped first on the emitter complex. The electron – or, more exactly, the negatively charged polaron⁴ [64] – experiences a Coulomb attraction and the formation of the overall neutral exciton starts. This process of hole trapping as a first step can occur, if the oxidation potential of the emitter complex fits well to the HOMO energy of the hole transport material (HTL) (compare Ref. [45]). Presumably, this process of charge carrier trapping directly on the emitter molecule will usually result in a more efficient OLED device than by indirect excitation of the emitter molecule by energy transfer [5]. In part, alternative approaches for the description of exciton formation processes are discussed in Refs. [5, 65, 66].

For the model depicted in Fig. 1.3, it is assumed (as mentioned above) that the hole is already trapped at the emitter molecule. In our simple approach, it is supposed that the reorganization energy after oxidation of the emitter (hole trapping) sitting in the relatively rigid host environment is small. Subsequently, we discuss the electron dynamics until the emitting triplet state is populated. With an external potential ΔV , the electron will migrate through the host material towards the anode. Under normal conditions, this process additionally requires thermal activation energy to overcome energy sinks due to inhomogeneities and due to host reorganization effects related to the polaronic properties of the electron. Electron trapping is avoided if the energies of the sink depths are less than, or on the order of, the thermal energy $k_B T$, where k_B is the Boltzmann constant and T the absolute temperature.

When the electron is still far from the trapped hole, it will migrate towards the anode independently from the hole. Thus, the hole and electron are neither bound nor correlated (see left-hand side of the diagram, Fig. 1.3). However, when the electron migrates further into a region given by a critical electron–hole separation R_C , the positively charged hole (h) will attract the electron (e). This distance is

4) Electron (or hole) hopping is normally connected with a polarization of the matrix. Therefore, the corresponding negatively (positively) charged particle coupled to

matrix distortions represents a polaron. For background information see, for example Ref. [64].

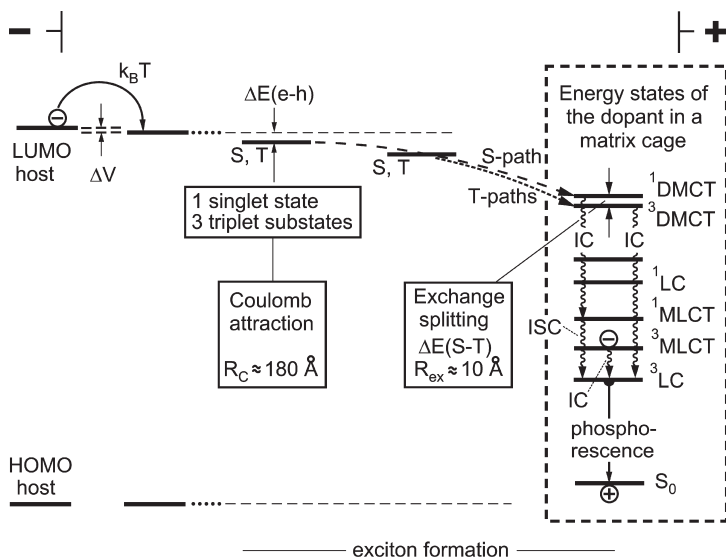


Fig. 1.3 Dynamics of exciton formation. In this model, the exciton formation is induced by Coulomb attraction between electron and hole and starts already at a separation of 150 to 180 Å. The exciton trapping on the emitter complex, which is doped into a host material, occurs via charge transfer states [5, 69]. The wavefunctions of these $^{1,3}\text{DMCT}$ states extend over 10 to 15 Å, and thus involve the triplet emitter itself and the nearest-neighbor host

molecules. The exciton trapping processes lead finally to the population of the lowest excited triplet state(s) of the emitter molecule via internal conversion (IC) and intersystem crossing (ISC). The lower-lying states depicted in the dashed frame represent electronic states of the doped emitter molecule itself. Note, this energy level diagram is strongly simplified.

reached when the energy of Coulomb attraction $\Delta E(e-h)$ is of similar size as the thermal energy $k_B T$. Thus, for an estimate of R_C , we can write

$$\Delta E(e-h) = \frac{e^2}{4\pi\epsilon_0\epsilon R_C} = k_B T \quad (1)$$

wherein e is the electron charge and ϵ_0 and ϵ represent the dielectric constants of the vacuum and the host material, respectively. If a dielectric constant of $\epsilon = 3$ is assumed, a value of $R_C \approx 180 \text{ \AA}$ is obtained for $T = 300 \text{ K}$. This means that the electron experiences the hole potential even when it is still far from the trapped hole. Both particles are already bound, although a relatively large number of host molecules lies between electron and hole. These two attracting particles may already be called “exciton”. However, at this electron–hole separation, the exciton can easily dissociate thermally.

For the further discussion, it is required to take also the spins of both electron and hole into account. The spin of the hole is given by the spin of the residual electron at the emitter molecule. In a quantum mechanical treatment, in which

the bound electron–hole states must be described by four antisymmetrized wavefunctions, the spins are coupled and *four* new combined states are obtained – that is, *one* singlet state and *one* triplet state. The triplet consists of *three* substates. These substates differ from each other mainly by their relative spin orientations. An energy splitting between the resulting singlet and triplet states may be neglected at large electron–hole separations. Therefore, the corresponding exciton state – being four times quasi-degenerate – is shown in Fig. 1.3 (middle) just by one energy level, designated as **S**, **T**. In a statistical limit, all *four* substates of this exciton state will be formed (populated) with equal probability. Consequently, a *population ratio of one to three* of singlet to triplet substates is obtained. For a more detailed discussion concerning the statistically determined population ratio, see Refs. [67, 68].

Driven by the long-range electron–hole Coulomb attraction, the electron moves further on matrix molecules towards the trapped hole. When the electron reaches a distance of 10 to 15 Å – that is, when the electron is approximately located in the first coordination sphere of the emitter dopant – the wavefunctions of electron and hole (or that of the residual electron) begin to overlap slightly [5, 69]. Consequently, the exchange interaction must be taken into account. This quantum mechanical interaction, based on the electron–electron interaction, is responsible for a splitting $\Delta E(S-T)$ of the singlet state **S** and the triplet state **T** by about twice the exchange integral. In this situation of small wavefunction overlap, $\Delta E(S-T)$ depends approximately exponentially on the electron–hole separation R

$$\Delta E(S-T) \sim \exp(-aR) \quad (2)$$

where a is a constant which depends on the individual wavefunctions of the emitter dopant and the nearest neighbor host molecules. Due to the still relatively large electron–hole separation of 10 to 15 Å with respect to the extension of the wavefunctions, the singlet–triplet splitting is expected to be very small, i.e. much smaller than is typically found for singlet–triplet splittings in molecules.

In the subsequent discussion, we follow further the model first presented by Yersin [5, 69]. According to this approach, it is suitable to analyze the above-described situation also from a slightly different viewpoint. Let us focus only on the emitter complex, the dopant (D), and its first coordination sphere of matrix (M) molecules. In this relatively large dopant–matrix–cage unit, the hole is located in the HOMO of the dopant and the electron resides on the LUMO of a matrix molecule. This situation corresponds to a charge transfer excitation. The corresponding states represent dopant-to-matrix charge transfer (DMCT) states. When the spin of the remaining electron in the HOMO of the dopant (D) and the spin of the electron in the LUMO of the matrix (M) molecule as well as the electron–electron interaction are taken into account, $^1\text{DMCT}$ and $^3\text{DMCT}$ states are obtained.⁵⁾ The corresponding splitting is relatively small due to the weak overlap

5) In Section 1.3, we will discuss in more detail, how singlet and triplet states are deduced from HOMO–LUMO excitations.

of the involved molecular orbitals. Clearly, these two states correspond to those exciton states **S** and **T** which are realized at a small electron–hole separation (Fig. 1.3).

The discussion presented above allows us to relate the exciton states with states of a larger molecular unit which consists of the dopant and its matrix cage. This molecular unit exhibits the $^1\text{DMCT}$ and $^3\text{DMCT}$ states as well as a number of lower-lying states which are largely confined to the dopant (triplet emitter) itself, such as $^{1,3}\pi\pi^*$, $^{1,3}\text{dd}^*$, $^{1,3}\text{MLCT}$ states or adequate mixtures of these (see also Section 1.3).⁶⁾ The resulting energy level diagram is depicted in the dashed frame of Fig. 1.3.

Interestingly, on the basis of this energy level scheme, one obtains also information about the relaxation paths from the exciton charge transfer states $^1\text{DMCT}$ and $^3\text{DMCT}$ to the lower-lying states which largely belong to the emitting center. In particular, the relaxation from the $^1\text{DMCT}$ state to lower states will be faster within the system of singlet states than making a spin-flip first. This is due to the fact that SOC in organic host molecules (matrix) is relatively small and, thus, intersystem crossing (ISC) is not favored. As consequence, a fast singlet path (internal conversion) is obtained that finally populates the lowest singlet state (Fig. 1.3). Subsequently, the population of this lowest singlet will be followed by ISC processes to the lowest triplet substates. In case of significant singlet–triplet mixing due to SOC, the difference between ISC and internal conversion (IC) might be lost. An initial population of the $^3\text{DMCT}$ state is similarly followed by a very fast relaxation (IC) within the system of triplet states down to the lowest triplet state (Fig. 1.3). The beginning of these relaxation processes corresponds to the singlet and triplet paths in the exciton trapping model, as shown in Fig. 1.3 (compare Refs. [5, 69].) The relaxation times within the singlet and triplet system, respectively, are of the order of 1 ps or faster, while the ISC processes can be slower or of similar time, depending on the importance of SOC and the resulting perturbation of the lowest triplet by singlet admixtures. In a favorable situation, which is usually realized for the organo-transition metal triplet emitters, the ISC rate is very high (order of 10^{12} to 10^{13} s^{-1}) [70, 71]. Thus, relaxation processes to the lowest triplet state occur mostly with a yield of 100%. This means that all originally formed singlet excitons (25%) and triplet excitons (75%) finally relax into the lowest triplet state of the doped emitter molecule. This process is called *triplet harvesting*. Therefore, under suitable conditions a fourfold larger electro-luminescence efficiency for triplet emitters can be obtained compared to purely organic singlet emitters.⁷⁾

6) Within this simple model, it is assumed that the energy states of the matrix (host) molecules lie at relatively high energies and thus do not interfere significantly with the lower-lying states of the dopant (triplet emitter).

7) For purely organic molecules, the radiative triplet–singlet transition rates are, at ambient temperature, orders of magnitude smaller than the corresponding non-radiative rates. Therefore, any excitation energy is converted into heat and the triplets do not emit.

1.3 Electronic Excitations and Excited States

In general, photoluminescence properties are largely determined by the nature of those molecular orbitals (MOs), which are mainly responsible for the electronic ground state and the lowest excited state. These are called “frontier orbitals”. Here, the aim is to focus on organo-transition metal complexes, such as Ir(ppy)₃, Ir(ppy)₂(CO)(Cl), Ir(btp)₂(acac), Pt(thpy)₂, [Pt(bpy)₂]²⁺, Re(phen)(CO)₃(Cl), [Ru(bpy)₃]²⁺, [Os(bpy)₃]²⁺, etc. For such compounds, different excitations between various MOs have to be taken into account.⁸⁾ Specifically, there are

- ligand-centered (LC) excitations, e.g., of π - π^* character
- metal-centered (MC) excitations, e.g., of d-d* character
- metal-to-ligand charge transfer (MLCT) excitations, e.g., of d- π^* character.

In these descriptions, the asterisk refers to an excited (i.e., a non-occupied) MO.

However, it is not sufficient to restrict the discussion only to HOMO \leftrightarrow LUMO transitions. Energetically nearby lying orbitals can also dominate emission properties. Thus, HOMO-1, HOMO-2, LUMO+1, LUMO+2, etc. have also to be included in the set of frontier orbitals. In this section, we discuss properties of the above-mentioned excitations and trends concerning the resulting electronic states, such as singlet and triplet states. These are many-electron states and can be significantly mixed by SOC. This presentation will initially be carried out using rather simple models, although more detailed descriptions are also presented later on to illustrate the nature of the set of low-lying states and the importance of SOC.

1.3.1 Ligand-Centered (LC) Transitions: States and Splittings

In a series of compounds, the lowest excited states are determined dominantly by MOs which can be well described by the π -HOMO and the π^* -LUMO of the organic ligands, since MOs of other than π and π^* character lie at significantly lower and higher energies, respectively. Thus, it is suitable to confine a first-order approach only to the HOMO-LUMO excitation(s) of the ligand(s). Clearly, these orbitals and their energies are somewhat altered by coordination of the ligand(s) to the positively charged metal. Usually, this leads to a red shift (i.e., a shift to lower energy) of the corresponding transitions of the order of 10^3 cm^{-1} ($\approx 0.12 \text{ eV}$).⁹⁾ Of course, the metal induces further changes, and in particular changes which

8) For completeness, also ligand-to-metal-charge-transfer (LMCT) excitations, e.g., of π -d* character, are mentioned. However, for the compounds of interest in this chapter

the corresponding excited states exhibit relatively high energies and therefore, are not discussed at this point.

9) $1 \text{ eV} \triangleq 8068 \text{ cm}^{-1}$.

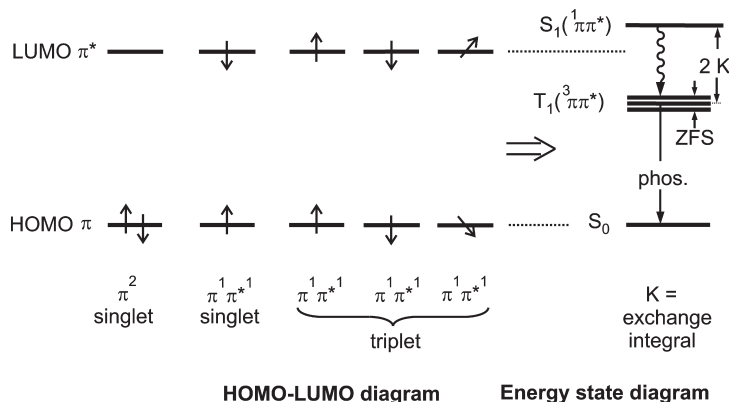


Fig. 1.4 Comparison of a HOMO-LUMO diagram to an energy state description. The configuration π^2 leads to the ground state S_0 , while the configuration $\pi^1\pi^{*1}$ gives four different excited states, one singlet S_1 and one triplet T_1 which consists of three substates. By taking the change of electron–electron interaction for both configurations into account, usually a significant $\Delta E(S_1 - T_1)$

splitting is obtained. For ligands which are in the focus of this contribution, $\Delta E(S_1 - T_1)$ can be as large as 10^4 cm^{-1} . The three triplet substates of T_1 exhibit a splitting, the zero-field splitting (ZFS). The corresponding value can be used to assess a triplet emitter compound for its application in an OLED. (See Section 1.4 and Fig. 1.11.)

result from SOC, such as changes of radiative and non-radiative rates as well as of energy splittings. (These important effects will be discussed later in Sections 1.3.3.3 and 1.4.2.) For completeness, it should be mentioned that, for this class of compounds, the lowest excited state (the triplet state) is largely localized on one ligand (compare Refs. [72–74] and Section 1.4.2).

For most molecules, which are of interest here, the HOMO is occupied by two electrons and the compound is diamagnetic. Thus, the two electrons carry opposite spins (α and β spins). This situation is described by an electron configuration of π^2 . The resulting state, the ground state, is a spin singlet S_0 ($^1\pi^2$) (Fig. 1.4, left). When, after a HOMO–LUMO excitation the spins are also taken into account, one obtains for the excited state configuration $\pi^1\pi^{*1}$ four different situations (Fig. 1.4, middle). An excitation without a spin flip gives an excited singlet, while an excitation with a spin flip gives a triplet due to three different possible spin orientations. This description is similar to the one discussed in Section 1.2.2. Again, in a quantum mechanical treatment, four different (antisymmetrized) wavefunctions must be formulated to describe the resulting singlet and the three triplet states (compare, for example, Ref. [75], p. 163).

In the simple HOMO–LUMO model, all four states, which result from the $\pi^1\pi^{*1}$ configuration, still have the same energy and are degenerate. However, from spectroscopic investigations it is known that the splitting between the excited singlet state and the excited triplet state is usually significant. For example, for the ligands discussed in this chapter, it can be as large as 10^4 cm^{-1} ($\approx 1.24 \text{ eV}$). There-

fore, the HOMO–LUMO model must be improved, specifically, by taking changes of the electron–electron interaction into account which are connected with the HOMO–LUMO excitation. This results in the energy state diagram (or the many electron state diagram) as depicted in Fig. 1.4 (right-hand side). A quantum mechanical consideration shows that the triplet state T_1 (or ${}^3\pi\pi^*$), consisting of three substates, is stabilized by an energy given by a difference of Coulomb integrals, while the singlet state S_1 (or ${}^1\pi\pi^*$) is destabilized relative to the triplet state by twice the exchange integral

$$K = \text{const} \times \left\langle \pi(r_1)\pi^*(r_2) \left| \frac{1}{r_{12}} \right| \pi(r_2)\pi^*(r_1) \right\rangle \quad (3)$$

wherein π and π^* are the HOMO and LUMO wavefunctions, r_1 and r_2 represent the electron coordinates, and r_{12} the separation between the two electrons (compare, for example, Ref. [75], p. 174). The exchange interaction is a quantum mechanical effect which takes the spin correlation into account. This means that two electrons with opposite spin orientations (in the singlet state) have a larger probability of being found near to each other than two electrons with the same spin orientation (the triplet state). In the latter situation, the two electrons have the tendency to avoid each other. Hence, the average electron–electron repulsion is smaller and thus the triplet has a lower energy than the singlet state (Fig. 1.4).

The exchange integral – as displayed in Eq. (3) in a shortened notation (compare, for example Ref. [76]) – is given in this elementary chapter, since it permits important qualitative conclusions to be reached by considering the overlap of the involved wavefunctions. The following conclusions fit to the spin correlation model discussed above. First, with an increasing conjugation length of the π and π^* orbitals, the exchange integral K becomes smaller. For example, in purely organic molecules, the singlet-triplet splitting $\Delta E({}^1\pi\pi^* - {}^3\pi\pi^*)$ decreases in the series of benzene, naphthalene, anthracene from $\approx 18\,000\text{ cm}^{-1}$ ($\approx 2.2\text{ eV}$) [77], to $12\,300\text{ cm}^{-1}$ ($\approx 1.5\text{ eV}$) [78], and to $10\,500\text{ cm}^{-1}$ ($\approx 1.3\text{ eV}$) [78]. Second, when the MOs are mainly confined to different spatial regions of the molecule, the MO overlap can become very small, and consequently so also can the integrals. For example, for n -HOMO to π^* -LUMO excitations, which are relevant for organic molecules with heteroatoms, such as benzophenone, the singlet-triplet splitting $\Delta E({}^1n\pi^* - {}^3n\pi^*)$ amounts to only 1750 cm^{-1} ($\approx 0.22\text{ eV}$) [79]. Equivalent considerations apply also to states of organo-transition metal complexes. Small admixtures of metal d-orbital or MLCT character to the ligand-centered states will increase the spatial extension of the wavefunctions and thus reduce the exchange integral – that is, the singlet–triplet splitting between the perturbed ${}^1\text{LC}({}^1\pi\pi^*)$ and ${}^3\text{LC}({}^3\pi\pi^*)$ states. For example, $\Delta E({}^1\pi\pi^* - {}^3\pi\pi^*)$ of the free ligand H(2-thpy) is of the order of 10^4 cm^{-1} (1.24 eV), as can be estimated from the data given in Ref. [80], whereas for $\text{Pd}(\text{thpy})_2$ (doped into n -octane) $\Delta E({}^1\text{LC} - {}^3\text{LC})$ is significantly smaller and amounts only to 5418 cm^{-1} [70]. This tendency becomes even more obvious for ${}^1\text{MLCT} - {}^3\text{MLCT}$ splittings.

The triplet state is always split into three substates, at least, if the symmetry of the molecule is sufficiently low.¹⁰⁾ This is valid for most organo-transition metal compounds that are of interest for OLED applications. The splitting occurs also at zero magnetic field, and is therefore referred to as zero-field splitting (ZFS) (Fig. 1.4). For ${}^3\pi\pi^*$ states of organic molecules, the ZFS is mainly induced by spin–spin interactions of the two unpaired electrons in the triplet state (compare, for example, Refs. [77, 81, 82]). This interaction leads to ZFS-values of the order of 0.1 cm^{-1} ($\approx 1.2 \times 10^{-5}\text{ eV}$). For largely ligand-centered ${}^3\text{LC}$ states of organo-transition metal complexes, the value of ZFS lies in the same order of magnitude. For example, for $[\text{Rh}(\text{bpy})_3]^{3+}$, the total ZFS has been determined as 0.125 cm^{-1} ($\approx 1.55 \times 10^{-5}\text{ eV}$) [83, 84], and for $\text{Pd}(\text{qol})_2$ to about 0.25 cm^{-1} ($\approx 3.1 \times 10^{-5}\text{ eV}$) [85]. However, SOC carried by metal d-orbitals can drastically increase the magnitude of ZFS, as found for ${}^3\text{MLCT}$ states. (Compare especially Sections 1.3.3, 1.4, and Refs. [5, 70, 72–74].) In this situation, the small contribution from spin–spin interactions can be neglected.

For completeness it is mentioned that, although the ZFS values of only slightly perturbed ${}^3\text{LC}({}^3\pi\pi^*)$ states of organo-transition metal compounds are of similar size, as found for purely organic molecules, the metal can manifest itself already drastically by increasing radiative and/or non-radiative rates. This is a consequence of a relatively small but still very effective SOC. For instance, the population of the triplet from an excited singlet state by ISC becomes orders of magnitude faster. Thus, the quantum efficiency of ISC reaches 100%. For example, for $\text{Pd}(\text{thpy})_2$ [70] and $\text{Pt}(\text{qol})_2$ [86], which both emit from ${}^3\text{LC}$ states, we determined ISC relaxation times of $\tau(\text{ISC})=800\text{ fs}$ and 500 fs , respectively. Moreover, the radiative $\text{T}_1 \rightarrow \text{S}_0$ rate also becomes orders of magnitude larger than are found for purely organic molecules. Thus, mostly the triplet substates can easily be excited resonantly [87, 88].¹¹⁾ This implies that the increased radiative rate can dominate over the non-radiative deactivation. As a consequence, even high-emission quantum yields can occur. For example, for $\text{Re}(\text{phbt})(\text{CO})_4$ – a ${}^3\text{LC}({}^3\pi\pi^*)$ emitter with a ZFS much smaller than 1 cm^{-1} – the photoluminescence quantum yield ϕ_{PL} amounts to 27% at ambient temperature in ethanol (Ar saturated) [88]. However, the emission decay time of $\tau(300\text{ K})=21\text{ }\mu\text{s}$ is still relatively long, and therefore the compound is probably not well suited for OLED applications [88] but probably well suited as an oxygen sensor molecule. It will be shown below that the size of ZFS represents a good measure of the importance of MLCT character in the lowest triplet state and that, for the most efficient OLEDs, emitter compounds are used which exhibit

10) Molecules which belong to a point group symmetry lower than C_3 do not exhibit any state degeneracies (apart from Kramer's degeneracies of molecules with uneven numbers of electrons).

11) For several compounds only two of the three triplet substates of dominant ${}^3\text{LC}$ character

can be excited directly from the ground state, while the transition to the third substate is still largely forbidden. This has, for example, been shown for $\text{Pd}(\text{thpy})_2$ [70], $\text{Pt}(\text{qol})_2$ [71], $\text{Ir}(\text{ppy})_2(\text{CO})(\text{Cl})$ [87], and $\text{Re}(\text{phbt})(\text{CO})_4$ [88].

ZFS-values of about 10 cm^{-1} or larger ($1.2 \times 10^{-3}\text{ eV}$). (Compare Sections 1.3.3, 1.4, and Refs. [5, 70, 72–74].)

1.3.2

Metal-Centered Transitions and States

A large number of compounds is known, for which the absorption and luminescence properties are determined by metal-centered (MC) excitations. For example, complexes or doped materials of main-group metal ions with s^2 ground state and sp excited state configurations have low-lying MC excitations (e.g., $[\text{PbCl}_4]^{2-}$) [89–91]. Lanthanide compounds with f - f excitations also exhibit MC transitions (e.g., Eu^{3+} , Tb^{3+} compounds; see e.g., Refs. [92–96]). A short summary of compounds which exhibit different types of MC transitions is found in Ref. [91]. However, within the scope of the present chapter, we are interested in properties of d - d^* excitations and related states. Well-known compounds with optical properties dominated by such MC excitations include ruby (Cr^{3+} in Al_2O_3) [97, 98] and $[\text{Cr}(\text{urea})_6]^{3+}$ [99–101], both with $3d^3$ configurations. The latter compound is among the first synthesized transition metal complexes with organic ligands. Further examples include $[\text{MnCl}_4]^{2-}$ [102], $[\text{Co}(\text{CN})_6]^{3-}$ [103, 104], and $[\text{PtCl}_4]^{2-}$ [104, 105], in which the metal centers have $3d^5$, $3d^6$, and $5d^8$ configurations, respectively.

The d -orbitals and d - d^* transitions are indirectly of importance for OLED materials. This is due to two different effects. On the one hand, the quantum mechanical mixing of d -orbitals of open-shell transition metal ions, such as Pt^{2+} , Ir^{3+} , or Os^{2+} , can induce the required SOC to make the formally forbidden triplet–singlet transitions sufficiently allowed (see next section). On the other hand, states which result from d - d^* excitations often quench the emission efficiently, and therefore should not lie in a thermally accessible energy range of the emitting states (see below).

Usually, a description of dd^* states is carried out by use of group theory and the symmetry of the complex. An introduction to ligand field or crystal field theory is found in most inorganic chemistry textbooks (e.g., see Refs. [106, 107]), whilst more detailed descriptions are found in Refs. [108, 109]. At this point, we present only a brief illustration of excitations (in particular of HOMO–LUMO excitations), provide some comments regarding the resulting states, and highlight the relevance of these states for triplet emitters in OLEDs. In this section, only those compounds having central metal ions with a d^6 configuration, such as Ir^{3+} , Ru^{2+} , Os^{2+} , Re^+ , and W^0 , will be discussed as examples. These metals/ions tend to prefer a sixfold coordination which includes, for example, three bidentate chelates. In a first-order approach, the complexes can be described in an octahedral symmetry (symbol: O_h) of the first coordination-sphere around the central metal. In this symmetry, the d -orbitals split into two sets of orbitals (Fig. 1.5). The magnitude of splitting is given by the ligand field strength, and amounts to Δ which is – for historic reasons – often named 10 Dq . The Dq parameter varies with the ligand according to the spectrochemical series (compare, for example Refs. [107], p. 221, and [108], p. 84):

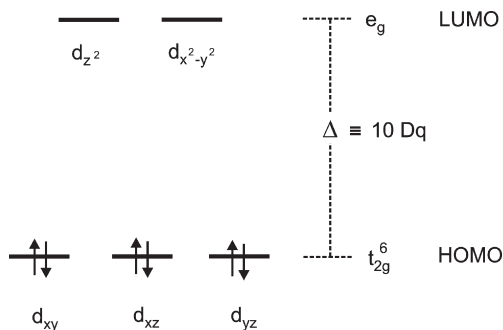
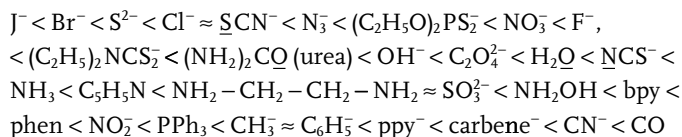


Fig. 1.5 Splitting of d-orbitals in an octahedral ligand field with O_h symmetry. For a high ligand field (large Δ or Dq value), the ground state configuration is t_{2g}^6 .

This series gives the approximate ordering of the Dq parameter.¹²⁾ In particular, ligands found on the left-hand side induce a small ligand field splitting (they are called “weak” ligands), while those on the right-hand side of the series are “strong” ligands with large ligand field splittings. These splittings depend also on the central metal ion. For OLED applications, one is usually interested in compounds with large ligand field splittings to avoid emission quenching processes at ambient temperature (see below). Consequently, it is useful to have some rules of thumb for the development of efficient triplet emitters. Such rules should help to estimate changes of Dq values with chemical variations. Indeed, if a reference compound is available, then specific trends can be given (Ref. [108], p. 83):

1. Compounds with the same ligands and the same central metal ion exhibit a 40–80% Dq increase, when the metal oxidation changes from 2+ to 3+.
2. Compounds with the same ligands experience an increase of Dq by 30–40%, when the metal of the first row of transition metal ions in the Periodic Table is replaced by one of the second row, and similarly if a second-row metal ion is replaced by one of the third row.
3. For compounds with mixed ligands (heteroleptic compounds), the Dq value can be estimated from the average ligand field strength.

12) According to different binding properties in different complexes, the sequence of the ligands in the spectrochemical series may slightly vary. In particular, the positions of $(\text{ppy})^-$ and carbenes^- are given only tentatively.

From Fig. 1.5 it is clear that compounds with a d^6 electron configuration and a large ligand field splitting have a t_{2g}^6 ground state configuration (in an O_h parent group approach). Thus, the t_{2g} sub-shell is filled. This leads to a low-spin compound with a (totally symmetric) diamagnetic ground state ($^1A_{1g}$ in O_h). From the excitations $t_{2g}^6 \rightarrow t_{2g}^5 e_g^1$ and $t_{2g}^6 \rightarrow t_{2g}^4 e_g^2$ etc., the excited states can be determined by taking electron–electron interaction into account (e.g., see Refs. [108, 109]). Usually, this is carried out by use of group theoretical methods. For example, for the $t_{2g}^5 e_g^1$ configuration, two triplets and two singlets are obtained. In a group theoretical notation (in the O_h group), the terms ordered according to increasing energy are $^3T_{1g}$, $^3T_{2g}$, $^1T_{1g}$, and $^1T_{2g}$. Further excitations such as $t_{2g}^6 \rightarrow t_{2g}^3 e_g^3$ lead to a number of additional energy states. All of the resulting states are summarized in the well-known Tanabe–Sugano diagrams, which are found in many inorganic textbooks (e.g., see Ref. [106], p. 1189, and Ref. [107], p. 683).

It is an important property that all of these excited states have distinctly larger metal–ligand bond lengths than the ground state. This can simply be deduced by visualizing the effects of the HOMO–LUMO excitation of $t_{2g}^6 \rightarrow t_{2g}^5 e_g^1$. It corresponds to a population of an anti-bonding e_g orbital from a non-bonding t_{2g} orbital. Therefore, the metal–ligand bond lengths increase, and additionally the potential surfaces become less stiff (smaller force constants). Consequently, the potential surfaces of the ground and of the excited states can cross at relatively low energies. These changes can have significant effects on non-radiative deactivation processes. This is due to a resulting distinct overlap of lower-lying vibrational wavefunctions of the excited electronic state with high-energy vibrational wavefunctions of the electronic ground state. Accordingly, the corresponding Franck–Condon factors which govern the rate of the radiationless deactivation from the excited state to the ground state, increase (compare , for example, Refs. [78], p. 71 and [110], p. 129). As consequence, the radiationless deactivation rate can become significantly larger than the radiative rates, and an emission is prevented (“quenched”).

In summary, a population of the excited $^1,3dd^*$ states of transition metal compounds with a d^6 configuration often leads to emission quenching at ambient temperature. Although, for OLED applications, the $^1,3dd^*$ states do not have to be characterized in detail, it is still required to take care of these quenching states. Energetically, they should not lie too close to the emitting states of, for example, $^3LC/^3MLCT$ character (compare next section). An energy difference of 3000 to 4000 cm^{-1} (0.37 to 0.50 eV) is required to obtain a sufficiently small Boltzmann factor, and thus a sufficiently small population of the quenching state, at ambient temperature. Note that arguments similar to those developed for central metal ions with a d^6 configuration also hold for compounds with a d^8 configuration, such as Pt(II) or Ir(I) complexes.

However, a strategy which aims to maximize the ligand field strength in order to shift the $^1,3dd^*$ states to an energy as high as possible will fail. For a very high Dq value, the occupied d-orbitals may be stabilized too much. This can have the consequence that a necessary MLCT admixture to the emitting triplet becomes too small and that the resulting compound turns into a less effective 3LC emitter. Exactly this behavior is observed for Re(I) complexes. Re(phen)(CO)₃(Cl) shows a

relatively good OLED performance [111, 112] which is related to a large ZFS of 50 cm^{-1} and thus to a large MLCT perturbation of the emitting triplet. For $\text{Re}(\text{phbt})(\text{CO})_4$, on the other hand, with ligands of an on-average much higher Dq value, the emitting state turns out to be a ^3LC state (ZFS $\ll 1\text{ cm}^{-1}$) [88]. For this latter material, only a very weak OLED performance was observed [88]. Obviously, a good balance between MLCT character of the emitting state and a high energy separation of the quenching state must be found.

1.3.3

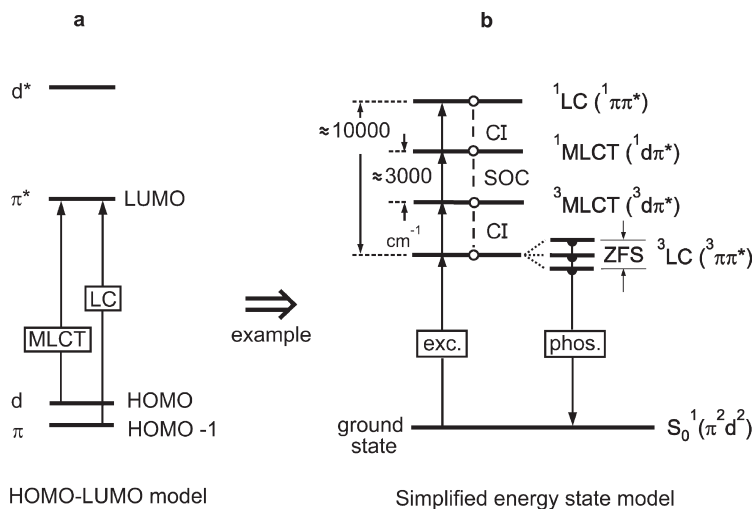
Metal-to-Ligand Charge Transfer/Ligand-Centered Transitions: States in Organo-Transition Metal Triplet Emitters

In the two previous sections, we have discussed well-seizable models with respect to the frontier orbitals and the resulting energy states. The situation becomes a little more complicated, when additionally MLCT transitions are taken into account. In particular, the interplay – that is, the quantum mechanical mixing between ^3LC , ^1LC , $^3\text{MLCT}$, and $^1\text{MLCT}$ states – determines the properties of the lowest triplet state and thus also the applicability of an emitter material in an OLED. For example, a compound with an almost “pure” ^3LC emitting state would presumably not be well suited as an OLED emitter, whereas a complex with a mixed emitting $^3\text{LC}/^3\text{MLCT}$ state might be a very good candidate. Such mixtures can occur, for instance, for a d-orbital admixture to the HOMO of mainly π character, that is, for $\pi\text{d} \rightarrow \pi^*$ transitions. (Compare the examples given at the end of Section 1.3.2 with those later in this section.) The inherent reason is SOC which, for the compounds under consideration in this contribution, is carried by the metal 5d-orbitals.

It is the subject of this section, to illustrate how many-electron states result from frontier orbitals, such as HOMO-1, HOMO, LUMO, LUMO+1, etc., and to discuss the properties of electronic states, the MLCT character, SOC routes, triplet state splittings, and radiative rates. In a first step (see Section 1.3.3.1), a very simple model is presented with a strongly restricted number of MOs. Yet, this model is well suited for describing some trends. In a second step (see Section 1.3.3.2), it will be shown that a more realistic model requires the inclusion of a larger number of active frontier orbitals, and a very large number of states in the optical energy range is obtained. Finally, in Section 1.3.3.3, the important effects induced by SOC are discussed.

1.3.3.1 Introductory MO Model and Energy States

Figure 1.6 illustrates a strongly simplified MO diagram for an organo-transition metal compound, and how the MOs relate to the energy states. In this model, one single ligand π -orbital (HOMO-1) and one d-orbital (HOMO) are considered as the occupied frontier orbitals. Both of these are occupied with two electrons. The lowest unoccupied orbital is given by a single π^* -MO. An additional unoccupied d*-orbital, also displayed in the figure, is not further discussed, as it is assumed that its energy and those of the resulting states are sufficiently high and thus have no importance for this introduction (but compare Section 1.3.2). In summary, this



HOMO-LUMO model

Simplified energy state model

Fig. 1.6 (a) Introductory MO model for a compound with single π , d , and π^* orbitals and the respective MLCT and LC transitions. It is assumed that the d^* -orbital lies at a significantly higher energy and that it does not lead to low-lying energy states. (b) From the two MLCT and LC transitions eight energy states are obtained: two singlets 1LC and 1MLCT , three 3LC , and three 3MLCT substates. The states can experience substantial quantum mechanical mixings due to configuration interaction (CI) and spin-orbit

coupling (SOC). SOC induces the zero-field splitting (ZFS). After these quantum mechanical mixings, the terms singlet, triplet, LC, MLCT can no longer be regarded as “pure” classifications. For details, see Section 1.3.3.3. Here, we illustrate a situation in which the order of the d - and π -orbital does not necessarily lead to the same sequence of the corresponding triplets. It is remarked that the SOC path is only symbolized in (b), realistic requirements are discussed later (compare Fig. 1.9).

three-orbital model is characterized by just two excitations: one MLCT and one LC transition between the corresponding MOs (Fig. 1.6a).

In Section 1.3.1, it has been shown that each of these excitations results in one singlet and one triplet state. The electronic ground state is a singlet (Fig. 1.6b). Furthermore, according to the distinct spatial differences of the respective electron distributions in the involved orbitals, the exchange interactions – and thus the singlet–triplet splittings – differ strongly [see Eq. (3)]. For the π - and π^* -orbitals of the ligands which are in the focus of this chapter, $\Delta E(^1\pi\pi^* - ^3\pi\pi^*)$ is of the order of 10^4 cm^{-1} (1.24 eV). On the other hand, $\Delta E(^1MLCT - ^3MLCT)$ is much smaller, as the electron–electron interaction of the two electrons being distributed over the d -orbital and the spatially separated π^* -orbital, respectively, is weaker. According to Ref. [70], $\Delta E(^1MLCT - ^3MLCT)$ is about 3000 cm^{-1} (0.37 eV), or even smaller. With this information, an energy level diagram is obtained as depicted in Fig. 1.6b.

Although the model for organo-transition metal compounds as presented in Fig. 1.6 is greatly simplified, it may still be used for an orientation and some general conclusions or helpful rules of thumb:

- In general, a HOMO/LUMO model does not contain singlet or triplet states.
- The relative positions of HOMO-1 and HOMO do not allow to predict the energy sequence of the corresponding triplet states directly. Figure 1.6 shows that ${}^3\text{LC}$ can be the lowest state, although the HOMO–HOMO-1 sequence may suggest that ${}^3\text{MLCT}$ might be the lowest state. This behavior is related to the difference in energy between HOMO and HOMO-1, which may be small in comparison to the energy difference between the exchange integrals.
- The number of states is quite large, even for this simple model. Eight states are obtained, two singlets (${}^1\text{LC}$, ${}^1\text{MLCT}$) and $2 \times 3 = 6$ triplet substates (${}^3\text{LC}$, ${}^3\text{MLCT}$) (neglecting double excitations, for example, to $d^2(\pi^*)^2$ configurations).
- The eight states can mix quantum mechanically induced by electron–electron interaction between the different configurations (configuration interaction, CI) and by SOC.¹³⁾ Especially, SOC between ${}^1\text{MLCT}$ and ${}^3\text{MLCT}$ and CI between ${}^3\text{MLCT}$ and ${}^3\text{LC}$ will alter the properties of the lowest triplet state (see Section 1.3.3.3). A splitting of the zero-order ${}^3\text{LC}$ state into substates (ZFS) will result, the transitions between these and the ground state will become more allowed, the emission decay time will decrease, the photoluminescence quantum yield is mostly increased, and the spectra change, etc. (see Section 1.4.2. and Refs. [5, 70, 73, 74]).

1.3.3.2 Extended MO Model and Energy States

The simple model as discussed in Section 1.3.3.1 will certainly not be applicable for describing experimental results with sufficient quantitative precision. In particular, the number of electronic states is far from being realistic. This message is illustrated in Fig. 1.7 on the basis of two approaches, applied to discuss the example of $\text{Ir}(\text{ppy})_3$. In a first introductory step, the discussion is restricted only to MLCT transitions; this approach is displayed in the inner frame of Fig. 1.7. Some group theory will help to find the number of d- and π^* -orbitals and, subsequently, the number of resulting energy states. In the electronic ground state, $\text{Ir}(\text{ppy})_3$ has C_3 point group symmetry [113] and probably also in the lowest triplet state [114, 115].¹⁴⁾ In C_3 symmetry, the 5d-orbitals of t_{2g} representation split into

- 13)** SOC is particularly important for third row transition metal complexes with open 5d shells. It increases approximately with Z^4 , Z being the atomic number.
- 14)** In Refs. [70, 73, 74, 114] it has been shown by low-temperature investigations that in homoleptic organo-transition metal compounds the lowest triplet state is

delocalized over the three ligands and the metal. However, this result is only valid for a sufficiently large metal-induced ligand–ligand coupling. This coupling increases with a growing MLCT character of the lowest triplet state. A measure for this property represents the amount of ZFS (see also Sections 1.3.3.3 and 1.4). For example,

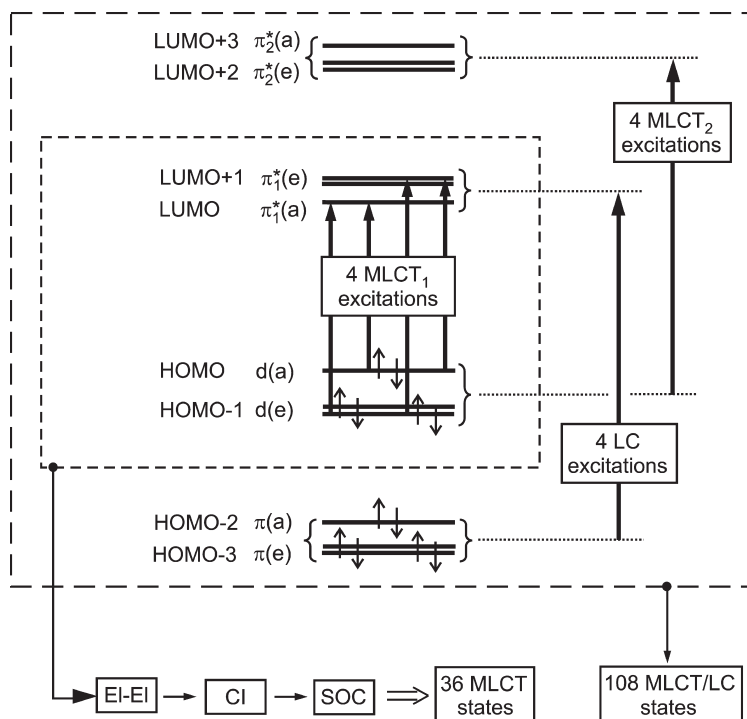


Fig. 1.7 Frontier orbitals, MLCT, and LC excitations and resulting number of states. Inner frame: In a simple model system for an organo-transition metal compound, such as $\text{Ir}(\text{ppy})_3$ with a C_3 symmetry, the four MLCT_1 excitations lead to 36 states. Outer frame: An

extension of the number of frontier orbitals by additional inclusion of four LC and four MLCT_2 transitions results in 108 states. About 70 states are expected to be within 8000 cm^{-1} (1 eV), just above the lowest triplet state [124].

two sets of d-orbitals – that is, a non-degenerate a and a doubly degenerate e representation. Due to the $5d^6$ configuration of Ir^{3+} , these orbitals are occupied by two and four electrons, respectively, giving the HOMO and HOMO-1 (Fig. 1.7, inner frame). The adequate, symmetry-adapted lowest unoccupied MOs result from the π_1^* -orbitals of the three (ppy)-ligands. Combinations of these lead, similarly, to one MO of a and two MOs of e representation, giving the LUMO and LUMO+1. It should be noted that these group theoretical considerations do not allow determination of the sequence of the respective MOs, as shown in Fig. 1.7. The energy ordering of the MOs has been adopted from Ref. [116]. It should be

for $\text{Pt}(\text{thpy})_2$ and $[\text{Ru}(\text{bpy})_3]^{2+}$ with $\Delta E(\text{ZFS}) = 16\text{ cm}^{-1}$ [70] and 61 cm^{-1} [73, 74], respectively, we have shown that the excited state is delocalized, whereas for $[\text{Pt}(\text{bpy})_2]^{2+}$ or $[\text{Rh}(\text{bpy})_3]^{3+}$ with $\Delta E(\text{ZFS}) < 1\text{ cm}^{-1}$, we found ligand-centered localized situations [73, 74]. For $\text{Ir}(\text{ppy})_3$, $\Delta E(\text{ZFS})$ amounts to

83 cm^{-1} [115]. According to this large value – and thus very large MLCT character – the assumption of having a delocalized triplet is well justified. Consequently, the C_3 symmetry is probably maintained for the lowest excited triplet.

further mentioned that a similar model was presented more than 20 years ago for $[\text{Ru}(\text{bpy})_3]^{2+}$ (compare Refs. [117, 118] and Ref. [74], p. 174).

According to the four different MOs shown in the inner frame of Fig. 1.7, four MLCT_1 transitions are obtained.¹⁵⁾ The effects of electron–electron interaction give the excited states (see Sections 1.3.1 and 1.3.3.1). For example, the HOMO–LUMO transition of type $d(e)^4 d(a)^2 \rightarrow d(e)^4 d(a)^1 \pi_1^*(a)^1$ leads to one singlet and one triplet – that is, to four states including triplet substates. Similarly, the three other MLCT_1 transitions $d(e)^4 d(a)^2 \rightarrow d(e)^4 d(a)^1 \pi_1^*(e)^1$, $d(e)^4 d(a)^2 \rightarrow d(a)^2 d(e)^3 \pi_1^*(a)^1$, and $d(e)^4 d(a)^2 \rightarrow d(a)^2 d(e)^3 \pi_1^*(e)^1$ result in an additional 32 states (including substates and counting doubly degenerate states twice). The resulting states of same symmetry will interact quantum mechanically due to CI, which is a consequence of electron–electron interaction. Moreover, SOC between singlets and triplets, as well as between different triplets, will lead to further energy shifts and splittings. This quantum mechanical mixing strongly alters the photophysical properties of the triplet substates, and is also the origin of the ZFS. As a consequence of these mixings, assignments as singlets or triplets (e.g., as $^1\text{MLCT}$ or $^3\text{MLCT}$) might not be fully adequate, especially if extensive mixings, such as in third period transition metal compounds, occur. However, the triplet character of the very lowest substate is usually almost maintained (see Section 1.3.3.3).

The total number of states, which result from the four MLCT_1 electron transitions, is 36. For $\text{Ir}(\text{ppy})_3$, if having a C_3 symmetry, 12 states would be doubly degenerate (representation E) and 12 would be non-degenerate (representation A). (Compare the situation described for $[\text{Ru}(\text{bpy})_3]^{2+}$ in Ref. [74], p. 175.) If, on the other hand, $\text{Ir}(\text{ppy})_3$ sits, for example, in a host cage which allows only a lower symmetry than C_3 – as would be expected for a complex doped into an amorphous matrix – the doubly degenerate E states will split. A splitting of E states would also be expected, if the complex were to be distorted in the excited state to a lower symmetry. This can occur due to polarization effects. Such distortions may be dissimilar for different excited states of the same complex. The 36 states are expected to lie within an energy range of about 4500 cm^{-1} (0.56 eV) (compare Ref. [116], Table 1.3). In this context, reference should also be made to the valuable model calculation carried out by Kober and Meyer [118] for $[\text{Ru}(\text{bpy})_3]^{2+}$.

Clearly, chemical intuition tells us that the model presented above (the inner frame of Fig. 1.7) will not lead to a successful description of organo-transition metal compounds. Specifically, their properties are extensively influenced or even dominated by ligand-centered contributions (compare, for example, Refs. [71–74, 82–88, 116–134]). These LC components are also very important for $\text{Ir}(\text{ppy})_3$ [116, 123, 124]. Hence, the lower-lying occupied π -MOs and the higher-lying unoccupied π^* -MOs must also be taken into account. Combinations of the respective ligand orbitals lead to occupied $\pi(a)$ and $\pi(e)$ as well as to unoccupied $\pi_2^*(e)$ and $\pi_2^*(a)$ -MOs (Fig. 1.7, outer frame). The inclusion of the π_2^* -MOs is justified by estimates

¹⁵⁾ These MLCT transitions can be described by the configuration $d^6 \rightarrow d^5(\pi^*)^1$. Transitions of the type of $d^6 \rightarrow d^4(\pi^*)^2$ lie at much higher energy, and are not taken into account in this model.

carried out for $[\text{Ru}(\text{bpy})_3]^{2+}$, for which the corresponding π_2^* -MOs lie only about 6000 cm^{-1} (0.74 eV) above the π_1^* -MOs (see Refs. [117, 118, 132] and [74], p. 175). Consequently, a more realistic model is extended by several additional frontier orbitals and the respective electron transitions. Beside the four MLCT_1 transitions, shown in the inner frame of Fig. 1.7, the extended model additionally provides four LC and four MLCT_2 transitions. Following the quantum mechanical procedures outlined above, $3 \times 36 = 108$ states are obtained. For completeness, it should be noted that 36 of these states are doubly degenerate E states, which split into 72 substates, if $\text{Ir}(\text{ppy})_3$ does not sit on a strict C_3 site. Interestingly, Nozaki's [124] theoretical approach can only achieve results which are comparable to experimental values, by taking as many as 50 singlets and 50 triplets (200 states) into account. Thus, the large number of states within a relatively small energy range, giving a high density of states, is a property that is characteristic of the systems under consideration.

Obviously, the total number of states depends on the number of chromophoric ligands. For example, for $\text{Ir}(\text{ppy})_2(\text{LL})$ with only two chromophoric (ppy) ligands, one obtains only 64 non-degenerate electronic states in an equivalent model and energy range (2×24 MLCT and 16 LC states). In general, one electronic excitation between two non-degenerate MOs gives one singlet and one triplet state with three substates – that is, four states. Thus, the number of resulting states can easily be determined, if the number of frontier orbitals is increased.

It should be emphasized that the resulting states are mostly quantum mechanically mixed. For example, the lowest triplet substates contain triplet and singlet admixtures of higher-lying states, of which the singlets carry the allowednesses of the transitions to the electronic ground state. These admixtures determine ZFSs, radiative rates, emission quantum yields, and spectral forms (see Sections 1.3.3.3 and 1.4.2).

Although the model presented has not been quantitatively applied to organo-transition metal compounds, it has the advantage of fitting well to the intuition of organo-metal chemistry. It offers good insight into the different MOs involved, their spatial distributions, and the resulting states. Thus, trends may be identified and can be used to predict changes in photophysical properties according to chemical variations, such as the effects of electron-donating or -withdrawing substitutions, variations of conjugation lengths, influence of the ligand field strength, variation of the oxidation and reduction potentials (compare, for example, Ref. [133]). Even predictions of SOC routes are possible (compare Sections 1.3.3.3 and 1.4.2). However, for quantitative descriptions, the current research is mainly based on *ab-initio* methods, such as time-dependent density functional theory (TDDFT) [116, 120–128] or CASSCF/CASPT2 [119]. Although the predictions of transition energies, singlet–triplet oscillator strengths, number of low-lying triplet states, and ZFS energies are mostly not very reliable, or may even not be determined at all, the calculated results are still helpful in understanding certain photophysical trends. However, the predictions become much more realistic when SOC effects are taken into account, and this point forms the subject of the next section.

1.3.3.3 Spin–Orbit Coupling, Triplet Substates, Zero-Field Splitting, and Radiative Decay Rates

The emission properties of an organo-transition metal complex are largely determined by the individual characteristics of the three substates of the lowest triplet term T_1 . The substates do not represent “pure” states, but contain contributions from singlets and triplets of other configurations due to CI and SOC. In particular, the mixed-in singlet components provide the required radiative rates and allowednesses of the optical transitions to the electronic singlet ground state. Further, specific interactions with higher-lying states lead to individual, but different, energy stabilizations of the substates. Thus, a splitting of the T_1 state, the ZFS, results.¹⁶⁾ It is subject of the subsequent considerations to develop some insight into the quantum mechanical description of these effects [82, 122, 124, 134–136].

The energies of the triplet substates can be calculated – at least in principle – by use of second order spin–orbit perturbation theory. The zero-order wavefunctions ϕ_{S_n} , ϕ_{T_n} and energies E_{S_n} , E_{T_n} of singlet and triplet states are considered as known before inclusion of spin–orbit interaction. They are, for example, determined by DFT calculations [122, 127, 128, 134]. The energies $E(i)$ of the resulting (perturbed) triplet substates of T_1 with $i=I, II, III$ can be expressed by:^{17),18)}

$$E(i) = E_{T_1} + \sum_{S_n} \frac{|\langle \phi_{S_n} | \hat{H}_{SO} | \phi_{T_1(i)} \rangle|^2}{E_{T_1} - E_{S_n}} + \sum_{T_n} \frac{|\langle \phi_{T_n(j)} | \hat{H}_{SO} | \phi_{T_1(i)} \rangle|^2}{E_{T_1} - E_{T_n}} \quad (4)$$

wherein \hat{H}_{SO} is the SOC Hamiltonian. S_n and $T_n(j)$ refer to those singlet states and triplet substates j , which have the same symmetry representation as the individual substate **I**, **II**, and **III**, respectively. Otherwise, the matrix elements of Eq. (4) vanish.¹⁹⁾

The energies $E(I)$, $E(II)$, and $E(III)$ of the individual triplet substates **I**, **II**, and **III** will energetically be stabilized, though differently, depending on the magnitudes of the respective matrix elements. Distinct shifts of $E(I)$, $E(II)$, and $E(III)$ can only occur, if SOC between the involved states is significant. This is only possible, if ${}^{1,3}\text{MLCT}$ (${}^{1,3}\text{d}\pi^*$) contributions are present in the respective wavefunctions. The resulting differences of the energy shifts give $\Delta E(\text{ZFS})$. In other words, an experimentally determined value of a relatively large $\Delta E(\text{ZFS})$ displays directly the importance of ${}^{1,3}\text{MLCT}$ (${}^{1,3}\text{d}\pi^*$) components in the wavefunction of the corresponding

16) The small effects of spin–spin coupling, giving splittings of the order of 0.1 cm^{-1} , are neglected here.

17) Note that the DFT calculations do not yield the exact states of the systems including full configuration interaction (CI) before taking SOC into account; hence, additional CI may lead to further mixing and energy shifts.

18) We simplify the notation in view of the fact that one has to use degenerate perturbation

theory. Also note that first-order contributions are vanishing.

19) The matrix elements can only be non-zero, if the grouptheoretical product of all components contains the totally symmetric representation. Since \hat{H}_{SO} is totally symmetric, the two interacting states have to belong to the same representation. For experts, it should be noted that we refer here to representations of the double group.

triplet state.²⁰ Clearly, this is connected with all other photophysical implications, which are induced by the involved MLCT character, such as an increase in the radiative rate and the photoluminescence quantum efficiency, and/or changes of the emission spectra (see below and Section 1.4.2). “Relatively large” in this context means $\Delta E(\text{ZFS}) \geq 2 \text{ cm}^{-1}$ – that is, the ZFS is more than one order of magnitude larger than splittings induced by spin–spin interactions.

The radiative rate constant $k^r(i)$ of the transition from triplet substate i , with $i = \text{I, II, III}$, to the electronic ground state represents a crucial quantity for the luminescence of an organometallic compound. The rate can be expressed by use of perturbation theory as [77, 134].

$$k^r(i) = \text{const} \times \bar{\nu}^3 \times \left| \sum_{S_n} \frac{\langle \phi_{S_n} | \hat{H}_{\text{SO}} | \phi_{T_1(i)} \rangle}{E_{T_1} - E_{S_n}} \times \langle \phi_{S_0} | \mathbf{er} | \phi_{S_n} \rangle \right|^2 \quad (5)$$

where $\bar{\nu}$ is the transition energy in cm^{-1} and \mathbf{er} the electric dipole operator. The zero-order wavefunctions ϕ_{S_n} and the zero-order energies E_{T_1} , E_{S_n} have been defined above. Similarly as discussed before, the wavefunction ϕ_{S_n} of a higher-lying singlet state must have the same symmetry representation as the respective triplet substate **I**, **II**, or **III**. Otherwise $\langle \phi_{S_n} | \hat{H}_{\text{SO}} | \phi_{T_1(i)} \rangle$ vanishes, and mixing between the corresponding states does not occur.

The radiative rate $k^r(i)$ depends not only on the values of the matrix elements $\langle \phi_{S_n} | \hat{H}_{\text{SO}} | \phi_{T_1(i)} \rangle$ – that is, the spin–orbit interactions of the respective triplet substate with higher-lying singlets – but also on the allowednesses of the transitions from S_0 to the interacting singlet states S_n . The corresponding transition dipole moments can be calculated by using DFT approaches [122, 123, 128].

With an increase of the radiative decay rate k^r , usually also an increase of the photoluminescence quantum yield ϕ_{PL} is found, according to

$$\phi_{\text{PL}} = \frac{k^r}{k^r + k^{\text{nr}}} \quad (6)$$

wherein k^r can be expressed for one specific triplet substate by use of Eq. (5). k^{nr} is the non-radiative decay rate, which depends on the energy gap between the emissive triplet state and the electronic ground state (the “energy gap law”), the number of coupling and deactivating vibrational modes, and on the coupling strength of the corresponding modes. For further information, see Refs. [78, 79].

In Section 1.3.3.2 it was shown that a very large number of excited states exists in an adjacent small energy range. In principle, these can all contribute to the lowest triplet substates via spin–orbit interaction, if the corresponding symmetries

20) It should be noted that small $\Delta E(\text{ZFS})$ values might, hypothetically, result also from large, but near-equal energy shifts of all three substates due to significant ^{1,3}MLCT components in each case. Corresponding mixings to the sublevels of T_1 , at least of

singlet character, would, for example, directly be displayed in shortening of the emission decay times (at low temperature). However, such a situation has never been found experimentally [5, 70, 73, 74].

fit. However, many of these SOC routes contribute little, and they can be neglected compared to a few dominating spin-orbit interactions. Interestingly, in a series of investigations, relatively simple rules for important SOC routes have been elucidated [82, 122, 136] and recently summarized by K. Nozaki et al. [122]. These considerations are based on estimating the magnitudes of matrix elements. In particular, if they do not involve one-center integrals on the transition metal center, the magnitudes are small.²¹⁾ [137] For example, SOC between ${}^3\text{LC}({}^3\pi\pi^*)$ and ${}^1\text{MLCT}({}^1d\pi^*)$ states involves only two-center integrals on the metal. Consequently, SOC between these states is small and therefore, cannot be responsible for the relatively large effects of SOC found in organo-transition metal compounds [82, 136] (Fig. 1.8a). On the other hand, one-center SOC integrals can induce effective SOC between ${}^1\text{MLCT}({}^1d\pi^*)$ and ${}^3\text{MLCT}({}^3d\pi^*)$ states [82, 136], as is symbolized in Fig. 1.8b. (Note that additional requirements have to be taken into account, see Fig. 1.9.)

From experimental investigations it is known, however, that many organo-transition metal complexes have (perturbed) ${}^3\text{LC}({}^3\pi\pi^*)$ states as lowest triplets which exhibit relatively high radiative transition rates to the electronic ground state. Obviously, these triplets involve significant ${}^1\text{MLCT}({}^1d\pi^*)$ components (compare, for example, Refs. [5, 70, 73, 74]). Therefore, another mechanism must be effective. Indeed, according to Miki et al. [82, 122, 136], an important indirect SOC mixing route is efficient. It is proposed that the ${}^1\text{MLCT}({}^1d\pi^*)$ state interacts by SOC with the ${}^3\text{MLCT}({}^3d\pi^*)$ state which on its part interacts by CI with the ${}^3\text{LC}({}^3\pi\pi^*)$ state (CI results from electron-electron interaction). According to Nozaki's investigations [122, 124], this indirect coupling route is the dominant mechanism for the intense photoluminescence of many complexes. The corresponding SOC route is shown in Fig. 1.8c, and was depicted earlier in Fig. 1.6b.

To summarize, an effective SOC between triplet substates and higher-lying states can lead to significant magnitudes of the matrix elements $\langle\phi_{\text{sn}}|\hat{H}_{\text{SO}}|\phi_{\text{T}(i)}\rangle$, for example, and thus lead to appreciable $\Delta E(\text{ZFS})$ values [Eq. (4)] and radiative rates $k^{\text{r}}(i)$ to the ground state [Eq. (5)], in contrast to zero-order ${}^3\text{LC}({}^3\pi\pi^*)$ states.

With regards to the discussed SOC route between ${}^3\text{MLCT}({}^3d\pi^*)$ and ${}^1\text{MLCT}({}^1d\pi^*)$ (Fig. 1.8b), a restriction must be accounted for. Again, based on the arguments of the dominance of one-center integrals, a ${}^3\text{MLCT}$ state only couples effectively with a ${}^1\text{MLCT}$ state, if the configurations of both states involve the *same* π^* -orbital, but *different* d -orbitals [137]. For quasi-octahedral d^6 complexes, these d -orbitals belong to the t_{2g} manifold. This additional requirement for an effective SOC is illustrated

21) From the usual rules for evaluating matrix elements of one-electron operators between Slater determinants (see Ref. [137], Table 2.3), one may conclude that single excitations $\Psi_1 \rightarrow \Psi_2^*$ and $\Psi_3 \rightarrow \Psi_4^*$ can only lead to non-vanishing contributions of SOC (approximated as a one-electron operator), when $\psi_1 = \psi_3$ or $\psi_2^* = \psi_4^*$. Thus, for example, SOC between states resulting from $d \rightarrow \pi^*$ and $\pi \rightarrow d^*$ vanishes. On the other

hand, for $d \rightarrow \pi^*$ and $\pi \rightarrow \pi^*$ excitations to the same π^* orbital, matrix elements of the form $\langle d|\hat{H}_{\text{SO}}|\pi\rangle$ are obtained, while for $d_1 \rightarrow \pi^*$ and $d_2 \rightarrow \pi^*$ excitations, integrals of the form $\langle d_1|\hat{H}_{\text{SO}}|d_2\rangle$ occur. The former is at least a two-center integral and, hence, small, while the latter is a one-center integral and can be large. Note, that diagonal matrix elements of the type $\langle d_1|\hat{H}_{\text{SO}}(\text{metal})|d_1\rangle$, involving the same d_1 orbital, vanish.

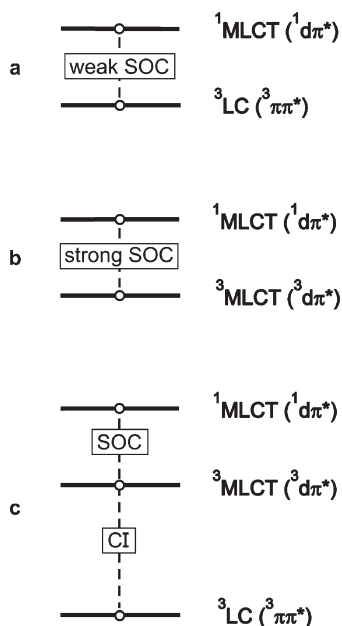


Fig. 1.8 Spin-orbit coupling (SOC) routes. (a) SOC between $^3\text{LC} (^3\pi\pi^*)$ and $^1\text{MLCT} (^1\text{d}\pi^*)$ does not involve one-center integrals on the transition metal center, and is therefore weak. (b) SOC between $^3\text{MLCT} (^3\text{d}\pi^*)$ and $^1\text{MLCT} (^1\text{d}\pi^*)$ states can be strong under

specific conditions, which are discussed in Fig. 1.9. (c) Indirect SOC mixing routes can be efficient, if the $^1\text{MLCT} (^1\text{d}\pi^*)$ state interacts with the $^3\text{MLCT} (^3\text{d}\pi^*)$ state, which couples with $^3\text{LC} (^3\pi\pi^*)$ by configuration interaction (CI). Compare also the Refs. [82, 122, 136].

in Fig. 1.9. For complexes with a distorted O_h symmetry, the three t_{2g} -orbitals can split and three MLCT transitions are obtained, if we consider in this simplifying illustration only one π^* -orbital, for example of a compound with just one chromophoric ligand (Fig. 1.9a) These transitions lead to three $^1\text{MLCT}$ and three $^3\text{MLCT}$ states (12 substates; compare Section 1.3.3.1). In Fig. 1.9b, the states are depicted in separate diagrams to illustrate the required coupling routes. According to footnote 21 and to Ref. [122], SOC between states of the same configuration is weak, while it can be significant between singlets and triplets of different configurations.²²⁾

Theoretical studies of phosphorescence properties of organo-transition metal compounds require a thorough inclusion of effects of SOC, in particular with respect to the lowest triplet states. A recent investigation by Nozaki [124] approaches this challenge by using – as an example – a strongly simplified model system for

22) It should be noted again that SOC between the corresponding states is only possible, if they belong to the same irreducible representation (same symmetry). Often, the

point group symmetry of a complex is only slightly distorted to C_1 . In this case, however, symmetry restrictions of the parent group might still be valid.

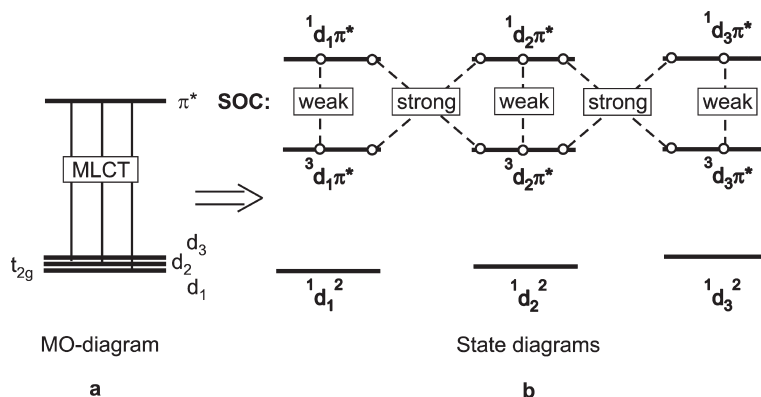


Fig. 1.9 Spin-orbit coupling (SOC) between ${}^3\text{MLCT}({}^3d\pi^*)$ and ${}^1\text{MLCT}({}^1d\pi^*)$ states. SOC can be effective under specific conditions; that is, it can be strong, if the same π^* -orbital but different d-orbitals are involved, otherwise SOC is weak. These considerations are based on estimates of SOC matrix elements (see

Refs. [82, 122, 136] and Footnote 21). Note that, in addition to the depicted coupling routes, strong SOC can also occur between ${}^3d_3\pi^*$ and ${}^1d_1\pi^*$ states. This illustration is greatly simplified, as only one π^* -orbital is taken into account in this model.

$\text{Ir}(\text{ppy})_3$. In these studies, zero-order wavefunctions and energies were obtained from TDDFT calculations. Subsequently, spin-orbit interactions were included as perturbation. The evaluation of the SOC matrix elements was carried out by considering only one-center spin-orbit integrals in the scope of the arguments presented above and depicted in Figs. 1.8 and 1.9. The resulting description of properties of the three lowest-lying triplet substates fits in several respects to experimental observations. From the very long emission decay time of substate I of $\tau_1 = 145 \mu\text{s}$, this state can be assigned to be an almost pure triplet [115]. Indeed, according to Ref. [124], substate I consists of about 92% of the T_1 contribution (which carries very high MLCT character) and of components of higher-lying triplets (T_4 : $\approx 5\%$ and T_6 : $\approx 2\%$) but – in the scope of this approximation – of no singlet character.

It seems to be a more general property of organo-transition metal compounds that the lowest triplet substate I represents an almost pure triplet. This has been observed experimentally for many compounds (compare the reviews in Refs. [5, 70, 73, 74]), and also found by *ab-initio* calculation for $[\text{Ru}(\text{bpy})_3]^{2+}$, $[\text{Os}(\text{bpy})_3]^{2+}$, and $\text{Ir}(\text{ppy})_3$ [124]. Presumably, this behavior is indicative of an energetically proximate higher-lying triplet, which is responsible for stabilizing substate I, obviously without providing singlet character.

The situation concerning singlet admixtures is different for the two higher-lying substates II and III of $\text{Ir}(\text{ppy})_3$ [124]. These represent also mainly T_1 substates (II: $\approx 92\%$ and III: $\approx 94\%$), and have different contributions of admixed higher-lying triplet components (II: $\approx 5\%$ T_4 , III: $\approx 2\%$ T_6). However, the substates II and III contain in addition small admixtures of higher-lying singlets. Specifically, these

admixture provide the required allowednesses for efficient emission (**II** $\approx 2\%$ S_4 , **III**: $\approx 1\%$ S_5). The calculated prediction of the sequence of radiative rates $k^r(\text{I}) < k^r(\text{II}) < k^r(\text{III})$ is also in accordance with the experimentally determined emission decay rates. We found $k(\text{I}) = 6.9 \times 10^3 \text{ s}^{-1}$, $k(\text{II}) = 91 \times 10^3 \text{ s}^{-1}$, and $k(\text{III}) = 1330 \times 10^3 \text{ s}^{-1}$ (compare Section 1.6 and Ref. [115]). The fact that $k^r(\text{III}) > k^r(\text{II})$ in spite of a somewhat larger singlet admixture in substate **II** can be explained by a larger oscillator strength (allowedness) of the transition $S_0 \rightarrow S_5$ in comparison to $S_0 \rightarrow S_4$ (see Fig. 1.3 of Ref. [124]).

Calculations as carried out in Ref. [124] led also to interesting conclusions concerning the number of states, which was the subject of discussion in Section 1.3.3.2. For example, according to Ref. [124], an “accurate” calculation requires the inclusion of up to 200 states (50 singlets and 50 triplets). Further, for the example of $\text{Ir}(\text{ppy})_3$, it has been found [124] that about 70 states lie within a range of 8000 cm^{-1} (1 eV) above the emitting triplet. This corresponds to a range from $\approx 20\,000 \text{ cm}^{-1}$ (500 nm) to $28\,000 \text{ cm}^{-1}$ (357 nm).

For the application of an organo-transition metal compound in an OLED, it is required that the radiative rate of the transition from the lowest triplet state to the singlet ground state is large. This is connected with a short emission decay time and – if non-radiative deactivation is not dominating – with a high photoluminescence quantum yield. From this requirement, it can be concluded that SOC routes to the lowest triplet state – i.e. to the specific triplet substates – have to be as effective as attainable. Presumably, when paying attention to the relatively simple rules for efficient SOC routes (Figs. 1.8 and 1.9), and when applying adequate chemical engineering, it might be possible to obtain compounds with distinctly improved efficiencies. This subject is re-addressed in Section 1.4.2.

1.4

Zero-Field Splitting (ZFS) of the Emitting Triplet, Photophysical Trends, and Ordering Scheme for Organo-Transition Metal Compounds

The emission of organo-transition metal compounds discussed in the scope of this chapter occurs from the lowest excited triplet state T_1 to the electronic ground state S_0 . Without including spin-orbit coupling, this transition is strictly forbidden. However, for third row transition metal compounds, SOC to the lowest triplet can be very important and can induce drastic effects, such as substantial splittings of the triplet into substates and an increase of radiative decay rates. Due to this latter effect, the phosphorescence quantum yields may reach almost 100%. Several other photophysical properties of the compounds will also be altered distinctly (see below). In Section 1.3.3.3, we have already illustrated SOC routes which are responsible for these effects. In particular, changes of the radiative rates of transitions from the three T_1 substates **I**, **II**, and **III** to the electronic ground state S_0 (**0**) can be calculated using Eq. (5), whilst splitting of the T_1 state (ZFS) can be determined using Eq. (4). However, sufficiently accurate quantum mechanical calculations, which include SOC, remain difficult to perform. Thus, an empirical ordering

scheme can be helpful for assessing the materials' properties. We have shown that especially the size of the total ZFS [$\Delta E(\text{ZFS})$] represents a valuable parameter to assess or even predict the important photophysical properties of organometallic compounds [5, 70, 74, 114]. According to Eq. (4) and the subsequent discussions, $\Delta E(\text{ZFS})$ displays directly the importance of $^1\text{MLCT}$ ($^1\text{d}\pi^*$) components in the corresponding triplet state. In other words, a value of $\Delta E(\text{ZFS})$ of more than $1\text{--}2\text{ cm}^{-1}$ is connected with $^1\text{d}\pi^*$ components in the wavefunctions of the triplet substates. In particular, significant $\Delta E(\text{ZFS})$ values are representative of significant $^1\text{MLCT}$ components in the corresponding triplet state. Usually, states with very large MLCT character (very large $\Delta E(\text{ZFS})$ values) are termed as MLCT states, although it is generally known that substantial π and π^* character of the ligand(s) is also involved. These considerations are summarized schematically in Fig. 1.10.

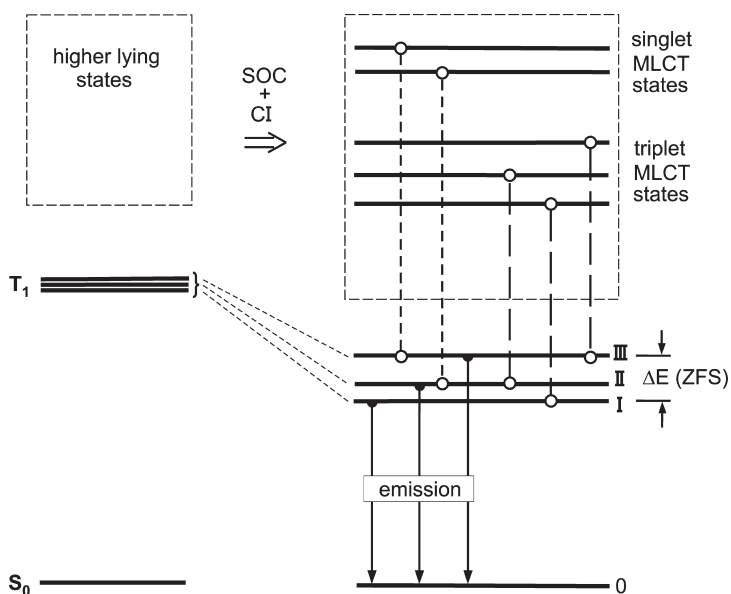


Fig. 1.10 Schematic diagram showing that spin-orbit coupling (SOC) and configuration interaction (CI) of the three triplet substates I, II, and III with higher-lying states result in energy shifts, splittings $\Delta E(\text{ZFS})$ of the lowest triplet T_1 state – also at zero magnetic field – and changes of the $T_1 \leftrightarrow S_0$ transition probabilities. Rules for the required mixings are discussed in Sections 1.3.3.3 and 1.4.2. Specifically, the allowedness of a transition between a triplet substate and the electronic ground state is governed by an admixture of

$^1\text{MLCT}$ character to the corresponding substate according to Eq. (5). Consequently, the magnitudes of the radiative rates are determined by the significance of the $^1\text{MLCT}$ admixtures and by the involved (admixed) singlet state – that is, its transition probability to the electronic ground state. Frequently, the very lowest triplet substate does not contain distinct singlet components and therefore is usually an almost pure triplet and hence long-lived (compare Refs. [5, 70, 73, 74, 124]).

1.4.1

Ordering Scheme

Figure 1.11 summarizes a series of compounds which are arranged according to an increasing $\Delta E(\text{ZFS})$ of the emissive triplet state; the corresponding chemical

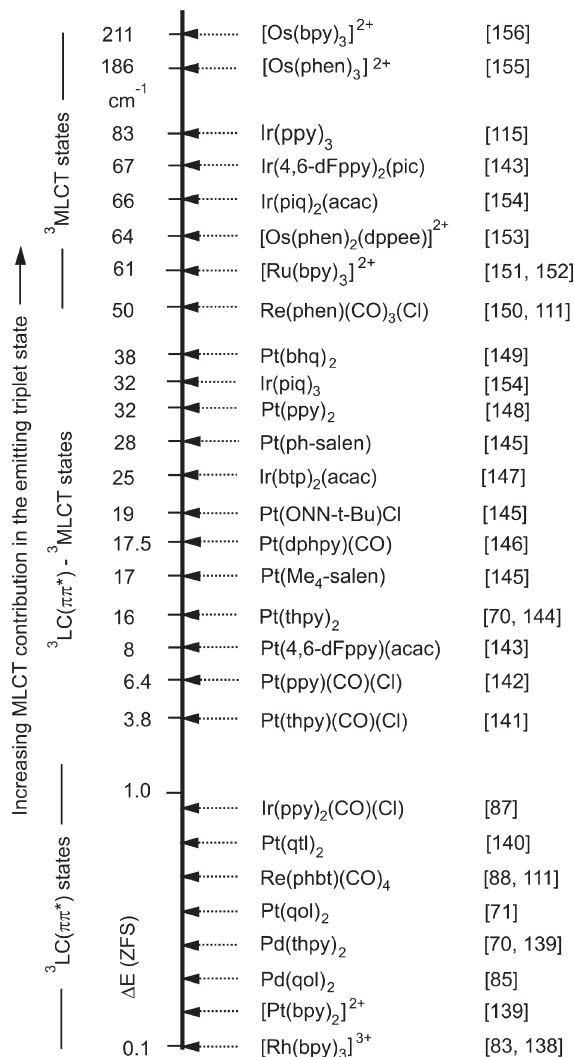


Fig. 1.11 The compounds are arranged according to an increasing splitting of the emitting triplet state into substates (zero-field splitting, ZFS). The splitting reflects the ^{1,3}MLCT character in the corresponding wavefunctions. The related structure formulae are shown in Fig. 1.12. The listed references

refer to reports in which the corresponding $\Delta E(\text{ZFS})$ values have been provided. Note that the size of ZFS can also depend on the individual environment of the emitter compound (compare Section 1.10). For most emitters the positions of compounds with $\Delta E(\text{ZFS}) \leq 1 \text{ cm}^{-1}$ are only roughly estimated.

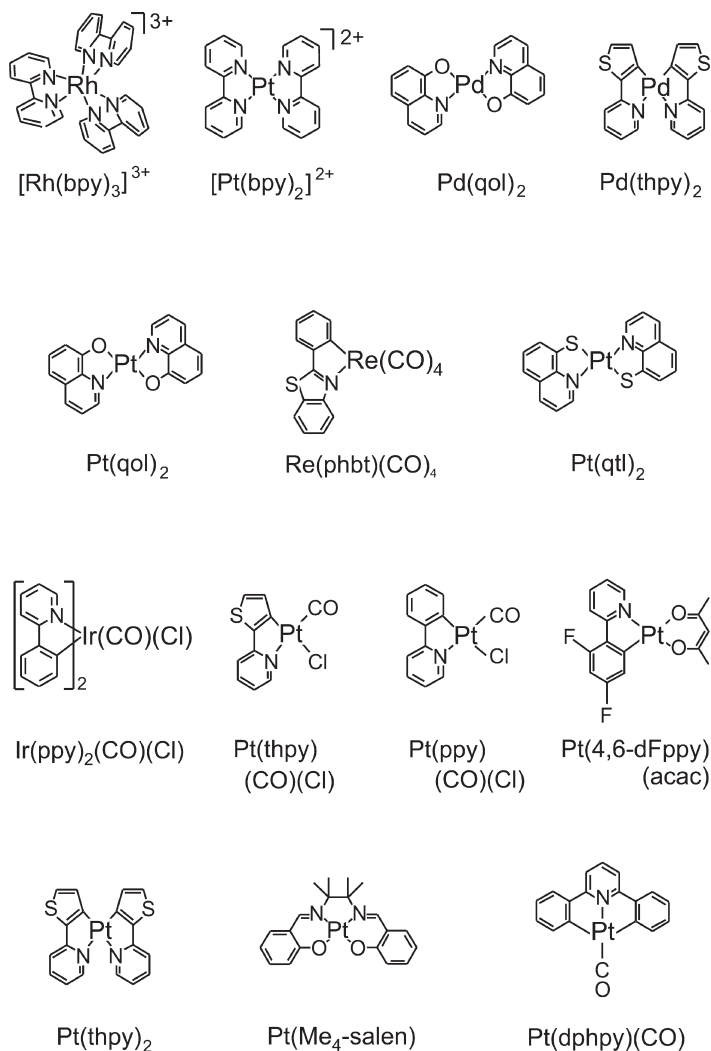


Fig. 1.12 Structure formulae of emitter compounds shown in Fig. 1.11 and discussed in this chapter.

structures are illustrated in Fig. 1.12. The $\Delta E(\text{ZFS})$ values have been determined mostly by use of optical high-resolution spectroscopic methods. A representative example, of how this procedure is carried out, is discussed in Section 1.5 for $\text{Pt}(\text{thpy})_2$ with an intermediate magnitude of ZFS. On the other hand, compounds with very small $\Delta E(\text{ZFS})$ values of much less than 1 cm^{-1} , such as $[\text{Rh}(\text{bpy})_3]^{2+}$ [83, 84, 138], $\text{Pd}(\text{qol})_2$ [85], and $\text{Pd}(\text{thpy})_2$ [139] have been investigated by using double-resonance methods, in particular optically detected magnetic resonance (ODMR). Details of the procedure are provided elsewhere (e.g., [83] and references therein.)

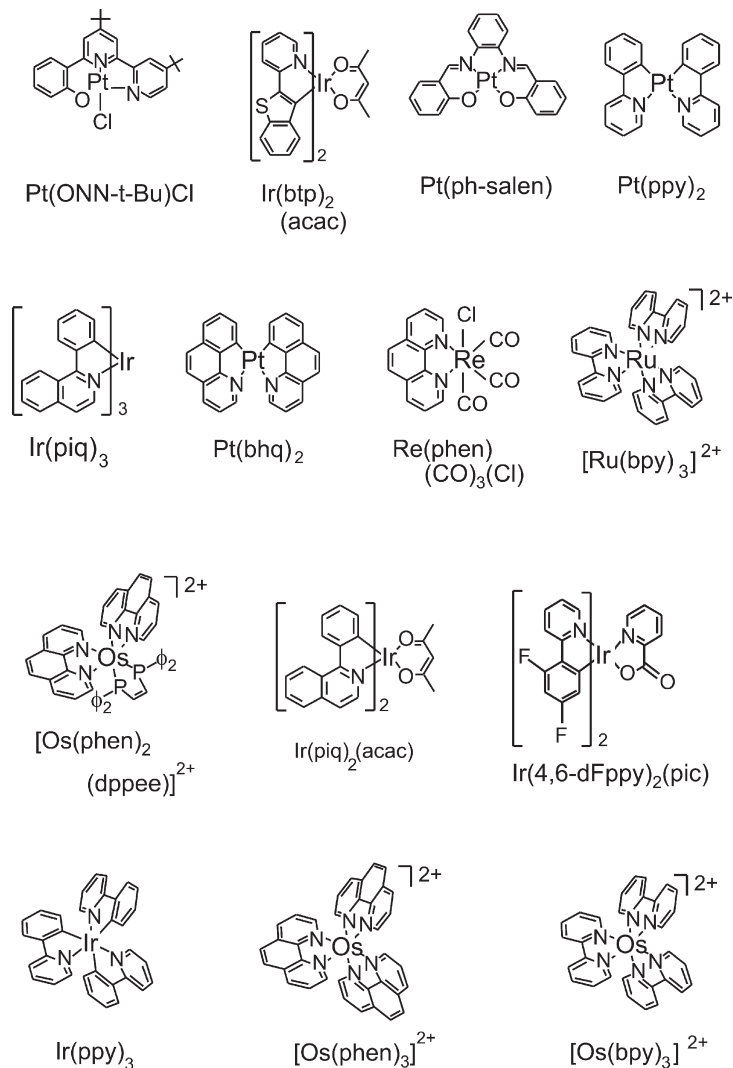


Fig. 1.12 Continued

In several cases, however, it is not possible to obtain highly resolved spectra, despite the ZFS being large. This behavior is connected to a relatively large inhomogeneity of the emitter compound in the applied host and/or to a large electron-phonon coupling of the singlet-triplet transition (compare Section 1.11). In these cases, an indirect method of determining the temperature dependence of the emission decay time was applied, and from a fit of these data valuable information concerning the triplet state can be obtained. A corresponding example is presented in Section 1.6, illustrating the properties of $\text{Ir}(\text{ppy})_3$.

According to the discussions presented above, an increasing ZFS of the emitting triplet state, as shown in the ordering scheme of Fig. 1.11, is connected with an increasing MLCT component in this triplet state. Compounds with $\Delta E(\text{ZFS})$ values of less than $\approx 1 \text{ cm}^{-1}$ exhibit largely ligand-centered ${}^3\text{LC}({}^3\pi\pi^*)$ emitting states. The triplets of complexes in the intermediate range cannot be regarded as pure ${}^3\text{LC}$ states. The ${}^3\text{LC}({}^3\pi\pi^*)$ character is significantly perturbed by ${}^{1,3}\text{d}\pi^*$ admixtures. Those emitters with larger $\Delta E(\text{ZFS})$ values $> 50 \text{ cm}^{-1}$ than about are normally termed and assigned as ${}^3\text{MLCT}$ emitters. Extensive literature concerning MLCT assignments is available, for example for $[\text{Ru}(\text{bpy})_3]^{2+}$ [117, 118, 124, 132, 157, 158], $\text{Ir}(\text{ppy})_3$ [115, 116, 123, 124], and $[\text{Os}(\text{bpy})_3]^{2+}$ [70, 74, 124, 125, 159].

1.4.2

Photophysical Properties and ZFS

The magnitude of the ZFS parameter increases in the range shown in Fig. 1.11 by more than a factor of 2000. This is a result of essential changes of the wavefunctions of the lowest triplet substates due to increasing SOC of ${}^3\pi\pi^*$ states with ${}^{1,3}\text{d}\pi^*$ states. The effectiveness of this coupling is given by specific SOC routes which are discussed in Section 1.3.3.3.

An interesting trend is found, when inspecting the ordering scheme of Fig. 1.11, which shows that large $\Delta E(\text{ZFS})$ values (e.g., $> 40 \text{ cm}^{-1}$) have not yet been found for quasi-square planar organometallic Pt(II) compounds, whereas for quasi-octahedral Re(I), Os(II), Ir(III) – and even for second row transition metal compounds, such as Ru(II) complexes – much larger $\Delta E(\text{ZFS})$ values are not unusual. This behavior can be explained on the basis of the SOC considerations carried out in Section 1.3.3.3. For *quasi-octahedral complexes*, it follows from Fig. 1.9 (middle) that the lowest ${}^3\text{MLCT}({}^3\text{d}\pi^*)$ state can experience strong SOC with ${}^1\text{MLCT}({}^1\text{d}\pi^*)$ states (and other ${}^3\text{MLCT}({}^3\text{d}\pi^*)$ states, not depicted in Fig. 1.9) which involve different d-orbitals of the t_{2g} manifold. For compounds with distorted O_h symmetry, the resulting orbital energies are still rather proximate. On the other hand, for *quasi-square planar* Pt(II) complexes, the lowest ${}^1\text{MLCT}$ and ${}^3\text{MLCT}$ states result from the same $d_{z^2} \rightarrow \pi^*$ excitation. Therefore, SOC between these states can be neglected, since for an effective SOC, the involvement of different d-orbitals is required (see Section 1.3.3.3). For square-planar complexes, the corresponding candidates would be the d_{xz} , d_{yz} orbitals; however, these are energetically significantly separated from the d_{z^2} orbitals. Estimates of the orbital energies lead to differences of about 4000 cm^{-1} (0.5 eV) or more for ligands with high D_q values [160, 161]. Accordingly, the energy denominator, which also governs the effectiveness of SOC [see Eqs. (4) and (5)], is significantly larger than for octahedral compounds. These considerations are summarized schematically in the upper part of Fig. 1.13, specified as MLCT range, for ${}^{1,3}\text{MLCT}$ states of octahedral and square planar complexes, respectively.

For many compounds, however, the lowest triplet is largely of $\text{LC}(\pi\pi^*)$ parentage. This is found, for example, for $\text{Pt}(\text{thpy})_2$ (see Refs. [70, 119] and Section 1.5) and for $\text{Ir}(\text{btp})_2(\text{acac})$ (see Ref. [147] and Section 1.8). Again schematically, this

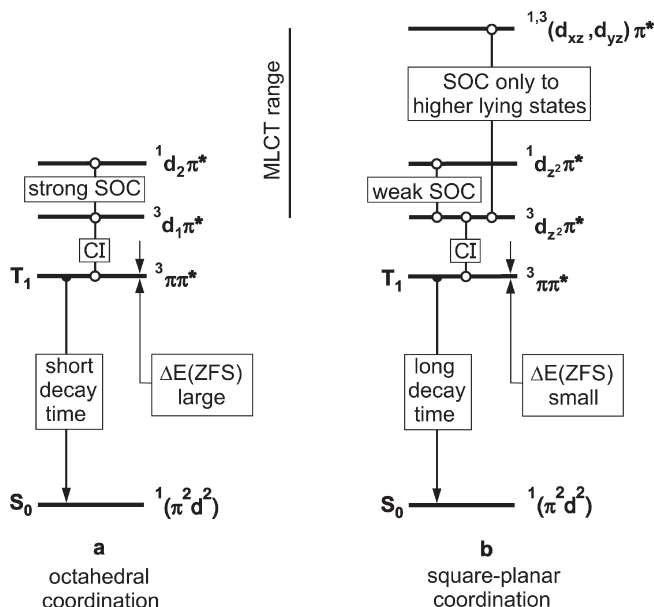


Fig. 1.13 Schematic and simplified comparison of quasi-octahedral to quasi-square planar triplet emitter compounds. The spin-orbit coupling (SOC) routes are different and thus can result in distinctly different zero-field splittings $\Delta E(\text{ZFS})$ and radiative emission decay rates. These considerations apply to

$^3\text{MLCT}(^3d\pi^*)$ states (higher-lying states specified by the MLCT range) as well as to $^3\text{LC}(^3\pi\pi^*)$ states. The $^3\text{LC}(^3\pi\pi^*)$ states mix with $^3\text{MLCT}(^3d\pi^*)$ states by configuration interaction (CI), and thus are indirectly altered by changes of SOC routes.

situation is taken into account in Fig. 1.13 by introducing a low-lying $^3\text{LC}(^3\pi\pi^*)$ state. Although, for this state, SOC to $^1,3\text{MLCT}$ states is negligible (no one-center integrals on the metal; Section 1.3.3.3), CI – representing an electron–electron interaction – can induce mixing of $^3\text{MLCT}(^3d\pi^*)$ and $^3\text{LC}(^3\pi\pi^*)$ states. Hence, this mixing modifies the lowest states of $^3\pi\pi^*$ parentage and induces a $^1d\pi^*$ admixture indirectly.

Thus, the differences of the SOC routes of quasi-octahedral compared to quasi-square planar complexes refer not only to the $^3\text{MLCT}(^3d\pi^*)$ manifolds but also to the $^3\text{LC}(^3\pi\pi^*)$ states. From these considerations it follows that the magnitudes of $\Delta E(\text{ZFS})$ and of the radiative decay rates can be larger for quasi-octahedral than for quasi-square planar complexes. These specific coupling routes often lead to relatively short emission decay times of quasi-octahedral emitters. Therefore, quasi-octahedral complexes might, in several cases, be better suited as OLED emitters than quasi-square planar compounds. In particular, this can be important if the OLEDs are operated at high current densities. These considerations explain – in part – the attractiveness of Ir(III) complexes for application in OLED devices.

The effectiveness of SOC is – as outlined above – very important for the photo-physical properties of the emitting compounds. At this point it becomes instructive to discuss the further consequences of an increasing perturbation by comparing two structurally similar compounds, Pd(thpy)₂ and Pt(thpy)₂, which exhibit strongly different MLCT character of the T₁ states. This is, in part, due to the different values of SOC constants of the involved 4dπ* and 5dπ* perturbations of the Pd(II) and the Pt(II) compound, respectively. The properties of these compounds are further compared to those of a typical small purely organic molecule with low-lying ³ππ* and ¹ππ* states. For these states, SOC is of minor importance. Such molecules have already been investigated in great detail (e.g., see Refs. [77–79]).

In the subsequent comparison, trends are illustrated which are connected with an increasing perturbation of the ^{1,3}ππ* states by ^{1,3}dπ* states (compare Fig. 1.14).

1.4.2.1 Singlet–Triplet Splitting

Organic molecules of the type of ligands which are of interest in this investigation usually exhibit singlet–triplet splittings $\Delta E(S_1 - T_1)$ of the order of typically 10^4 cm^{-1} (1.24 eV). This splitting is mainly given by the exchange interaction, which is

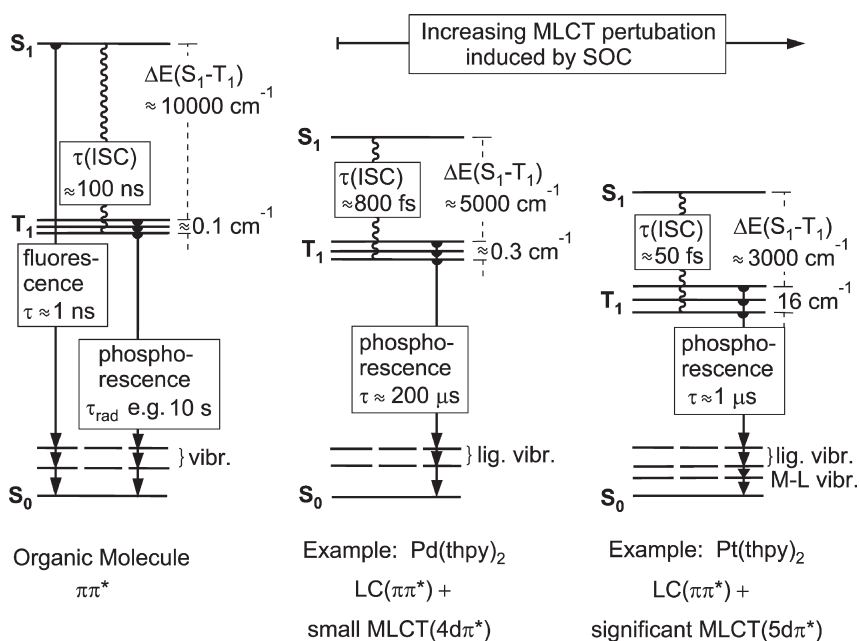


Fig. 1.14 Photophysical properties of two organo-transition metal emitters compared to those of a representative purely organic molecule. The emissive triplets of Pd(thpy)₂ and Pt(thpy)₂ exhibit small and significant MLCT admixtures to the LC($\pi\pi^*$) states, respectively. The positions of the compounds

in the ordering scheme and the molecular structures are found in Figs. 1.11 and 1.12. The properties of Pd(thpy)₂ and Pt(thpy)₂ are discussed and compared in detail in Ref. [70]. lig. vibr. = ligand vibrations; M-L vibr. = metal–ligand vibrations.

essentially determined by the extensions and overlap of the involved wavefunctions (see Section 1.3.1). For the organometallic $\text{Pd}(\text{thpy})_2$, a value of 5418 cm^{-1} is found [70].²³⁾ The emissive triplet of this compound has been classified – based on experimental investigations [70, 139, 162, 163] and later also by CASPT2 *ab-initio* calculations [119] – as being mainly of $\text{LC}(\pi\pi^*)$ character with small $\text{MLCT}(4d\pi^*)$ admixtures. Therefore, the compound is found in the lower range of the ordering scheme of Fig. 1.11. On the other hand, for $\text{Pt}(\text{thpy})_2$ with significant $\text{MLCT}(5d\pi^*)$ admixtures to the ${}^3\text{LC}(\pi\pi^*)$ state [70, 144], the amount of $\Delta E(S_1 - T_1)$ is reduced to 3278 cm^{-1} (Fig. 1.14) [70].²³⁾ Obviously, enhancing the metal character in the corresponding wavefunctions increasingly reduces the $\Delta E(S_1 - T_1)$ value. Due to the higher MLCT character, the electronic wavefunctions extend over a larger spatial region of the complex involving, in the case of $\text{Pt}(\text{thpy})_2$, both ligands and the metal [114]. This is connected to an on average larger spatial separation between the interacting electrons. Thus, electron–electron interactions – and especially the exchange interaction – are reduced. This explains both the reduction of $\Delta E(S_1 - T_1)$ and the lowering of the S_1 state for compounds with higher metal character (Fig. 1.14).

1.4.2.2 Intersystem Crossing Rates

After excitation of the singlet state S_1 , either optically or by electron-hole recombination, an organic molecule can exhibit an efficient fluorescence ($S_1 \rightarrow S_0$ emission) with a time constant of the order of 1 ns. In competition to this process, ISC can at least principally depopulate the S_1 state. However, the time constant of $\tau(\text{ISC})$ is often much larger (order of 100 ns or even more) than the radiative decay time of the S_1 state, and hence ISC does not effectively quench the fluorescence (Fig. 1.14). On the other hand, in organo-transition metal complexes, the ISC time is drastically reduced due to singlet–triplet mixing induced by SOC, and due to the reduction of the energy separation $\Delta E(S_1 - T_1)$. According to this latter effect, the number of vibrational quanta, which are needed for the relaxation process, is reduced and thus the ISC probability becomes higher. For example, already for a compound, such as $\text{Pd}(\text{thpy})_2$, with a relatively small MLCT perturbation in the wavefunction of the T_1 state and a halved $\Delta E(S_1 - T_1)$ value, ISC is by five orders of magnitude faster (800 fs [70]) than in typical organic compounds with ${}^1\pi\pi^*$ and ${}^3\pi\pi^*$ states. For $\text{Pt}(\text{thpy})_2$ with a higher metal perturbation, the process is again much faster ($\tau(\text{ISC})$ at $\approx 50 \text{ fs}$ [70]) (Fig. 1.14). It should be noted that the term “intersystem crossing” loses its specific meaning, if SOC is large and effectively mixes singlet and triplet states. In this situation, IC and ISC cannot be discriminated.

In conclusion, the process of ISC in organometallic compounds with transition metal ions is fast and efficient for all compounds shown in Fig. 1.11. The quantum efficiency for this process is usually almost one (e.g., see Ref. [164]). Therefore, an emission from the S_1 state is not observable – a property which is the basis of the triplet harvesting effect, as discussed in Section 1.2.2.

²³⁾ This value refers to the specific site of $\text{M}(\text{thpy})_2$ investigated in *n*-octane.

1.4.2.3 Emission Decay Time and Photoluminescence Quantum Yield

In purely organic molecules, the $S_0(\pi^2) \leftrightarrow T_1(\pi\pi^*)$ transition is strongly forbidden, and the radiative decay time can be of the order of 10 s [78]. On the other hand, non-radiative processes are in general much faster, and consequently phosphorescence from the T_1 state is totally quenched at ambient temperature. With increasing SOC, the radiative decay time of the $T_1 \rightarrow S_0$ transition is reduced and thus the radiative path can compete with the non-radiative one [compare Eq. (5)]. Interestingly, already a relatively small singlet admixture to the ${}^3\text{LC}({}^3\pi\pi^*)$ state – or, more exactly, to the respective triplet substate – increases the radiative transition probability drastically (see Section 1.3.3.3). For example, for $\text{Pd}(\text{thpy})_2$ the emission decay time may be as short as $\tau_{\text{mean}} = 235 \mu\text{s}$ (τ_{mean} is the mean decay time for the three triplet substates with $\tau_{\text{I}} = 1200 \mu\text{s}$, $\tau_{\text{II}} = 235 \mu\text{s}$, and $\tau_{\text{III}} = 130 \mu\text{s}$ [163]). For $\text{Pt}(\text{thpy})_2$, with a significant MLCT admixture to the lowest ${}^3\text{LC}$ state, the decay time is even reduced by six to seven orders of magnitude as compared to a purely organic emitter, and an emission decay time of the order of $1 \mu\text{s}$ is found (Fig. 1.14) [70].²⁴⁾

In summary, for organometallic compounds the radiative decay rates between the states T_1 and S_0 can be tuned by several orders of magnitude as compared to organic emitters. This is induced by an increase of SOC of the triplet substates to higher-lying singlets. Particularly short decay times are found, if effective SOC occurs to singlets S_n , which exhibit high transition probabilities of the transitions $S_0 \rightarrow S_n$ [Eq. (5)]. Thus, for such compounds, the radiative processes can well compete with or even exceed the non-radiative ones [compare Eq. (6)]. Consequently, organo-transition metal compounds can exhibit efficient emission (phosphorescence) with high ϕ_{PL} values. Therefore, these compounds are well suited as emitter materials for OLEDs.

1.4.2.4 Zero-Field Splitting – Summarizing Remarks

Triplet states split generally into substates, and this is also valid for purely organic molecules. However, for these one finds only small values of ZFS of the order of 0.1 cm^{-1} ($1.2 \times 10^{-5} \text{ eV}$) which result from spin–spin couplings between the electrons in the π and π^* orbitals, respectively (e.g., see Refs. [77, 82–84]). On the other hand, in organo-transition metal compounds SOC will modify the properties of the emitting triplet state by mixing in higher-lying states of singlet and triplet character. Yet, small admixtures may have drastic consequences: For example, increase of the ISC rate and of the phosphorescence decay rate (see the previous subsections) by orders of magnitude are found, whereas the ZFS is not drastically altered by small MLCT perturbations. Well-studied examples of this behavior are $[\text{Rh}(\text{bpy})_3]^{3+}$ and $\text{Pd}(\text{qol})_2$ [72, 83, 85]. However, larger MLCT perturbations due to stronger SOC lead to appreciable ZFSs, as was discussed in Section 1.3.3.3 [Eq. (4)] and depicted in Fig. 1.11. For the example of $\text{Pt}(\text{thpy})_2$, we find $\Delta E(\text{ZFS}) = 16 \text{ cm}^{-1}$, which lies in the intermediate range.

²⁴⁾ The emission decay behavior of emitter compounds is of crucial importance for an understanding of the triplet state properties and the compounds' applicability in OLEDs.

Therefore, decay properties will be discussed later in detail (see Sections 1.6, 1.7, 1.8, 1.9.2.3, and 1.10.3).

Importantly, the individual triplet substates **I**, **II**, and **III** can have very different photophysical properties with regard to radiative decay rates, vibronic coupling, coupling to the environment, emission quantum yields, population and relaxation dynamics due to spin–lattice relaxation (SLR), and sensitivity with respect to symmetry changes (see also the following sections). At ambient temperature, the individual properties are largely smeared out, and in general only an averaged behavior is identified. Nevertheless, the individual triplet substates still determine the overall emission properties (compare Section 1.11). It should be noted that the magnitude of $\Delta E(\text{ZFS})$ and the properties of the substates are not independent of the environment or the matrix cage in which the emitter complex is situated. This behavior is discussed in more detail in Section 1.10.

1.4.2.5 Emission Band Structures and Vibrational Satellites

At ambient temperature, the phosphorescence of organo-transition metal compounds usually consists of superimposed spectra, which stem from the different triplet substates (see Section 1.9). An individual spectrum which results from only one specific substate is normally composed of a transition at the electronic origin (0-0 transition), a large number of vibrational satellites, and of in part overlapping low-energy satellites which – due to electron–phonon coupling – involve low-energy vibrations of the complex in its environment (lattice cage). Moreover, all of these individual transitions are masked by homogeneous broadening effects, and consequently at ambient temperature only a broadband emission normally results (compare Section 1.11). On occasion, residual, moderately resolved structures occur, which stem from overlapping vibrational satellites (not necessarily from progressions). Interestingly, at low temperature and under suitable conditions, these structures can often be well resolved and characterized (compare Section 1.9). Based on this type of investigation, it follows that the vibrational satellite structure is also influenced by the MLCT component in the electronic states [165]. Specifically, the spectra of compounds with electronic transitions of mainly LC($\pi\pi^*$) character (small MLCT perturbation) are largely determined by satellites corresponding to ligand vibrations (fundamentals, combinations, progressions). However, with increasing MLCT character, low-energy vibrational satellites of metal–ligand character become more important (up to about 600 cm^{-1} from the electronic origin) [165] (Fig. 1.14). Thus, the emission spectrum (at ambient temperature) becomes less resolved and the maximum of the emission shifts away from the electronic 0-0 transition towards the metal–ligand vibrational satellites.

To summarize, metal participation (i.e. MLCT perturbation) in the emitting state leads to a slight shift of the unresolved emission maximum as compared to an LC-based spectrum with the same 0-0 transition energy. This is due to the occurrence of additional low-energy metal–ligand vibrational satellites which causes also a further smearing out of the spectrum.

1.4.2.6 Localization/Delocalization and Geometry Changes in the Excited Triplet State

The singlet–triplet transitions of compounds with small MLCT character (as shown in the lower part of Fig. 1.11) are usually confined to one of the ligands,

even if the formal symmetry of the complex would allow a delocalization over all of the ligands. This has been proven for $[\text{Rh}(\text{bpy})_3]^{3+}$ [72] and $[\text{Pt}(\text{bpy})_2]^{2+}$ [74] by use of the method of deuteration labeling [74, 114]. In contrast, for compounds with emissive $^3\text{MLCT}$ states such as $[\text{Ru}(\text{bpy})_3]^{2+}$ [166] and $[\text{Os}(\text{bpy})_3]^{2+}$ [167], it has been shown that the excited state is delocalized over the three ligands and the metal. This is even valid for $\text{Pt}(\text{thpy})_2$, in which the triplet state is largely of $\text{LC}(\pi\pi^*)$ character, but for which the metal orbital admixture induces sufficient coupling between the ligands to result in a delocalization of the lowest excited state [70, 114]. It should be noted that these results were obtained at low temperature for compounds doped into rigid matrices. (For a detailed discussion of this subject, see Ref. [74].)

Moreover, since the metal character or MLCT component in the triplet state – if sufficiently large – can induce a ligand–ligand coupling which delocalizes the excited state wavefunction, the metal contribution will also affect the geometry change that follows an excitation. This is indicated by the values of the Huang–Rhys parameters. For the localized situation in the above-mentioned compounds, a maximum Huang–Rhys parameter [70] of $S=0.3$ is found, whilst for compounds with delocalized triplets with larger (!) MLCT components this characteristic parameter is smaller by a factor of three to four [70, 74]. The description of S and the corresponding background information are presented in Section 1.9 [Eq. (21), see below]. Interestingly, geometry changes or reorganization effects which occur upon excitation of the emissive triplet states are small for almost all investigated complexes (in rigid matrices).

In conclusion, we point to an interesting observation. The organo-transition metal emitters, which have been applied in *efficient* OLEDs, exhibit $\Delta E(\text{ZFS})$ values greater than $\approx 10 \text{ cm}^{-1}$ ($1.2 \times 10^{-3} \text{ eV}$). It is indicated that for splittings above this magnitude, components of higher-lying singlet states in the emitting triplet sub-states can be large enough to induce the required radiative allowednesses, short emission decay times, and sufficiently high photoluminescence quantum yields.

1.5

Characterization of the Lowest Triplet State Based on High-Resolution Spectroscopy: Application to $\text{Pt}(\text{thpy})_2$

$\text{Pt}(\text{thpy})_2$ has been used as emitter dopant in OLEDs [168–170] and for generation of chemiluminescence [171], albeit less frequently than $\text{Ir}(\text{ppy})_3$ (Section 1.6) or $\text{Ir}(\text{btp})_2(\text{acac})$ (Section 1.8). Nevertheless, $\text{Pt}(\text{thpy})_2$ represents a highly illustrative example to demonstrate, how the triplet T_1 substates can be characterized by high-resolution spectroscopy. At this point, initially a survey is provided. Figure 1.15a shows the absorption spectrum below $\approx 50\,000 \text{ cm}^{-1}$ (6.2 eV) and the emission spectrum, both measured at ambient temperature (compare Refs. [172–174]). The features in absorption are typical structures which are related to strongly mixed MLCT/LC states (compare the CASPT2 treatment of Ref. [119]). The low-energy weak absorption peak near $\approx 580 \text{ nm}$, which overlaps with the emission, corre-

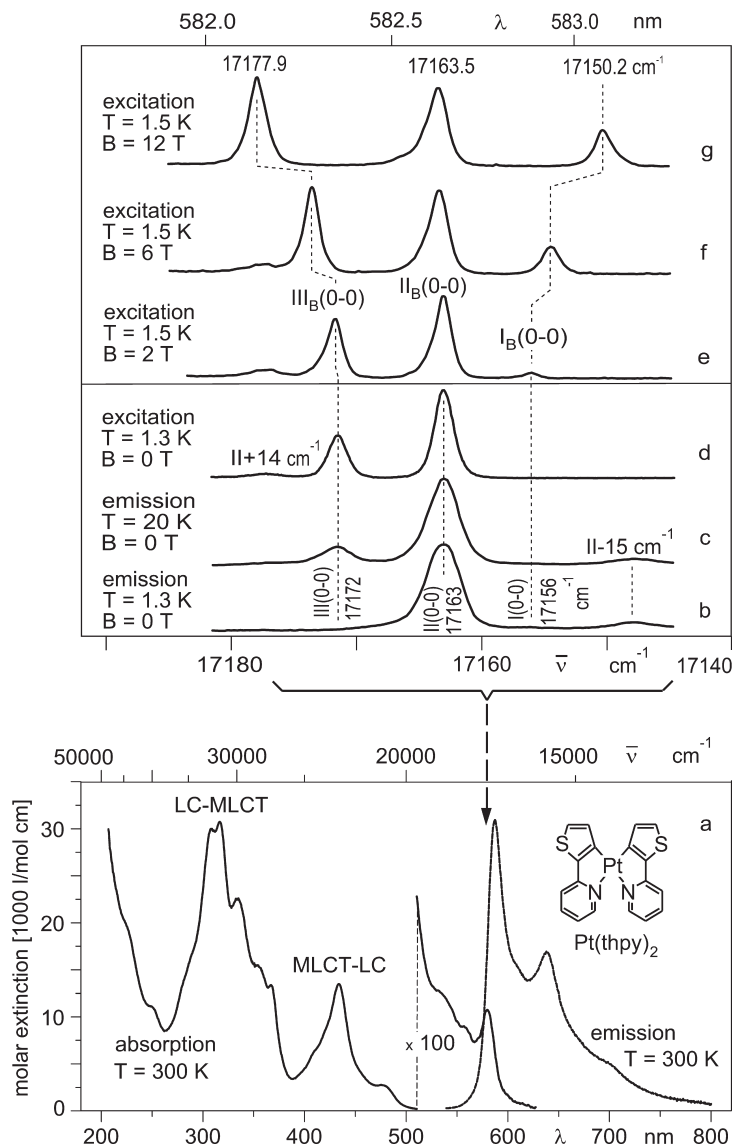


Fig. 1.15 Emission, excitation, and absorption of Pt(thpy)₂ at various temperatures and magnetic fields. (a) Compound dissolved in *n*-octane, $\lambda_{\text{exc}} = 457.9$ nm. (b–g) Pt(thpy)₂ dissolved in *n*-octane, ca. $\approx 10^{-5}$ mol L⁻¹. For experimental details, see Ref. [70].

sponds to the lowest triplet state T_1 . Already from this investigation, carried out at ambient temperature and showing the “allowedness” of the $S_0 \rightarrow T_1$ transition, it is expected that the T_1 state contains MLCT admixtures and is distinctly split into substates. Accordingly, it is within the focus of this section to illustrate, how

the ZFS can be determined and the substates as well as the corresponding electronic transitions to the ground state can be characterized. Clearly, the total emission spectrum from a triplet term consists almost generally not only of electronic 0-0 transitions, but additionally of vibrational and lattice mode satellites. In this section, attention is focused on the purely electronic 0-0 transitions, whereas in Section 1.9 the vibrational satellite structures will be discussed.

1.5.1

Highly Resolved Electronic Transitions

The transitions corresponding to the triplet substates **I**, **II**, and **III** can be well resolved by applying the methods of high-resolution and site-selective Shpol'skii²⁵⁾ spectroscopy at low temperatures. However, for Pt(thpy)₂, the three electronic transitions $\mathbf{0} \leftrightarrow \mathbf{I}$ (I(0-0)), $\mathbf{0} \leftrightarrow \mathbf{II}$ (II(0-0)), and $\mathbf{0} \leftrightarrow \mathbf{III}$ (III(0-0)) cannot be observed in the same spectrum (Fig. 1.15b–g). At $T=1.3$ K, the emission from substate **III** is frozen out and the transition $\mathbf{I} \leftrightarrow \mathbf{0}$ at the electronic origin I(0-0) is largely forbidden. Thus, only the electronic origin II(0-0) at $17\,163\text{ cm}^{-1}$ is found (Fig. 1.15b). Interestingly, this emission cannot be frozen out due to the relatively slow thermalization between the substates **I** and **II**. This behavior is a consequence of a long spin-lattice relaxation (SLR) time of $\tau_{\text{SLR}}=720\text{ ns}$ at $T=1.3\text{ K}$ (see Section 1.7). With a temperature increase, for example to $T=20\text{ K}$, substate **III** is populated and the III(0-0) emission grows in (Fig. 1.15c). On the other hand, an excitation spectrum measured at low temperature shows the two electronic transitions $\mathbf{0} \leftrightarrow \mathbf{II}$ and $\mathbf{0} \leftrightarrow \mathbf{III}$, but again, $\mathbf{0} \leftrightarrow \mathbf{I}$ is too weak to be detectable (Fig. 1.15d). However, the position of substate **I** can be located indirectly by a comparison of energies of infrared-active vibrations with energies of the vibrational satellites which are well resolved in the $T=1.3\text{ K}$ emission spectrum (see Section 1.9). It is shown that the vibrational satellites fit well, if the position of the electronic origin of substate **I** is set to $17\,156\text{ cm}^{-1}$. Indeed, a careful inspection of the 1.3 K emission spectrum shows that a very weak transition occurs at exactly this energy. The forbiddenness of this transition is displayed also in the long emission decay time of $\tau_1=110\text{ }\mu\text{s}$ [70].

An independent confirmation of the position of this origin I(0-0) is obtained, when a high magnetic field is applied. With increasing field strength, the electronic origin line $\text{I}_B(0-0)$ grows in due to a B-field-induced Zeeman interaction of substate **I** with higher-lying triplet substates (Fig. 1.15e–g). Distinct Zeeman shifts of the lines $\text{I}_B(0-0)$ and $\text{III}_B(0-0)$ are also observed. The interpretation of this behavior is straightforward, as a similar behavior has been observed for $[\text{Os}(\text{bpy})_3]^{2+}$ and has been thoroughly discussed in Refs. [74] (p. 223) and [177]. In particular, an extrapolation from high magnetic fields to zero field clearly allows one to confirm the position of $17\,156\text{ cm}^{-1}$ for the energy of the I(0-0) transition.

25) Alkanes, such as hexane, heptane, and octane, crystallize at low temperature as so-called Shpol'skii matrices [175, 176]. For many neutral molecules, these matrices represent relatively inert hosts. The guest molecules, doped at low concentrations of

10^{-4} to $10^{-5}\text{ mol L}^{-1}$, substitute host molecules. In suitable situations, one obtains highly resolved spectra also of organo-transition metal compounds [70–72, 85, 86, 139–144, 162, 163].

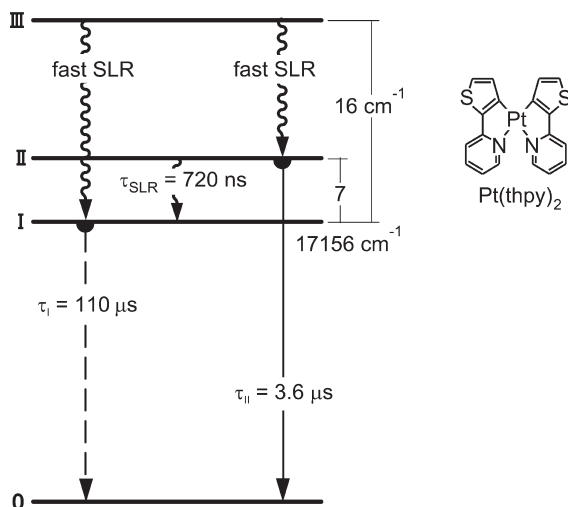


Fig. 1.16 Energy level diagram and decay times of the T_1 substates of $\text{Pt}(\text{thpy})_2$ dissolved in *n*-octane. The energy values and splittings result from highly resolved spectra, as discussed in Section 1.5. The decay properties are discussed in Section 1.7. SLR = spin-lattice relaxation.

In summary, using the methods of high-resolution emission and excitation spectroscopy at various temperatures and under the application of high magnetic fields, allows identification of the three triplet substates of the T_1 term. In particular, an observation of the Zeeman effects confirms that the observed origins do not belong to different sites of the emitter in the host, but represent substates of the same T_1 parent term. The magnetic field effects will be discussed in more detail in a case study applied to $\text{Ir}(\text{btp})_2(\text{acac})$ in Section 1.8.

Figure 1.16 displays the resulting energy level diagram for $\text{Pt}(\text{thpy})_2$; several specific decay times taken from Ref. [70] are also given (compare Section 1.7). In particular, it is found that the total $\Delta E(\text{ZFS})$ amounts to 16 cm^{-1} . Thus, according to Section 1.4 and Fig. 1.11, it can be concluded that $\text{Pt}(\text{thpy})_2$ belongs to the group of compounds with an emitting ^3LC state which, however, is significantly perturbed by MLCT admixtures.

1.5.2

Symmetry and Grouptheoretical Considerations

The crystal structure determination [178] has shown that the point group symmetry of $\text{Pt}(\text{thpy})_2$ deviates from a C_{2v} symmetry, because the molecule is not planar. Also, a geometry optimization based on a density functional theory (DFT) calculation resulted in a structure which deviates from the C_{2v} symmetry. However, the calculations showed also that the corresponding energy minimum is shallow and

that the C_{2v} structure has only a slightly higher energy ($1.7 \text{ kcal mol}^{-1}$, $\approx 600 \text{ cm}^{-1}$ or 0.074 eV) [119]. This energy is so small, however, that intermolecular forces between the matrix cage and the $\text{Pt}(\text{thpy})_2$ compound can easily have an effect on the geometry of the doped molecule. In particular, $\text{Pt}(\text{thpy})_2$ might also become planar. This hypothesis is indicated due to the following considerations:

- Matrix cages consisting of *n*-octane or other *n*-alkanes host planar molecules with preference [175, 176, 179].
- The electronic forbiddenness of the transition $\mathbf{0} \leftrightarrow \mathbf{I}$ is unusually pronounced (Fig. 1.15b), if compared to other compounds; this indicates that the transition is spin and symmetry forbidden.
- After a relatively fast cooling rate of $\text{Pt}(\text{thpy})_2$ dissolved in *n*-octane, the corresponding transition is found to be more allowed and thus well observable at $T = 1.3 \text{ K}$; this indicates that the forbiddenness of the transition $\mathbf{0} \leftrightarrow \mathbf{I}$ depends on the specific cage geometry.
- Unsymmetric vibrations induce distinct radiative deactivation paths (appearance of strong “false origins”; compare Section 1.9.2.1).

Hence, it is assumed that $\text{Pt}(\text{thpy})_2$ is flattened under the experimental situation, at which the spectrum of Fig. 1.15b has been measured, and that $\text{Pt}(\text{thpy})_2$ adopts a C_{2v} symmetry. Under this assumption, an illustrative grouptheoretical consideration can be carried out. It is a specific property of the C_{2v} symmetry group²⁶⁾ that only one representation exists – the A_2 representation – for which the transition to the electronic ground state of A_1 symmetry is electric dipole forbidden [180] and therefore is very sensitive to symmetry-breaking processes. Accordingly, we assign the triplet substate \mathbf{I} to an A_2 representation. Thus, with the additional spin–flip–forbiddenness of the triplet–singlet transition, one can understand, why the transition $\mathbf{I} \leftrightarrow \mathbf{0}$ is so weak and almost non-observable at zero magnetic field.

Ab-initio calculations of Ref. [119] lead to an assignment of the lowest triplet (with a calculated transition energy of $\approx 18200 \text{ cm}^{-1}$) to 3A_1 (in C_{2v}). From this representation it follows under SOC (not included in Ref. [119]) that in the C_{2v} double group the triplet splits into the three substates A_2 , B_1 and B_2 (compare Ref. [180]). Thus, if the assignment of Ref. [119] holds, one obtains just one sublevel with the symmetry A_2 for state \mathbf{I} , while the two other triplet substates \mathbf{II} and \mathbf{III} have B_1 and B_2 representations, respectively. An individual assignment of these two other states is not yet possible. Both transitions between the ground state A_1 and these triplet substates B_1 and B_2 are formally dipole-allowed [180].²⁷⁾

²⁶⁾ The subsequent classification is carried out in the C_{2v} double group which takes into account orbital and spin symmetries [108, 180].

Indeed, the experiment shows that both substates **II** and **III** can directly be excited from the ground state (Fig. 1.15d). Moreover, the ambient temperature absorption spectrum (Fig. 1.15a) indicates that the corresponding electronic 0-0 transitions together exhibit an absorption coefficient of $\approx 90 \text{ L mol}^{-1} \cdot \text{cm}$. Thus, the transitions to the two triplet substates **II** and **III** are considerably allowed.

The model presented above can be discussed further with respect to the radiative rates $k'(i)$ (with $i = \text{I, II, III}$) as expressed by Eq. (5). Specifically, the T_1 substates **II** and **III** of $\text{Pt}(\text{thpy})_2$ – exhibiting B_1 and B_2 symmetry, respectively – couple with higher-lying singlets also of $B_1(^1B_1)$ and $B_2(^1B_2)$ representation. Thus, these two transitions between the substates **II** and **III** and the electronic ground state **0** borrow their allowednesses from the $^1B_1 \leftrightarrow ^1A_1$ and $^1B_2 \leftrightarrow ^1A_1$ transition, respectively ($\langle \phi_{s_0} | \epsilon r | \phi_{s_n} \rangle$ term of Eq. (5)). On the other hand, the transition between the electronic ground state and a higher-lying 1A_2 state is dipole-forbidden and thus cannot provide transition probability to the transition $\text{I} \leftrightarrow \text{0}$.

It is expected that the considerations discussed in relation to a planar C_{2v} symmetry remain at least approximately valid for a slightly distorted geometry.

In conclusion, for most of the organo-transition metal compounds it has been found that the lowest triplet substate **I** represents an almost pure triplet – that is, SOC to higher-lying singlets is unimportant (compare Section 1.3.3.3). Hence, the SOC matrix elements $\langle \phi_{s_n} | \hat{H}_{\text{SO}} | \phi_{T_1(i)} \rangle$ representing the first term of Eq. (5), are very small. This is also valid for substate **I** of $\text{Pt}(\text{thpy})_2$. In addition, the second term of Eq. (5) vanishes in a strict C_{2v} symmetry (or is very small in a slightly distorted symmetry) due to the dipole forbiddenness of the intensity-providing transition between the singlets. Consequently, the model proposed above allows an understanding of why the transition between the T_1 substate **I** and the electronic ground state **0** is difficult to detect.

1.6

Characterization of the Lowest Triplet State Based on Decay Time Measurements: Application to $\text{Ir}(\text{ppy})_3$

$\text{Ir}(\text{ppy})_3$ represents a well-known and efficient OLED emitter; therefore, it is of great interest to characterize the emitting triplet state of this and related compounds in detail. Until now, however, it has not been possible to obtain highly resolved and thus highly informative emission or excitation spectra, even when

27) Due to the restricted accuracy of the CASPT2 calculations [119], it is not excluded that the substates of a different triplet term, namely of 3B_2 , can become the lowest ones under inclusion of spin-orbit coupling. 3B_2 would lead to A_1 , A_2 , and B_1 substate symmetries in C_{2v} . In this case, we would

also assign substate **I** to the A_2 symmetry. The corresponding transition between the ground state A_1 and the sublevel of symmetry A_2 would again be forbidden, while transitions to the substates **II** and **III** of A_1 and B_1 representations, respectively, would formally be dipole allowed.

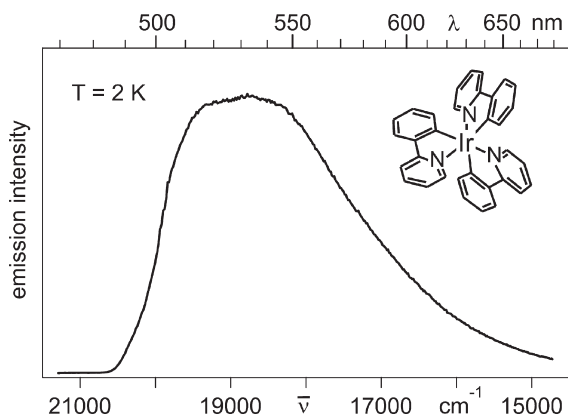


Fig. 1.17 Emission spectrum of Ir(ppy)₃ in tetrahydrofuran ($\approx 10^{-5}$ mol L⁻¹) at $T = 2$ K, $\lambda_{\text{exc}} = 363.8$ nm (compare Ref. [115]).

investigating the compound at low temperature. This may be due to the fact that, until now, a suitable host material for Ir(ppy)₃ has not been found.

Figure 1.17 shows an emission spectrum of Ir(ppy)₃ doped into tetrahydrofuran (THF). Although the temperature is as low as $T = 2$ K, the spectrum is still very broad (compare also Section 1.11). Therefore, indirect methods must be applied to gain sufficient information for a successful characterization of the emitting states. A determination of the ZFS values and the *individual* decay times of the T_1 substates is possible, if the *thermalized* emission decay times are available for a larger temperature range. This method will be explained by applying it to Ir(ppy)₃, although it has also been successfully used to characterize many other compounds [150, 153, 181–184].

The emission at $T = 1.2$ K stems from the lowest triplet substate I. From the relatively long decay time of $\tau_1 = 145$ μ s (Fig. 1.18), it follows that the corresponding transition to the ground state is largely forbidden. Therefore – and according to the spectral features as discussed for Ir(ppy)₃ in Ref. [115] – the radiative processes stemming from substate I have been assigned to be vibronically induced. From this behavior, it is indicated again that substate I represents a relatively pure triplet and that the transition to the ground state is symmetry forbidden. With temperature increase to $T = 4$ K, the emission decay time is drastically reduced, whereby the emission quantum yield remains high. This behavior shows clearly that higher-lying emitting states are thermally populated.

The temperature dependence of the emission decay time, as displayed in Fig. 1.18, allows the evaluation of an energy level diagram for the spectroscopically active states involved in the emission processes. Under assumption of a fast thermalization – as given for Ir(ppy)₃ – the occupation dynamics of excited states is governed by the expression (e.g., compare Ref. [181]):

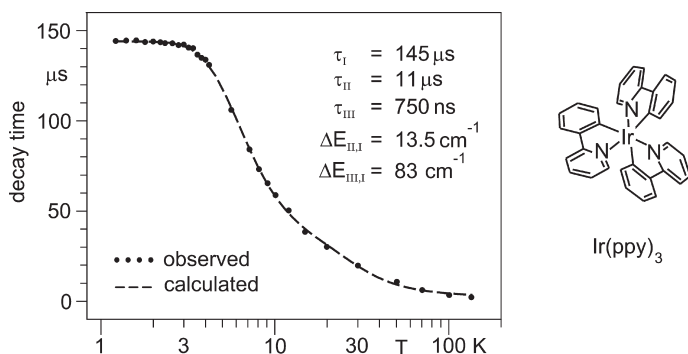


Fig. 1.18 Emission decay time of $\text{Ir}(\text{ppy})_3$ dissolved in tetrahydrofuran ($10^{-5} \text{ mol L}^{-1}$) versus temperature measured after excitation at 337.1 nm. The decay curves are monoexponential over the whole temperature range, at least after the experimental limit of

the equipment of $\approx 300 \text{ ns}$. From a fit of Eq. (8), one obtains the zero-field splitting energies and the decay times, which are also given. $\Delta E_{\text{III,I}}$ and $\Delta E_{\text{II,I}}$ are the energy differences between the respective triplet substates (compare Fig. 1.19).

$$\frac{dN}{dt} = -k_{\text{therm}}N = -\sum_i k(i)n_i \quad (7)$$

wherein n_i denotes the Boltzmann occupation number of state i , and $k(i)$ is the total rate constant for depopulation of state i . N is the total number of occupied excited states and $k_{\text{therm}} = 1/\tau_{\text{therm}}$ the rate constant for depopulation of the equilibrated (thermalized) system of excited states or the inverse of the measured decay time. The introduction of Boltzmann factors and the assumption of three emitting states with $i = \text{I, II, and III}$ lead to the expression (e.g., compare Refs. [181–185]):

$$k_{\text{therm}} = \frac{k(\text{I}) + k(\text{II})e^{-\Delta E_{\text{II,I}}/k_{\text{B}}T} + k(\text{III})e^{-\Delta E_{\text{III,I}}/k_{\text{B}}T}}{1 + e^{-\Delta E_{\text{II,I}}/k_{\text{B}}T} + e^{-\Delta E_{\text{III,I}}/k_{\text{B}}T}} \quad (8)$$

All constants and symbols have been explained above, and this equation can be applied for a fit to the measured lifetime data in dependence of the sample temperature, as shown in Fig. 1.18. The fitting procedure leads to $\Delta E_{\text{II,I}} = 13.5 \text{ cm}^{-1}$, $\Delta E_{\text{III,I}} = 83 \text{ cm}^{-1}$, $\tau_{\text{II}} = 11 \mu\text{s}$, $\tau_{\text{III}} = 750 \text{ ns}$. The fit was carried out with the fixed value of $\tau_{\text{I}} = 145 \mu\text{s}$, which is the emission decay time at 1.2 K, when only state I emits. The accuracy of the fit parameters is better than 10% if the model of just three emitting substates holds.²⁸⁾ These data are summarized in the energy level diagram shown in Fig. 1.19.

It should be noted that a fit based on a simplified Eq. (8) involving only two excited states cannot describe the observed temperature behavior. On the other hand, it cannot be ruled out definitely that more than three states are involved in

²⁸⁾ It should be noted that the value $\Delta E_{\text{III,I}}$ depends critically on the decay time data in the temperature range of $(30 \pm 10) \text{ K}$. Thus, the error of the $\Delta E_{\text{III,I}}$ value presumably exceeds 10% [186].

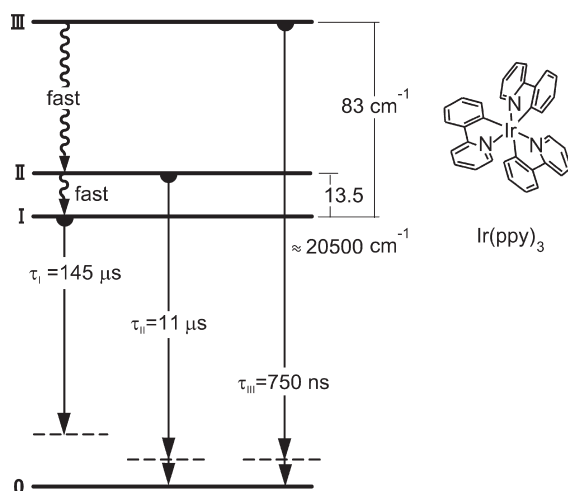


Fig. 1.19 Energy level diagram and decay times of Ir(ppy)₃ dissolved in tetrahydrofuran. The data are determined from broadband emission spectra by use of the temperature dependence of the emission decay time (compare Fig. 1.18 and Ref. [115]). The dashed lines represent vibrational energy levels.

the emission process, for example proximate higher-lying triplets. Further, the data obtained do not provide any reliable information about degeneracies or near degeneracies which might occur in the case that Ir(ppy)₃ maintains (nearly) the C₃ symmetry, as the fitting procedure does not allow the deduction of any group-theoretical assignment. Therefore, Eq. (8) is given for the simplest model of three non-degenerate substates.

Further, determination of the emission decay time for $T=300\text{ K}$ is also possible by use of Eq. (8). If the parameters obtained from the fitting procedure are used, a value of $\tau_{\text{therm}}=2.6\ \mu\text{s}$ is found, which corresponds well to the measured decay time at higher temperatures. The value measured for Ir(ppy)₃ in THF at 130 K is 2 μs , in degassed acetonitrile at 300 K it is 1.9 μs [187], and in degassed toluene 2 μs [188].

In conclusion, the emission decay behavior of Ir(ppy)₃ can be well modeled by three triplet substates with a total ZFS of $\Delta E(\text{ZFS})=83\ \text{cm}^{-1}$. This value is much larger than that found for Pt(thpy)₂ with $\Delta E(\text{ZFS})=16\ \text{cm}^{-1}$, or even for [Ru(bpy)₃]²⁺ ($\Delta E(\text{ZFS})=61\ \text{cm}^{-1}$), which is regarded as a typical ³MLCT emitter. Therefore, and especially according to Section 1.4 (Fig. 1.11), we assign the lowest triplet T₁ of Ir(ppy)₃ as being largely of MLCT parentage (compare also Ref. [189].) A corresponding interpretation results also from *ab-initio* calculations [116, 123, 124]. For completeness, the reader is referred to Section 1.3.3.3, where the magnitudes of singlet admixtures to the three triplet substates according to the calculations by Nozaki [124] are discussed. The two short-lived triplet substates II and III have singlet admixtures of the order of 1%, whilst substate I is largely a pure triplet, as predicted from the long emission decay time of $\tau_{\text{I}}=145\ \mu\text{s}$.

1.7

Phosphorescence Dynamics and Spin–Lattice Relaxation: Background and Case Study Applied to Pt(thpy)₂

1.7.1

Processes of Spin–Lattice Relaxation

The population dynamics of the different triplet substates, emission decay properties, and even emission spectra are, at low temperature, usually essentially determined by the times of relaxation between the substates. These times can be very long (e.g., the order of many μs), if the energy separations between the substates are of the order of several wavenumbers. This behavior is connected to the property that the excess energy of a higher-lying triplet substate is not easily transferred to the lattice due to the small density of states of lattice vibrations (phonons) in this energy range, and due to the requirement of spin-flips for transitions between the substates. This type of relaxation is known as spin–lattice relaxation (SLR). Although, it has been known for decades that such slow processes are of significant importance for the emission behavior (e.g., see Refs. [98, 190–198]), the almost general importance for organometallic compounds also has not yet been fully recognized. Within the literature, different mechanisms have been discussed which may induce a spin-flip due to an interaction of phonons with the triplet substates of a molecule. The phonon modes can cause fluctuations of molecular properties, such as intramolecular distances, and thus can modulate electronic charge distributions, SOC, and mixing coefficients between different states. It is beyond the scope of this chapter, however, to discuss these mechanisms in greater detail (see Refs. [98, 190–200]).

Usually, SLR is described by considering three different processes, namely the *direct*, the *Orbach*, and the *Raman process* [98, 193–198]. These are illustrated in Fig. 1.20 (compare also Refs. [70, 74, 182, 185, 201]). The three electronic states **I**, **II**, and **III** represent, for example, the three triplet substates of an organometallic compound with energy separations of several cm^{-1} . It is assumed that one of the higher-lying states – for example state **II** – is populated by a relaxation from a still higher-lying state or by a resonant excitation of just this electronic state.

These three SLR processes and the temperature dependences of the corresponding rates are briefly introduced in the following sections.

1.7.1.1 The Direct Process

A relaxation from state **II** to state **I** may occur by emission of one phonon with the energy $\Delta E_{\text{II,I}}$, which is transmitted to the lattice (Fig. 1.20a). This process is called the *direct process* of SLR. The corresponding rate $k_{\text{II,I}}^{\text{SLR}}$ (direct) dominates the rates of other processes of SLR at low temperature T . For higher temperatures, the absorption of a phonon can also take place, and thus represents a back process from state **I** to state **II**. Both up and down processes give rise to the *direct process*. For the net rate, one obtains (e.g., compare Refs. [74, 98, 182, 193, 195, 201]):

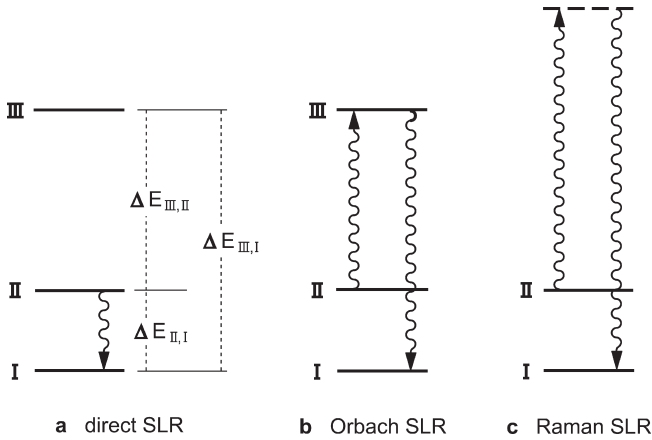


Fig. 1.20 Schematic diagram to illustrate the different processes of spin–lattice relaxation (SLR). The states I, II, and III represent, for example, triplet substates of organo-transition metal compounds. The energy separations are given by the zero-field splittings (ZFS) (compare also Table 1.1).

$$k_{II,I}^{\text{SLR}}(\text{direct}) = \frac{3}{2\pi\hbar^4\rho v^5} \cdot |\langle \text{II} | V | \text{I} \rangle|^2 \cdot (\Delta E_{II,I})^3 \cdot \coth(\Delta E_{II,I}/2k_B T) \quad (9)$$

where ρ is the mass density of the matrix material, v the (average) velocity of sound in the matrix, and k_B the Boltzmann constant. V represents the perturbation caused by lattice modes (phonons) which couple the electronic states I and II. The *direct process* exhibits only a weak temperature dependence.

1.7.1.2 The Orbach Process

At higher temperatures, the relaxation may also proceed indirectly by the two-phonon *Orbach process* (Fig. 1.20b). Schematically, in this process one phonon of the energy $\Delta E_{III,II}$ is absorbed, while a second phonon of the energy $\Delta E_{II,I}$ is emitted. The inverse process can also occur. The rate of this process has been determined only recently also for a general pattern of ZFS states, which are often found for the compounds being of interest here. The corresponding approximation, representing an *extended Orbach process*, was derived in Refs. [182, 201]. A slightly simplified expression is given by the following equation [182, 185]:

$$k_{II,I}^{\text{SLR}}(\text{Orbach}) = \frac{C_{III,II} C_{III,I} (e^{\Delta E_{III,II}/k_B T} + e^{\Delta E_{II,I}/k_B T})}{C_{III,I} e^{\Delta E_{II,I}/k_B T} (e^{\Delta E_{III,II}/k_B T} - 1) + C_{III,II} e^{\Delta E_{III,II}/k_B T} (e^{\Delta E_{II,I}/k_B T} - 1)} \quad (10)$$

with the abbreviations

$$C_{III,I} = \frac{3}{2\pi\hbar^4\rho v^5} \cdot |\langle \text{III} | V | \text{I} \rangle|^2 \cdot (\Delta E_{III,I})^3$$

$$C_{III,II} = \frac{3}{2\pi\hbar^4\rho v^5} \cdot |\langle \text{III} | V | \text{II} \rangle|^2 \cdot (\Delta E_{III,II})^3 \quad (11)$$

The used parameters and matrix elements correspond directly to the definitions given above. The energy separations are specified in Fig. 1.20. From the more general equation [Eq. (10)], the original *Orbach expression* can be obtained. It is derived under the assumption of specific energy differences, namely of $\Delta E_{\text{III,I}} \approx \Delta E_{\text{III,II}} = \Delta E$ (compare Refs. [98, 194, 195, 198]):

$$k_{\text{II,I}}^{\text{SLR}}(\text{Orbach}) \approx \frac{2C_{\text{III,II}}C_{\text{III,I}}}{(C_{\text{III,I}} + C_{\text{III,II}})} \cdot \frac{1}{e^{\Delta E/k_{\text{B}}T} - 1} \quad (12)$$

This expression can further be simplified for $\exp(\Delta E/k_{\text{B}}T) \gg 1$ or for $\Delta E \gg k_{\text{B}}T$. Thus, one obtains the famous and simple approximation for the *Orbach process*

$$k_{\text{II,I}}^{\text{SLR}}(\text{Orbach}) \approx \text{const} \cdot (\Delta E)^3 \cdot e^{-\Delta E/k_{\text{B}}T} \quad (13)$$

This approximation has – together with the expression for the *direct process* according to Eq. (9) – been used successfully to fit the temperature dependence of the SLR rate of $[\text{Ru}(\text{bpy})_3]^{2+}$ doped into $[\text{Zn}(\text{bpy})_3](\text{ClO}_4)_2$ up to $T \approx 10$ K [74]. However, application of the approximations given in Eqs. (12) and (13) to the experimental data obtained for $\text{Pt}(\text{thpy})_2$ does not lead to a successful fit, as the condition described above – assuming $\Delta E_{\text{III,I}} \approx \Delta E_{\text{III,II}}$ does not hold for the specific ZFS pattern of this complex (see Fig. 1.16.). In contrast, a good fit is obtained, if Eq. (10) is used (see Ref. [201] and below). For completeness, it should be noted that the rate according to the *Orbach process* vanishes for $T \rightarrow 0$ K, and also for $\Delta E \rightarrow 0 \text{ cm}^{-1}$.

1.7.1.3 The Raman Process

A relaxation between the states **II** and **I** can also proceed by a two-phonon Raman scattering process, according to Fig. 1.20c. The temperature dependence of the corresponding rate is usually approximated by

$$k_{\text{II,I}}^{\text{SLR}}(\text{Raman}) = R \cdot T^n \quad (14)$$

with a constant R and with n equal to 5 or 7 (for non-Kramers compounds [196]). For the organo-transition metal complexes hitherto studied, the T^5 dependence fits to the experimental observations much better than the T^7 dependence. [185, 202]. It should be noted that the *Raman process* is usually less effective than the *Orbach process*, if a higher-lying electronic state is present, such as state **III** in Fig. 1.20b. If not, however, the *Raman process* becomes important. For example, for $\text{Pt}(\text{thpy})(\text{CO})(\text{Cl})$ with an energy level diagram similar to that shown in Fig. 1.20c, it has been found that the *Raman process* with a T^5 dependence must be taken into account for $T \gtrsim 5$ K. Its rate exceeds the one of the *direct process* above $T = 9$ K [185].

1.7.2

Population and Decay Dynamics of the Triplet Substates of $\text{Pt}(\text{thpy})_2$

The emission rise and decay properties of the three triplet substates have been well studied for $\text{Pt}(\text{thpy})_2$. Therefore, this complex represents a good example to

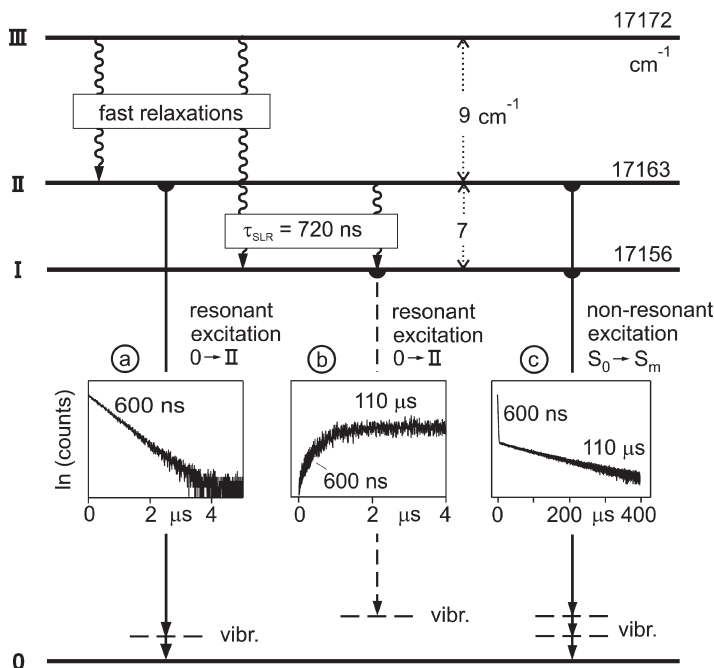


Fig. 1.21 Triplet substates of $\text{Pt}(\text{thpy})_2$ and dynamic processes of spin–lattice relaxation at $T=1.3$ K. $\text{Pt}(\text{thpy})_2$ is dissolved in *n*-octane at a concentration of $\approx 10^{-5}$ mol L $^{-1}$. (a) Resonant excitation at the electronic origin II (0–0) (17163 cm^{-1}) and detection of the emission of state II at the 653 cm^{-1} vibrational satellite at 16510 cm^{-1} . (b) Same excitation as in (a), but detection of the emission of state I at the 531 cm^{-1} satellite at 16625 cm^{-1} . (c) Excitation into a higher-lying singlet (e.g., $\lambda_{\text{exc}}=337.1$ nm), detection at 16444 cm^{-1} with a bandwidth of ≈ 5 cm^{-1} . Thus, the emissions from substate I on the 713 cm^{-1} vibrational satellite and from substate II on the 718 cm^{-1} satellite, are monitored (compare Section 1.9 and Refs. [182, 185]).

illustrate the importance of SLR between the triplet substates of organo-transition metal compounds. Figure 1.21 reproduces the energy level diagram of $\text{Pt}(\text{thpy})_2$ (as already presented in Fig. 1.16), and summarizes the dynamical emission properties observed at $T=1.3$ K. Interestingly, at low temperature they depend on the excitation as well as on the detection energy. Such behavior is rather typical for organo-transition metal compounds if they exhibit similar splitting patterns and magnitudes of $\Delta E(\text{ZFS})$. The properties will be explained by use of the insets shown in Fig. 1.21 [182, 185].

- After an excitation with a laser pulse of triplet substate III at 17172 cm^{-1} , one finds a fast SLR to the two lower-lying substates II and I. At $T=1.3$ K, the *Orbach* and the *Raman processes* are negligible, and the SLR is governed by the *direct process*. Due to the relatively large energy separation of $\Delta E_{\text{III,I}}=16$ cm^{-1} and the $(\Delta E_{\text{III,I}})^3$ dependence [Eq. (9)], the SLR

rate according to this process will be large, as depicted in Fig. 1.21.

- The emission decay behavior of substate **II** is of specific interest. After a pulsed and resonant excitation of the $\mathbf{0} \rightarrow \mathbf{II}$ transition at $17\,163\text{ cm}^{-1}$, a strictly monoexponential decay with a decay constant of $600 \pm 10\text{ ns}$ is observed (for more than five lifetimes), if the emission is detected selectively on a vibrational satellite that corresponds to the emission of substate **II** (Fig. 1.21a). For example, the 653 cm^{-1} satellite is well suited (compare Fig. 1.32, below). The corresponding decay rate is $k_{\text{exp}} = 1/600\text{ ns} = 1.67 \times 10^6\text{ s}^{-1}$. This decay is mainly determined by the *direct process* of SLR from state **II** to state **I** (for a slight correction see Eq. (15) below). Again at $T = 1.3\text{ K}$, the other two SLR processes are inefficient. Later in this section, we will discuss the temperature dependence of the rate of SLR between these two substates **II** and **I**. An increasing importance of the *Orbach* and the *Raman processes* at higher temperatures will be demonstrated below.
- After substate **II** is excited selectively, substate **I** will be populated indirectly by the SLR process. Indeed, a corresponding rise is observed (Fig. 1.21b). For this experiment, the excitation is maintained as before, but the emission is detected on a vibrational satellite which belongs selectively to the state **I** emission. The 531 cm^{-1} satellite represents such a specific satellite (compare Fig. 1.31, below). After the emission rise, the population of substate **I** decays with the usual emission decay time of substate **I** of $\tau_1 = 110\text{ }\mu\text{s}$ [185].
- It is also instructive to discuss the decay behavior, in case $\text{Pt}(\text{thpy})_2$ is excited non-selectively by exciting a singlet ($\mathbf{S}_0 \rightarrow \mathbf{S}_m$), for example, and by applying a non-selective detection. These conditions correspond to a usual experimental situation. In this case, the two decay components of 600 ns and $110\text{ }\mu\text{s}$ are found, since by the relaxation both substates **I** and **II** are initially populated and both states exhibit their individual relaxation and emission decay behavior (compare Fig. 1.21c and Refs. [182, 185]).

The experimentally determined decay time of the higher-lying triplet substate **II** of $\tau_{\text{exp}} = 600\text{ ns}$ ($= 1/k_{\text{exp}}$) does not directly represent the SLR time, since the decay of substate **II** is given by two processes – that is, by the usual decay from this substate **II** to the ground state $\mathbf{0}$, $k_{\text{II},0} = 1/\tau_{\text{II}}$, and by the SLR rate from substate **II** to substate **I**, $k_{\text{II},\text{I}}^{\text{SLR}}$. Thus, the SLR rate is obtained by [182, 185]:

$$k_{\text{II},\text{I}}^{\text{SLR}} = k_{\text{exp}} - k_{\text{II},0} \quad (15)$$

Although the emission decay time $\tau_{II} = 1/k_{II,0}$ of substate II cannot be measured directly, it can be determined from the temperature dependence of the emission decay time of the thermally equilibrated system of the triplet substates. This procedure, as described in Section 1.6, has been carried out for Pt(thpy)₂ in Ref. [182], where $k_{II,0} = 2.78 \times 10^5 \text{ s}^{-1}$ ($\tau_{II} = 3.6 \mu\text{s}$) is obtained. (Compare Fig. 1.16.) By use of Eq. (15) with $k_{\text{exp}} = 1.67 \times 10^6 \text{ s}^{-1}$ ($\tau_{\text{exp}} = 600 \text{ ns}$), the values $k_{II,I}^{\text{SLR}} = 1.39 \times 10^6 \text{ s}^{-1}$ or $\tau_{\text{SLR}} = 720 \text{ ns}$ are found (compare Fig. 1.21).

The SLR observed at $T = 1.3 \text{ K}$ is given by the *direct process*. However, with temperature increase, the other processes also become important and will dominate at higher temperature; this behavior is illustrated in Fig. 1.22. The SLR rate is determined from the measured decay times $\tau_{\text{exp}}(T) = 1/k_{\text{exp}}(T)$, according to the inset in Fig. 1.22, and by applying the correction expressed by Eq. (15). The resulting data of $k_{II,I}^{\text{SLR}}(T)$ can be fitted well (Fig. 1.22), when the three processes, illustrated in Fig. 1.20, are taken into account. Thus, application of the expressions for the *direct process* $k_{II,I}^{\text{SLR}}(\text{direct})$ [Eq. (9)], the *extended Orbach process* $k_{II,I}^{\text{SLR}}(\text{Orbach})$ [Eq. (10)], and the *Raman process* $k_{II,I}^{\text{SLR}}(\text{Raman})$ [Eq. (14)], leads to

$$k_{II,I}^{\text{SLR}} = k_{II,I}^{\text{SLR}}(\text{direct}) + k_{II,I}^{\text{SLR}}(\text{Orbach}) + k_{II,I}^{\text{SLR}}(\text{Raman}) \quad (16)$$

This expression describes the temperature dependence of the SLR rate from state II to state I of Pt(thpy)₂, and is used for the fitting procedure (compare Refs. [182, 185, 201]). Equation (16) contains six parameters after insertion of Eqs. (9), (10), and (14). However, these are reduced to only two free fit parameters, as all energy separations are known from highly resolved spectra

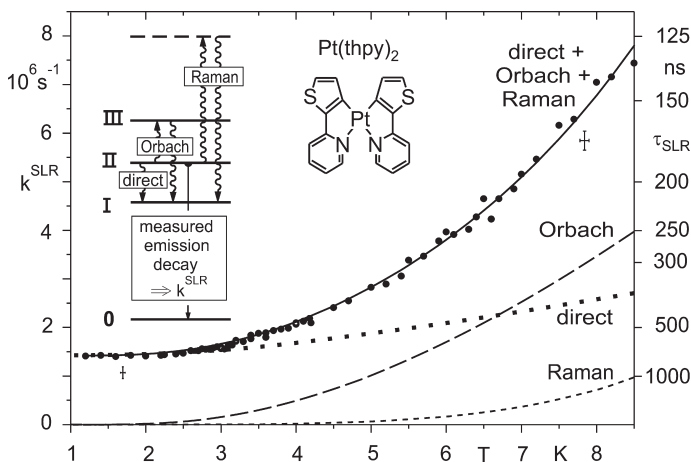


Fig. 1.22 Temperature dependence of the rate $k_{II,I}^{\text{SLR}}$ ($= k^{\text{SLR}}$ as displayed in the figure) and time τ_{SLR} of spin-lattice relaxation of state II of Pt(thpy)₂ dissolved in *n*-octane. The experimental data (points) result from the emission decay times of state II, corrected according to Eq. (15). The solid line

represents a fit according to Eq. (16), while the broken and dotted lines give the contributions of the respective processes. The inset shows the triplet substates and depicts schematically the three different processes of spin-lattice relaxation (compare Ref. [185]).

(Fig. 1.21), the ratio $C_{\text{III,I}}/C_{\text{III,II}}$ is determined as ≈ 1.2 [182] from time-resolved excitation spectra, $C_{\text{II,I}}$ is equal to the low-temperature limit of the SLR with $k_{\text{II,I}}^{\text{SLR}}(\text{direct}, T = 1.3\text{K}) = 1/\tau_{\text{SLR}} = 1.39 \times 10^6 \text{ s}^{-1}$ (see above), and the exponent of Eq. (14) can be set to $n=5$. Thus, the fitting procedure leads to the two unknown parameters and produces the solid line in Fig. 1.22 (for further details, see Ref. [182]).

The results obtained are also used to illustrate graphically the relative magnitudes of the three different processes that give the total rate of SLR $k_{\text{II,I}}^{\text{SLR}}(T)$. For the temperature range between $1.3\text{K} \leq T \leq 3\text{K}$, the total rate $k_{\text{II,I}}^{\text{SLR}}$ is nearly exclusively determined by the *direct process*. Above $T \approx 3\text{K}$ and above $\approx 6\text{K}$, the *Orbach* and the T^5 *Raman process*, respectively, become important. Although, the *Raman process* is less significant than the two other processes, its inclusion with $R = (10 \pm 3) \text{ K}^{-5} \text{ s}^{-1}$ improves the fit.

In conclusion, the times of relaxation between different triplet substates can be relatively long, such as 720 ns for $\text{Pt}(\text{thpy})_2$ at $T = 1.3\text{K}$. As a consequence, the emission of higher-lying states cannot be frozen out. Therefore, the usually monitored time-integrated, low-temperature emission spectra often represent superimposed spectra which stem from different excited states. (Compare also the results discussed for $\text{Ir}(\text{btp})_2(\text{acac})$, Fig. 1.34, below.) Moreover, in this situation, the emission decay behavior depends on the excitation and the detection energy. At very low temperature, the *direct process* of SLR dominates for compounds with ZFSs of the triplet state of a few cm^{-1} , while with temperature increase the SLR becomes distinctly faster due to growing in of the *Orbach* and/or the *Raman processes*. The specific temperature dependence of the SLR rate and the importance of an individual process is essentially determined by the magnitude and pattern of ZFS of the lowest triplet. In particular, when a real electronic state (such as substate **III**) is present (see Fig. 1.20b), the *Orbach process* will dominate the *Raman process*. On the other hand, the latter process will govern the temperature dependence of SLR, when the third state is absent [182, 185]. For completeness, it should be noted that the processes of SLR are very fast at ambient temperature, and a thermalized decay time of the three substates is observed.

The pattern and magnitude of ZFS is chemically tunable, as is depicted schematically in Fig. 1.11. Thus, the effective SLR can also be varied chemically. Several emitter/matrix combinations, for which highly resolved spectra as well as SLR properties have been investigated, are summarized in Table 1.1. The τ_{SLR} values given in the table refer to the low temperature ($T = 1.3\text{K}$) at which the *Orbach* and *Raman processes* can be neglected. Only the *direct process* of SLR is important. The data in the table show that the effects of SLR are quite general, with the SLR times mostly in the range of several 100 ns to some μs , when the energy separation between the two involved states is of the order of 10 cm^{-1} , or less. The value found for site **H** of $\text{Ir}(\text{btp})_2(\text{acac})$ in CH_2Cl_2 with $\tau_{\text{SLR}} = 22\ \mu\text{s}$ is, at first sight, remarkably long. However, the energy separation of $\Delta E_{\text{II,I}} = 2.9\text{ cm}^{-1}$ is, compared to the one of $\text{Pt}(\text{thpy})_2$ in *n*-octane, relatively small. Thus, if one takes the $(\Delta E_{\text{II,I}})^3$ dependence of the corresponding rate $k_{\text{II,I}}^{\text{SLR}}$ into account [Eq. (9)] and calculates formally the expected time of τ_{SLR} for an assumed $\Delta E_{\text{II,I}}$ value of 7 cm^{-1} , a hypothetical SLR time

Table 1.1 Photophysical data of several organo-transition metal compounds arranged according to an increasing spin-lattice relaxation time due to the direct process of SLR.

Compound, Matrix	Lowest triplet substate I ¹⁾ (cm ⁻¹)	ZFS		Decay times		Remarks, References
		$\Delta E_{II,I}$ ¹⁾ (cm ⁻¹)	$\Delta E_{III,I}$ ¹⁾ (cm ⁻¹)	τ_i ²⁾ (μ s)	τ_{SLR} (II \rightarrow I) ^{1),2)} (μ s)	
[Ru(bpy) ₃] ²⁺ in [Zn(bpy) ₃](ClO ₄) ₂	17 684	8.7	61	230	0.22	74
Pt(ppy) ₂ in <i>n</i> -octane	19 571	6.5	32	70	0.39	70, 148
Pt(thpy) ₂ in <i>n</i> -octane	17 156	7	16	110	0.72	182, 185
Pt(thpy)(CO)(Cl) in <i>n</i> -octane	18 012.5	0.055	3.8	120	3	182, 141, SLR between the substates III and I/II
Pt(4,6-dFppy) ₂ in <i>n</i> -octane	20 629	4	31	55	3.7	204
Ir(btp) ₂ (acac) in CH ₂ Cl ₂ (site H)	16 268	2.9	25	150	22	147, 203

1) Determined from highly resolved spectra.

2) Measured at T = 1.3 K.

of $\approx 1.5 \mu$ s would be obtained. This value is only by a factor of about two longer than that found for Pt(thpy)₂. Such a deviation might easily result from different values of the prefactors, the velocity of sound, and/or the matrix element, in Eq. (9) (compare also Section 1.10.3 and Ref. [203]).

Finally, an interesting implication of the occurrence of a slow SLR should be noted which opens the possibility of investigating the emission properties of the higher-lying substate II also at T = 1.3 K, as the corresponding emission cannot be frozen out. Therefore, access is obtained to the highly informative low-temperature emission spectrum of this higher lying state. This favorable situation is applied in Section 1.9.2.3 to study the highly resolved vibrational satellite structure of the emission of substate II of Pt(thpy)₂.

1.8

The Triplet State Under Application of High Magnetic Fields: Properties of Ir(btp)₂(acac)

The triplet substates and the related transitions of a specific organometallic compound exhibit distinct differences with respect to photophysical properties, such as radiative rates, energy separations, SLR dynamics, vibronic coupling (see below, Section 1.9), and emission and excitation spectra. Many studies have shown that these properties can distinctly be altered under the application of large external magnetic fields (compare Fig. 1.15 and Refs. [74, 85, 115, 147, 163, 177, 185, 202,

204–215]). In this section, we will illustrate how the application of magnetic fields alters the properties of the three triplet substates and of the corresponding electronic 0-0 transitions. For this, we have chosen Ir(btp)₂(acac) [147, 203], as it represents a very efficient red-emitting OLED material. Consequently, many photophysical and OLED related investigations were carried out with this complex [215–236], although the influence of magnetic field application has (apart from Ref. [147]) not yet been discussed.

Ir(btp)₂(acac) was first synthesized and studied spectroscopically by Thompson et al. [227]. The emitter exhibits a high photoluminescence quantum yield of $\phi_{\text{PL}}=21\%$ in solution, and a decay time of 5.8 μs . [227] In a 4,4'-bis(carbazol-9-yl)biphenyl (CBP) film, a ϕ_{PL} value as high as 50% has been reported [216].

Figure 1.23 shows emission spectra of Ir(btp)₂(acac) dissolved in CH₂Cl₂, and the spectral changes upon cooling. The host material crystallizes as a Shpol'skii-like matrix, and therefore, at $T=4.2\text{ K}$ line spectra are observable. The lines represent electronic 0-0 transitions of a large number of different sites, which are characterized by dissimilar interactions of the dopants with their respective environments or matrix cages (compare Section 1.10). It will be shown below that these electronic transitions occur between the respective triplet substate **II** and the elec-

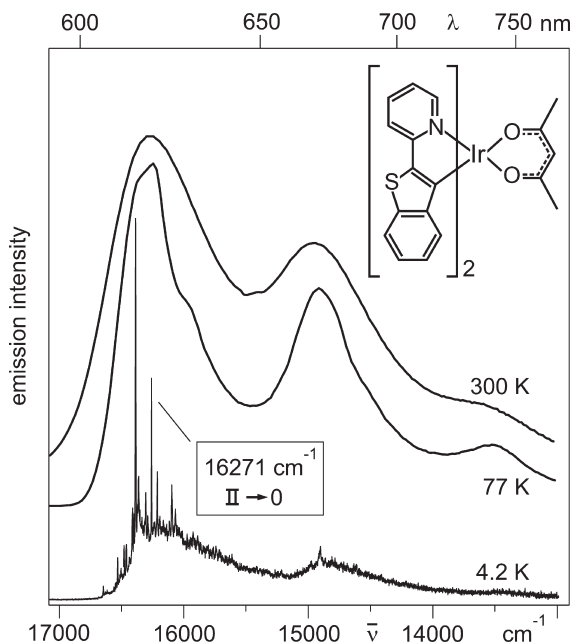


Fig. 1.23 Emission spectra of Ir(btp)₂(acac) in CH₂Cl₂ (ca. $\approx 10^{-5}\text{ mol L}^{-1}$) at different temperatures. The emission structure at $T=4.2\text{ K}$ consists mainly of 0-0 lines (triplet substate **II** to the electronic ground state **0**) of a large number of discrete sites and a broad

inhomogeneous background. In this section, properties of the site at 16271 cm^{-1} (specified as site **H** in Section 1.10) are investigated in detail. Other sites are discussed in Section 1.10.

tronic ground state S_0 (0). In the 4.2 K spectrum of Fig. 1.23, the $II \leftrightarrow 0$ transition at 16271 cm^{-1} of one specific site is marked (in Section 1.10 and Ref. [147] this site is specified as site **H**). This site can be selectively excited with a tunable laser and studied individually.

Within the scope of this section, we want to focus on the electronic transitions between the T_1 substates and the ground state S_0 . The emission line spectra of the corresponding energy range are reproduced in Fig. 1.24. One can clearly identify the three 0-0 transitions from the three triplet substates **I**, **II**, and **III**, though only at different temperatures. At $T = 1.35 \text{ K}$, a very weak peak at 16268 cm^{-1} is detected, and is assigned to the purely electronic $I \rightarrow 0$ transition ($I(0-0)$). At $T = 4.2 \text{ K}$, the $II \rightarrow 0$ emission ($II(0-0)$) at 16271 cm^{-1} dominates and represents almost the only 0-0 emission line. With temperature increase, the triplet substate **III** is also populated according to a Boltzmann distribution, and the corresponding 0-0 transition ($III(0-0)$) at 16293 cm^{-1} grows in [147]. These data reveal that the substates **I** and **II** are separated by $(2.9 \pm 0.2) \text{ cm}^{-1}$, whereas the splitting of substates **I** and **III**, representing the total ZFS, amounts to $(25.0 \pm 0.5) \text{ cm}^{-1}$. From the intensity distribution and its temperature dependence, it can be concluded that the radiative transition from the lowest substate **I** to the ground state 0 is largely forbidden,

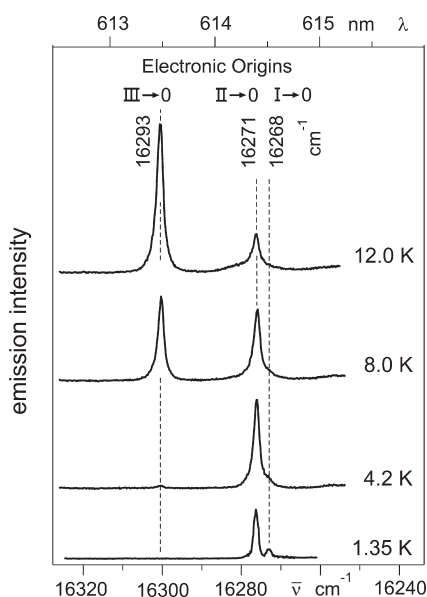


Fig. 1.24 Emission spectra at different temperatures of a selected site of $\text{Ir}(\text{btp})_2(\text{acac})$ dissolved in CH_2Cl_2 at a concentration of $\approx 10^{-5} \text{ mol L}^{-1}$. In Section 1.10, this site is specified as site **H**. Only the region of the electronic origins is reproduced. The specific site was excited at 16742 cm^{-1} (449 cm^{-1} vibrational satellite of the $0 \rightarrow III$

transition at 16293 cm^{-1}). The intensities of the different spectra are comparable. The spectrum at $T = 1.35 \text{ K}$ was measured with a higher resolution to obtain the energy difference of $\Delta E_{II-I} = 2.9 \text{ cm}^{-1}$ sufficiently accurate (compare Section 1.9.3 and Ref. [147]).

while the transitions from the two higher-lying substates **II** and **III** to the ground state are significantly more allowed. This can also be verified by decay time measurements, which reveal individual decay times of the T_1 substates of $\tau_I = 150 \mu\text{s}$, $\tau_{II} = 58 \mu\text{s}$, and $\tau_{III} = 2 \mu\text{s}$ [203]. The ZFS and decay time values are summarized in an energy level diagram given in Fig. 1.27 (see below). Mainly due to the magnitude of $\Delta E(\text{ZFS}) = 25 \text{ cm}^{-1}$, it can be concluded from Sections 1.3.3.3 and 1.4 that the triplet T_1 parent term has to be assigned as a ${}^3\text{LC}({}^3\pi\pi^*)$ term which, however, is significantly perturbed by an ${}^1{}^3\text{MLCT}$ admixture according to the coupling routes presented in Fig. 1.13a.

The forbiddenness of the transition from substate **I** to the singlet ground state **0** and the long emission decay time allows one to conclude that the lowest triplet substate **I** represents an almost pure triplet. A similar conclusion holds also for the lowest triplet substates of $\text{Ir}(\text{ppy})_3$, $\text{Pt}(\text{thpy})_2$, $[\text{Ru}(\text{bpy})_3]^{2+}$, $[\text{Os}(\text{bpy})_3]^{2+}$, and many other organo-transition metal compounds.

For completeness, it should be noted that the data given above refer only to the specific site investigated. Other sites exhibit different ZFSs, decay times of the substates, SLR times, etc. [147, 203]; these properties are discussed in Section 1.10.

The application of external magnetic fields significantly alters the splitting pattern and the intensity distribution of the three electronic origin lines. Figure 1.25 reproduces the corresponding trends for the field range of $B=0 \text{ T}$ to $B=8 \text{ T}$. Figure 1.25a shows the spectra measured at $T=8 \text{ K}$ for the complete spectral range of the three electronic origins. The relatively high temperature was chosen to provide sufficient population of the higher-lying substate **III**. Figure 1.25b reproduces only the region of the electronic origins $\text{I} \rightarrow \mathbf{0}$ and $\text{II} \rightarrow \mathbf{0}$. The spectra are monitored at $T=2.8 \text{ K}$ in order to obtain a better resolution; the population of substate **III** is frozen out at this temperature.

With an increase of the magnetic field strength, distinct Zeeman shifts of the transition energies are observed. Transition $\text{III}(0-0)$ is shifted to higher energy from 16293 cm^{-1} ($B=0 \text{ T}$) to $\approx 16295 \text{ cm}^{-1}$ ($B=8 \text{ T}$), while transition $\text{I}(0-0)$ is shifted to lower energy from 16268 cm^{-1} ($B=0 \text{ T}$) to $\approx 16265.5 \text{ cm}^{-1}$ ($B=8 \text{ T}$). The energy of $\text{II}(0-0)$ at 16271 cm^{-1} ($B=0 \text{ T}$) is only slightly increased by $\approx 0.5 \text{ cm}^{-1}$ up to $B=8 \text{ T}$. Figure 1.26 summarizes the magnetic field-induced energy shifts of the three electronic origins. Clearly, the Zeeman shifts are asymmetric. This is qualitatively understood, since the B -field induced mixings between the corresponding states depend on their energy separations at zero field (energy denominators) which are strongly asymmetric for $\text{Ir}(\text{btp})_2(\text{acac})$.

It should further be noted that the Zeeman shifts are usually different for molecules with different orientations relative to the magnetic field vector. This applies also to polycrystalline samples, as the molecules have different orientations in different micro-crystals. Therefore, the observed Zeeman pattern corresponds to an averaged orientational distribution of molecules.

A further important magnetic field-induced effect becomes apparent in the spectra of Fig. 1.25b. At $B=0 \text{ T}$, the transition from substate **I** to the ground state **0** is very weak, even at lowest temperature applied. With an increase of the field

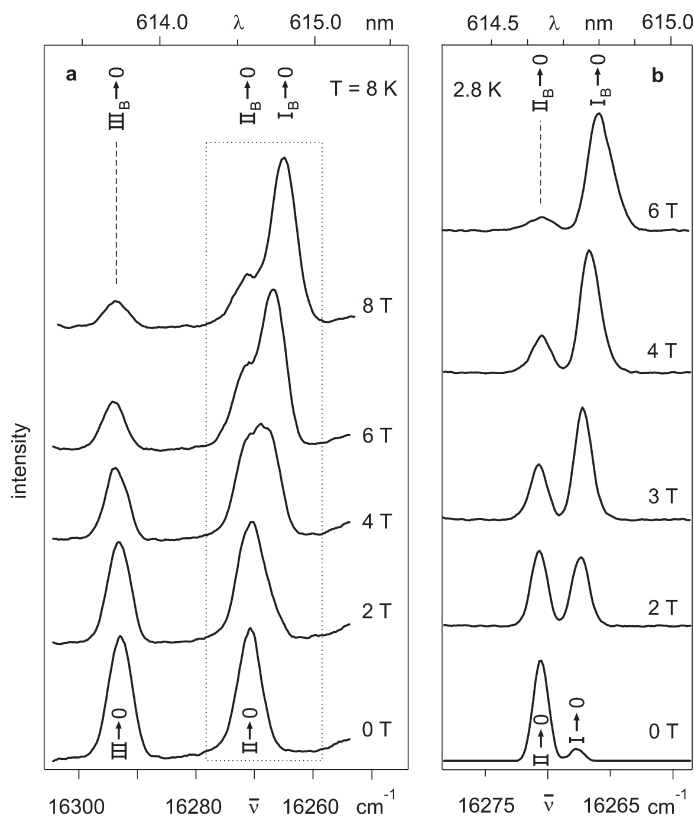


Fig. 1.25 Emission spectra of Ir(btp)₂(acac) in CH₂Cl₂ at $\approx 10^{-5}$ mol L⁻¹ in the energy range of the electronic 0-0 transitions at different magnetic fields. The spectra refer to the specific site which is investigated in this section (site H in Section 1.10). (a) The spectra were monitored at $T=8$ K to obtain

sufficient thermal population of substate III ($\bar{\nu}_{\text{exc}} = 26810$ cm⁻¹, non-selective excitation). (b) Selectively excited emission spectra for the energy range of the two lowest transitions I → 0 and II → 0, $T=2.8$ K, $\bar{\nu}_{\text{exc}} = 16293$ cm⁻¹ (0 → III). For further experimental details, see Ref. [147].

strength, this transition gains intensity. This effect becomes obvious already for $B < 1$ T (not shown). At $B=2$ T and $T=2.8$ K, the intensity stemming from the perturbed state I_B is almost equal to the intensity resulting from substate II_B. At $B=6$ T, for example, the intensity of transition I_B → 0 dominates clearly. For an explanation of this effect, three factors are important [147] (compare Fig. 1.27). First, the magnetic field-induced mixing of the wavefunction of substate I with the wavefunctions of the two higher states renders transition I_B → 0 more allowed. Second, due to the increased splitting between substates I and II under the magnetic field, the Boltzmann factor for population of state II (relative to state I) is significantly smaller. Third, SLR between the triplet substates becomes considerably faster with increasing field-induced energy separation between the

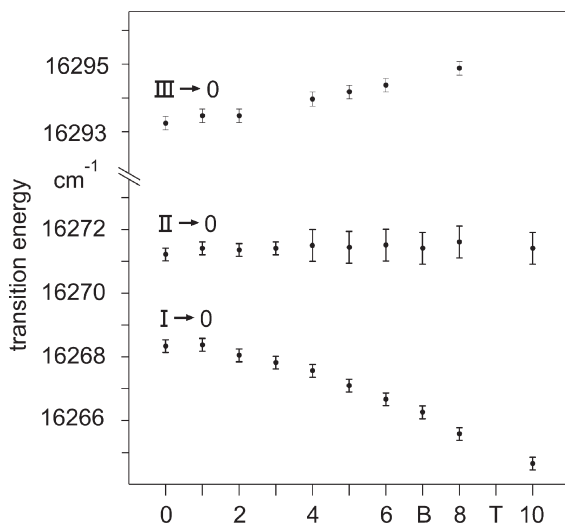


Fig. 1.26 Magnetic field-induced shifts of the T_1 substates I, II, and III of $\text{Ir}(\text{btp})_2(\text{acac})$ in CH_2Cl_2 . For experimental details, see Fig. 1.25 and Ref. [147].

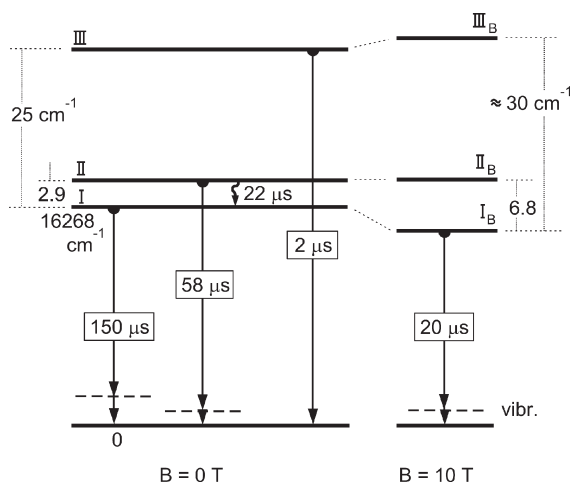


Fig. 1.27 Energy level diagram and photophysical data for the lowest triplet state T_1 of $\text{Ir}(\text{btp})_2(\text{acac})$ without and with an external magnetic field, respectively. The state is classified as ${}^3\text{LC}({}^3\pi\pi^*)$, which is significantly MLCT perturbed. The values given apply to the individual site under investigation in this section (specified as site

H in Ref. [147] and in Section 1.10). Other sites exhibit different spectroscopic properties (compare Section 1.10). The decay times of the T_1 substates and the spin–lattice relaxation time of $22\ \mu\text{s}$ (at $T=1.5\ \text{K}$) referring to zero magnetic field have been determined in Ref. [203], while the data at $B=10\ \text{T}$ ($T=1.7\ \text{K}$) are taken from Ref. [147].

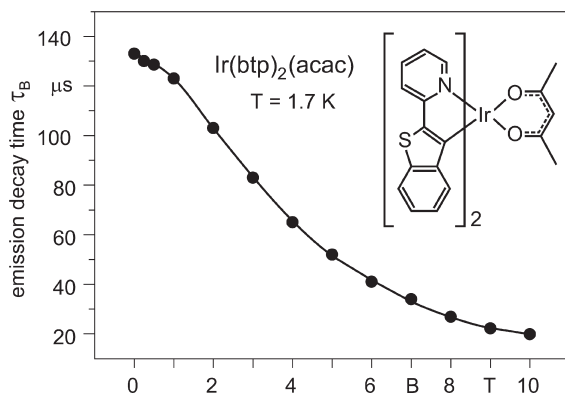


Fig. 1.28 Emission decay time of $\text{Ir}(\text{btp})_2(\text{acac})$ in CH_2Cl_2 for different magnetic flux densities B at $T = 1.7\text{ K}$ and under selective excitation of T_1 substate III. The decay is monoexponential over the whole range $0 \leq B \leq 10\text{ T}$; detection at the transition $\text{I}_B \rightarrow 0$.

corresponding states (compare Section 1.7).²⁹⁾ Accordingly, the Boltzmann distribution is established faster and thus the non-equilibrated fraction of the emission resulting from the higher-lying substate II_B is strongly reduced.

The increased allowedness of transition $\text{I}_B \rightarrow 0$ under the application of a magnetic field is also reflected in the emission decay time of the perturbed substate I_B . In particular, the almost pure and long-lived triplet substate **I** is expected to experience a distinct reduction of the emission decay time, when mixing with shorter-lived substates. Indeed, Fig. 1.28 shows that a drastic effect is observed. At $T = 1.7\text{ K}$, the decay time decreases from $\tau_1(B = 0\text{ T}) = 133\ \mu\text{s}$ to $\tau_1(B = 10\text{ T}) = 20\ \mu\text{s}$. The measurements were carried out with detection at the respective Zeeman shifted electronic origin (for $B = 0\text{ T}$ at $16\,268\text{ cm}^{-1}$ and for $B = 10\text{ T}$ at $16\,264.7\text{ cm}^{-1}$). Comparable measurements are often interpreted by the use of a simple first-order perturbation model which takes into account only mixing of the two lowest strongly interacting substates. Such a model is valid, if the energy separation between the substates **I** and **II** and the corresponding Zeeman shifts are small compared to the energy separation to substate **III**. This situation has been found, for example, for $\text{Ir}(\text{ppy})_3$ [115], $[\text{Ru}(\text{bpy})_3]^{2+}$ [205], and $[\text{Os}(\text{bpy})_3]$ [177, 206, 207]. For $\text{Ir}(\text{btp})_2(\text{acac})$, however, the data show clearly that this simple approach is not successful, as the decay time of I_B at $B = 10\text{ T}$ is, with $\tau_B = 20\ \mu\text{s}$, much shorter than the decay time of **II** at $B = 0\text{ T}$ ($\tau_{\text{II}} = 58\ \mu\text{s}$). Therefore, it must be concluded that the Zeeman mixing occurs between all three substates. In particular, the singlet component of substate **III** is responsible for the drastic shortening of the emission decay time of the lowest substate by the applied magnetic field.

²⁹⁾ Magnetic-field induced changes of SLR times have been investigated with $\text{Pt}(\text{thpy})_2$ [185]. These studies support the assignment given above.

In conclusion, the magnetic field experiments are very helpful for the characterization of an organo-transition metal complex, as they allow a more thorough interpretation of obtained data. For Ir(btp)₂(acac), the Zeeman behavior as described demonstrates that the three states involved represent indeed substates of one triplet parent term. An assignment of the three electronic origins to different sites can thus be excluded.

1.9

Vibrational Satellite Structures: Case Studies Applied to Pt(thpy)₂ and Ir(btp)₂(acac)

Usually, the emission from an electronic state takes place as purely electronic transition, for example, from a substate of the lowest triplet state T₁ to the electronic ground state S₀ with involvement of vibrational modes. At low temperature, these latter transitions occur at the low-energy side of the purely electronic transition. Generally, many different vibrations – having different energies – are active in the radiative processes from the emitting state of an organo-transition metal compound. Thus, an energetically widespread distribution of vibrational satellites is obtained. In suitable cases, the corresponding lines can be well resolved. With temperature increase, these vibrational satellites are smeared out and result in broad vibrational side bands (compare Section 1.11). The sidebands can comprise a substantial part of the total emission intensity, and this can have significant consequences, for example, on the color purity of an emitter applied in an OLED. In particular, a compound, of which the purely electronic 0-0 transition lies in the deep blue region of the visible spectrum, can still be a blue-green or turquoise emitter, if the vibrational satellite bands extend with significant intensity into the green region of the spectrum. This is due to the wavelength dependence of the human eye sensitivity, being highest for green. On the other hand, vibrational sidebands of red emitters frequently extend into the near-infrared region. This part is lost for the visual efficiency of an OLED.

Clearly, it is very important to study the mechanisms which lead to the occurrence of vibrational satellites, and to understand the corresponding spectral features. This will be addressed in the next sections, while broadening mechanisms including effects induced by temperature increase are discussed in Section 1.11.

1.9.1

Vibrational Satellites: Background

An electronic transition is usually accompanied by vibrational satellites which are found in absorption or excitation spectra, and also in emission spectra. Within this chapter, attention is focused on emission properties. The satellite lines result from different vibrational activities, namely from the well-known Franck–Condon activity and the less frequently discussed Herzberg–Teller (HT) activity. Here, we introduce details of both mechanisms.

1.9.1.1 Franck–Condon Activity

Vibrational satellites according to Franck–Condon activity can only occur, if the involved purely electronic transition between the ground state **0** and an electronically excited state **1** carries allowedness. In this situation, progressions can result. The occurrence of a progression is always connected with a geometry change between the two electronic states with respect to the vibrational coordinate of the progression forming mode. A useful measure for the extent of such a geometry variation is the Huang–Rhys parameter, S . In the following sections an introduction to these properties and to the spectroscopic implications is given (compare Refs. [98] (p. 200), and [70, 237, 238]).

Figure 1.29a depicts the harmonic potentials for a model system with only one vibrational coordinate Q in the electronic ground state **0** and the excited state **1**. It is assumed that the potentials are (nearly) equal, but are shifted by ΔQ with respect to each other – that is, the vibrational frequencies of both states are also (nearly) equal. Generally, the wavefunctions of electronic-vibrational states depend on both, the coordinates of the electrons and nuclei, and thus the wavefunctions are

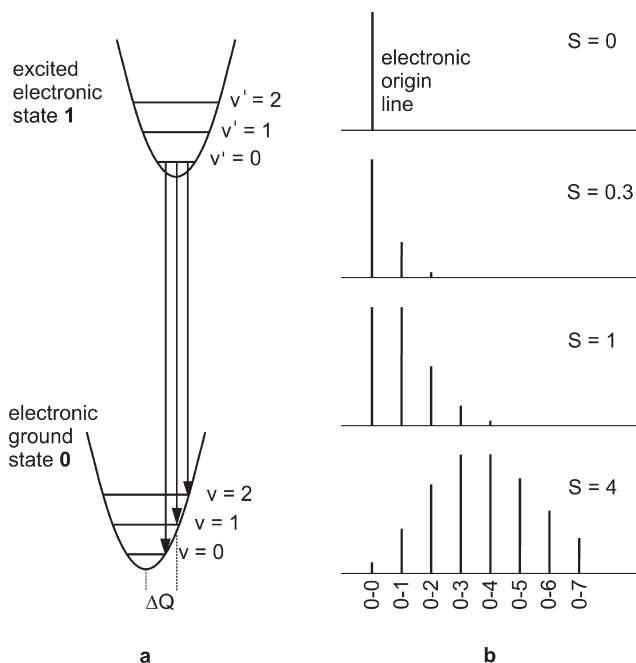


Fig. 1.29 Franck–Condon progressions. (a) The equilibrium positions of the potential surfaces of the excited state **1** and the ground state **0** are shifted by ΔQ . This leads to a progression in the emission spectrum, if the dipole moment of the transition between the states **1** and **0** is non-zero. The progression is characterized by vertical transitions that are

depicted for a low-temperature emission. (b) The intensity distribution of a progression of vibrational satellites depends on the Huang–Rhys parameter, S , which is proportional to $(\Delta Q)^2$ [see Eq. (21)]. The examples given in (b) are calculated according to Eq. (22). The peaks of highest intensity are normalized for the different diagrams.

very difficult to handle. However, taking into account that the electronic motion is much faster than the vibrational motion, one can factorize the vibrational and the electronic part of the wavefunction. This leads to the Born–Oppenheimer approximation with the

$$\begin{aligned} \text{ground state } \mathbf{0}: \psi_0(\mathbf{v}) &= \phi_0 \cdot \chi_0(\mathbf{v}) \\ \text{and the excited state } \mathbf{1}: \psi_1(\mathbf{v}') &= \phi_1 \cdot \chi_1(\mathbf{v}') \end{aligned} \quad (17)$$

wherein ϕ_0 and ϕ_1 are the electronic wavefunctions and $\chi_0(\mathbf{v})$ and $\chi_1(\mathbf{v}')$ are harmonic oscillator functions with vibrational quantum numbers \mathbf{v} and \mathbf{v}' for the electronic ground state $\mathbf{0}$ and the excited state $\mathbf{1}$, respectively. The harmonic oscillator functions are similar sets of wavefunctions, but they are defined with respect to different zero-positions of the variable Q .

The desire is to apply this model to study low-temperature emission spectra. The corresponding intensity distribution is proportional to the square of the electronic transition dipole moment involving the two states. When applying the approximation [Eq. (17)], the intensity of a transition from the zero-point vibrational level ($\mathbf{v}'=0$) of the excited state $\mathbf{1}$ to a level \mathbf{v} of the electronic ground state $\mathbf{0}$ can be expressed by (Fig. 1.29a):

$$I_{1,0}(\mathbf{v}'=0, \mathbf{v}) \sim |\langle \phi_1 | \mathbf{er} | \phi_0 \rangle|^2 \cdot |\langle \chi_1(\mathbf{v}'=0) | \chi_0(\mathbf{v}) \rangle|^2 \quad (18)$$

where \mathbf{er} is the usual electric dipole operator. The first term of the right-hand side of Eq. (18) represents the squared electronic dipole matrix element, and specifies the intensity of the purely electronic transition. The second term is the Franck–Condon factor, which is discussed in more detail below. This leads to the well-known Franck–Condon progression of vibrational satellites that progress in the spectrum by the energy $\bar{\nu}_Q$ of the vibrational mode under consideration.

The total emission intensity, I_{tot} , of all transitions with the different vibrational quantum numbers \mathbf{v} can be summed up, and one obtains

$$I_{\text{tot}} \sim |\langle \phi_1 | \mathbf{er} | \phi_0 \rangle|^2 \quad (19)$$

This result means that the total emission intensity – that is, the intensity of the electronic 0-0 transition and the complete Franck–Condon progression – depends only on the purely electronic transition dipole moment. Thus, the electronic allowedness represents the source of intensity which is distributed according to the Franck–Condon factor to the different vibrational satellites of the progression.

The Franck–Condon factor is given by the squared overlap integral of displaced harmonic oscillator functions.³⁰⁾ It can be related ([109], p. 113) to the so-called Huang–Rhys parameter, S , according to

30) The Franck–Condon factor can only be non-zero for totally symmetric modes, as the vibrational ground state $\chi_1(\mathbf{v}'=0)$ is totally symmetric.

$$|\langle \chi_1(v'=0) | \chi_0(v) \rangle|^2 = \frac{e^{-S} S^v}{v!} \quad (20)$$

This parameter S is directly connected with the shift ΔQ of the equilibrium positions of the involved electronic states (Fig. 1.29a). According to Ref. [109] (p. 112), one obtains

$$S = \frac{\pi c M \bar{v}_Q}{\hbar} (\Delta Q)^2 \quad (21)$$

wherein c is the velocity of light and M is the effective mass (=reduced mass) of the vibration Q . The value of M is usually not known, unless a normal coordinate analysis is available.

From Eq. (20), and by use of Eqs. (18) and (19), an expression can be derived, which is very useful for the characterization of geometry shifts of an excited state as compared to the ground state. For the intensity ratio of successive vibrational satellites of a Franck–Condon progression one finds, using the abbreviation $I_v = I_{1,0}$ ($v'=0, v$) for $v \neq 0$:

$$\frac{I_v}{I_{v-1}} = \frac{S}{v} \quad (22)$$

The intensity at the electronic origin (0-0 transition), I_0 , can be expressed by

$$I_0 = I_{\text{tot}} \cdot e^{-S} \quad (23)$$

From the above equations it is seen that for $S=0$ the total intensity is contained in the purely electronic origin line [Eq. (23)] and the displacement between the two electronic states **1** and **0** is zero [Eq. (21)]; that is, there is no geometry change connected with the electronic transition. With an increase of the displacement ΔQ (Fig. 1.29a), and thus an increase of the Huang–Rhys parameter S , the intensity of the electronic 0-0 line decreases and the vibrational satellites of the Franck–Condon progression gain intensity [Eq. (22)]. This behavior is illustrated in Fig. 1.29b for several different values of S . Thus, the satellites gain intensity only by borrowing it from the electronic origin line. If the electronic transition is forbidden, Franck–Condon satellites also do not occur. This situation is found, for example, for the **0** \leftrightarrow **I** transition of Pt(thpy)₂ (see Fig. 1.15b). The consequences of the vibrational satellite structure being connected with such a forbiddenness will be discussed in the next section, and also in Sections 1.9.2 and 1.9.3.

The S -value represents a characteristic parameter, in particular, when different compounds are compared [70]. Hence, it is possible to characterize changes of the binding situation that occur between excited electronic states and ground states for different types of electronic transitions. For example, for the **T**₁ \rightarrow **S**₀ transitions of a large number of organo-transition metal compounds, the maximum S -values

lie between 0.3 and 0.08 (compare Ref. [70] and Sections 1.9.2 and 1.9.3). From this it follows that the geometry changes between the ground and excited triplet state are small. Moreover, the S parameters are found to be significantly smaller for compounds with large (!) MLCT admixtures to the excited triplet states than for compounds with emitting ^3LC states. This behavior is ascribed to the enlarged spatial extensions of the electronic wavefunctions with an increasing MLCT admixture. In this situation, an electronic transition results in a smaller charge density change per ligand, and thus has less influence on the specific binding separation (small ΔQ values) [70, 165].

1.9.1.2 Herzberg–Teller Activity

In the preceding section, it was shown that Franck–Condon-induced satellites or progressions can only occur if the electronic transition carries allowedness, which may then be distributed to the vibrational satellites. However, in many cases, the electronic transition is largely forbidden. Nevertheless, a rich vibrational satellite structure is observed. This situation is frequently found for organo-transition metal compounds, for which the transition probability from the lowest triplet substate \mathbf{I} to the singlet ground state $\mathbf{0}$ is very small due to the almost pure triplet character of substate \mathbf{I} (compare Sections 1.5, 1.6, and 1.8). Clearly, a different process – the vibronic or Herzberg–Teller coupling – must be taken into account. In particular, this mechanism must provide singlet character to the triplet substate via spin–orbit coupling in order to induce radiative allowedness to the vibronic transition.

As the corresponding vibronic mechanisms are discussed comprehensively elsewhere in the literature [206, 239–243], only a brief discussion of a specific mechanism – the *spin-vibronic coupling* – is given here. It has been shown that such a mechanism can indeed provide the required transition probability [70, 206]. This coupling route is illustrated schematically in Fig. 1.30.

For purely organic compounds the mechanism of spin-vibronic coupling is usually neglected due to the small value of the SOC constant. In contrast, for compounds of the platinum metal group, this mechanism can be very important. Specifically, vibrations of the central-metal ion – that are connected with variations of electron density of d-character in the spatial region of the organic ligands – can induce significant changes in the effective SOC. Good candidates for such vibrations are metal–ligand vibrations. Such a coupling route is shown schematically in Fig. 1.30. \hat{H}_{SO} is the SOC Hamiltonian, \mathbf{I} represents the unperturbed lowest triplet substate, and \mathbf{S}_m is a higher lying singlet. The matrix element given in Fig. 1.30 signifies that the vibration with the (normal) coordinate Q modulates the SOC operator. This mechanism induces intensity to the specific vibrational satellite with the energy $\bar{\nu}_Q$ relative to the forbidden electronic origin, but it does not provide any intensity to the purely electronic 0-0 transition. Clearly, this vibronic mechanism can be effective for a large number of different vibrational modes Q . In this case, usually different intensity-providing higher-lying singlets \mathbf{S}_m are involved. The corresponding vibrational satellites are frequently called “false origins”.

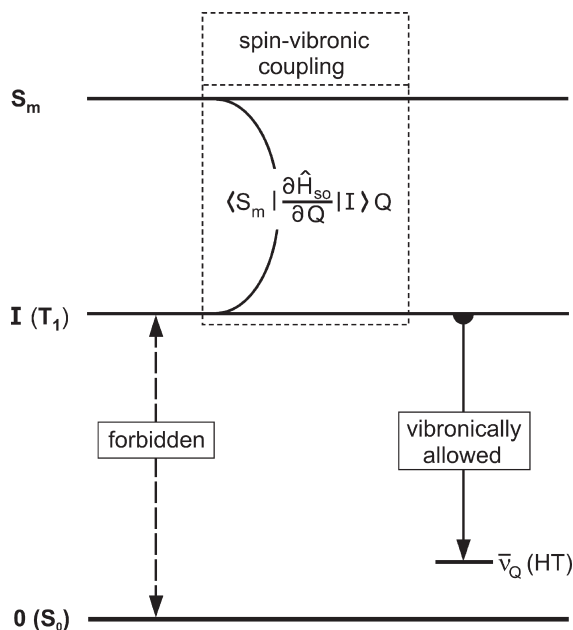


Fig. 1.30 Schematic illustration of the spin-vibronic coupling route (Herzberg–Teller coupling). This mechanism can become important, when the purely electronic $I \leftrightarrow 0$ transition is forbidden. The matrix element expresses schematically that a vibration, specified by a coordinate Q , changes the spin–orbit coupling (SOC) and thus induces

an admixture of a higher-lying singlet state S_m to the triplet substate I . This mechanism can provide intensity to a vibrational satellite, but not to the electronic 0-0 transition. Note that HT coupling usually occurs with many HT active modes to different higher-lying singlets. Hence, a rich vibrational satellite structure results. For further explanation, see the text.

In Sections 1.9.2.1 and 1.9.3, we will demonstrate that HT coupling is indeed important for the low-temperature emission of $\text{Pt}(\text{thpy})_2$ and $\text{Ir}(\text{btp})_2(\text{acac})$. The importance of the HT coupling has also been shown for many other organo-transition metal compounds [70, 71, 73, 74, 115, 163, 177, 206].

1.9.2

$\text{Pt}(\text{thpy})_2$ Emission: Temperature- and Time-Dependence of the Vibrational Satellite Structure

The vibrational satellite structures in the emission of $\text{Pt}(\text{thpy})_2$ display triplet substate properties in a characteristic manner. In particular, the emission from substate **I** features a completely different vibrational satellite structure than the emission from the substates **II** and **III**. This behavior will be illustrated by presenting spectra, which are measured at different temperatures and at different delay times after an exciting laser pulse, respectively.

1.9.2.1 Herzberg–Teller-Induced Emission from Substate I: The 1.3 K Spectrum

Figure 1.31 shows the emission spectrum of $\text{Pt}(\text{thpy})_2$ measured at $T=1.3\text{ K}$. The rich vibrational satellite structure seems to belong to the electronic 0-0 transition at 17163 cm^{-1} , which represents the $\text{II} \rightarrow 0$ transition (see Figs. 1.15 and 1.16). However, all vibrational energies as determined relative to this 0-0 transition do *not* match the vibrational energies available from IR measurements [70], and they cannot be related to vibrational energies found for $\text{Pd}(\text{thpy})_2$ [70, 163]. On the other hand, by setting the electronic origin for these satellites to the position of the transition $\text{I} \leftrightarrow 0$ at 17156 cm^{-1} which, however, does not carry any intensity, an excellent correspondence of the satellite energies to those of known vibrational modes is obtained. This procedure allows us to determine the position of a missing electronic origin line. Indeed, as discussed in Section 1.5.1, the $\text{I}(0-0)$ line can be observed directly under application of a magnetic field of $B \approx 1\text{ T}$ (see Fig. 1.15e). Interestingly, none of the satellites that is clearly identified in the 1.3 K time-integrated emission spectrum belongs to the electronic origin $\text{II}(0-0)$ at 17163 cm^{-1} , apart from a 15 cm^{-1} phonon satellite (Fig. 1.15b) and some spectral background.

The vibrational satellites observed in Fig. 1.31 correspond in most cases to fundamentals. Modes which occur up to $\approx 100\text{ cm}^{-1}$ relative to the electronic origin

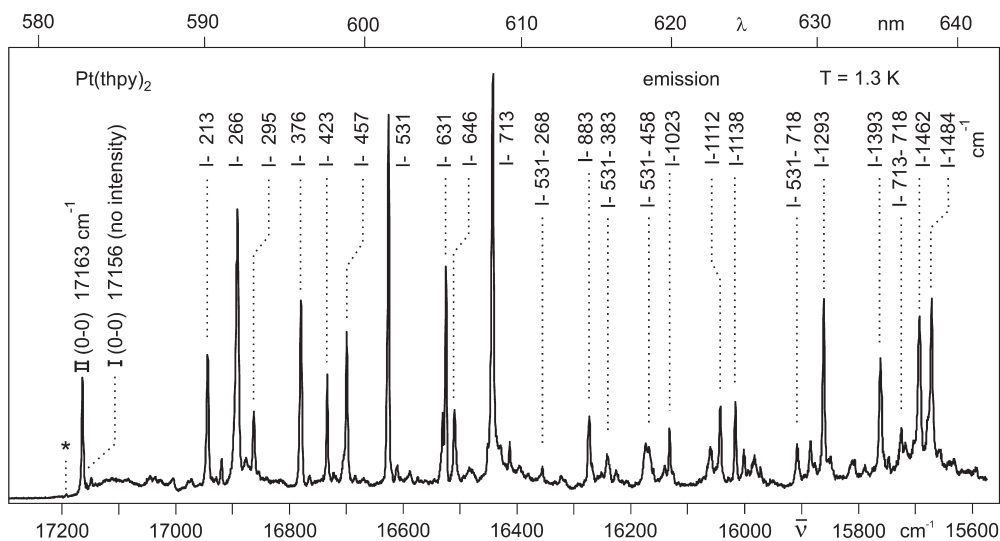


Fig. 1.31 Emission spectrum of $\text{Pt}(\text{thpy})_2$ dissolved in *n*-octane and monitored at $T=1.3\text{ K}$. Concentration $\approx 10^{-5}\text{ mol L}^{-1}$; $\lambda_{\text{exc}}=457.9\text{ nm}$. The vibrational satellites are characterized by their energy separations from the electronic origin $\text{I}(0-0)$ at 17156 cm^{-1} . The asterisk denotes an electronic origin of a different site. The region of the electronic origins is shown in Fig. 1.15, on an enlarged scale.

have significant lattice or chromophore-cage mode character. It should even be taken into account that a mixing of complex vibrations with cage modes is still obvious up to $\approx 150\text{ cm}^{-1}$ [244]. Overlapping with this energy range up to $500/600\text{ cm}^{-1}$, one finds metal–ligand (M-L) vibrations, which can, for example, be identified by a comparison of vibrational energies of $\text{Pt}(\text{thpy})_2$ to those of $\text{Pd}(\text{thpy})_2$ [70].³¹⁾ Fundamentals with energies higher than $\approx 600\text{ cm}^{-1}$ represent internal ligand vibrations. It should be noted that many vibrational satellite lines are accompanied by weak phonon satellites at their low-energy side.

The structure of the 1.3 K emission of $\text{Pt}(\text{thpy})_2$ (Fig. 1.31) is characterized by the absence of the electronic I(0-0) transition, but by an occurrence of intense vibrational satellites. Since: (i) the satellites do not show any distinct progression; and (ii) the electronic origin does not show any intensity, it can be concluded that the satellites do not result from Franck–Condon activity (compare Section 1.9.1.1). All satellites that correspond to fundamentals are vibronically (Herzberg–Teller) induced, and hence represent so-called “false origins”.

In Section 1.9.1.2 and Fig. 1.30, a mechanism has been proposed, which can provide intensity to the vibrational satellites (false origins), even when the electronic transition is spin-forbidden. In particular, for low-energy vibrations below $\approx 600\text{ cm}^{-1}$, which exhibit pronounced metal–ligand character, such as the 266, 295, 376, 531 cm^{-1} modes (Fig. 1.31), it is very probable that the vibrating platinum ion can induce spin-vibronic coupling.

Presumably, this specific mechanism should be extended to describe also the occurrence of satellites of high-energy fundamentals, such as the 1023, 1138, 1293, 1393, and 1462 cm^{-1} vibrations (Fig. 1.31).³²⁾ A corresponding mechanism has been treated theoretically with respect to organic molecules [239–243], and proposed to be of importance also for organo-transition metal compounds, such as $\text{Pt}(\text{thpy})_2$ [70] and $[\text{Os}(\text{bpy})_3]^{2+}$ [206]. It is based on a two-step coupling route, which involves the usual vibronic coupling of state I to a higher-lying triplet substate that experiences on its part effective SOC.

1.9.2.2 Franck–Condon Activity in the Emissions from Substates II and III: The 20 K Spectrum

With a temperature increase, for example to $T = 20\text{ K}$ (Fig. 1.32), the electronic 0-0 transitions II(0-0) and III(0-0) at $17\,163\text{ cm}^{-1}$ and $17\,172\text{ cm}^{-1}$ grow in strongly. This is attributed to the thermal population of the two higher-lying states. Also, the vibrational satellite structure changes and satellites that correspond to fundamen-

31) Due to the largely ligand-centered transition in $\text{Pd}(\text{thpy})_2$, its emission spectrum exhibits only very weak vibrational satellites of M-L mode character.

32) It should also be pointed out that for most of the intense false origins combinations are also observed, such as $(531 + 1484)$, $(713 + 1400)$, $(1462 + 718)\text{ cm}^{-1}$, etc. (not all are shown in Fig. 1.31, but see Refs. [70, 144]). The second member of the

combination represents a vibrational mode which is not Herzberg–Teller active, but shows Franck–Condon activity and corresponds to a totally symmetric mode (see next section). It is remarked that the 1484 cm^{-1} mode seems to be HT and FC active, presumably, two vibrational modes of different symmetry have nearly the same energy.

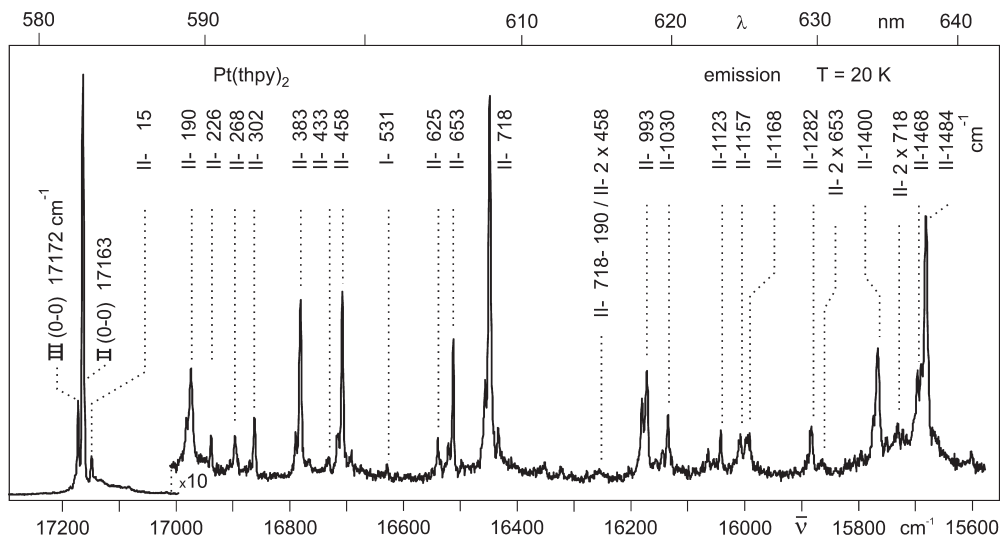


Fig. 1.32 Emission spectrum of Pt(thpy)₂ dissolved in *n*-octane and monitored at $T=20$ K. Concentration $\approx 10^{-5}$ mol L⁻¹; $\lambda_{\text{exc}}=457.9$ nm. The vibrational satellites are characterized by their energy separations from

the electronic origin II(0-0) at 17163 cm⁻¹, apart from the weak 531 cm⁻¹ satellite which belongs to the emission of substate I. The region of the electronic origins is reproduced in Fig. 1.15, on an enlarged scale.

tals different from those found in the 1.3 K emission spectrum, grow in; thus, the emission spectrum changes drastically (compare Figs. 1.31 to 1.32). Moreover, those satellites which dominate at $T=1.3$ K, such as the 531 cm⁻¹ satellite, become weak at higher temperature. Further, in the 20 K emission spectrum, the electronic origin lines II(0-0) and III(0-0) are the dominating peaks. In contrast to the situation of the electronic 0-0 transition $\text{I} \leftrightarrow \text{0}$, they carry significant allowedness. This is evidenced, for example, by the possibility of exciting the substates **II** and **III** directly (see Fig. 1.15a and 1.15d)

The vibrational satellites in the 20 K emission spectrum are observed as vibrational doublets. These all exhibit the same energy separation of 9 cm⁻¹, like the two electronic origins II(0-0) and III(0-0). Thus, the same vibrational modes are active in the radiative processes of both electronic states **II** and **III**. In Fig. 1.32, only satellites of origin II(0-0) (at 17163 cm⁻¹) are specified by marking the vibrational energies.

The 20 K emission spectrum exhibits vibrational satellites due to the activity of fundamentals (e.g., 190, 383, 458, 718, 1400, 1484 cm⁻¹, etc.; see Fig. 1.32), of combinations of these fundamentals [e.g., (190+1484), (383+1400), (458+1484), (718+1400), (718+1484) cm⁻¹, etc.], and for the most intense satellites, also the second members of progressions (e.g., 1×718 cm⁻¹, 2×718 cm⁻¹, 1×1484 cm⁻¹, 2×1484 cm⁻¹) are also observed. Some of these satellites are not displayed in Fig. 1.32 (but see Refs. [70, 144]). These results can be rationalized, when all vibrational satellites with significant intensity are assigned to correspond to totally symmetric fundamentals. This assignment is also in accordance with the observation that the

same fundamentals are built upon the false origins occurring in the 1.3 K emission spectrum. An assignment to an alternative symmetry would not allow us to explain the very distinct differences of vibrational activities found in the emission from the states **I** and **II**, respectively.

Moreover, these totally symmetric fundamentals are assigned to be Franck–Condon active (compare Section 1.9.1.1) and indeed, for the most intense satellites weak overtone satellites are also found. By use of Eq. (22), the corresponding Huang–Rhys parameters S can be estimated. For the most “pronounced” progressions of the 718 and the 1484 cm⁻¹ modes, a value of $S \approx 0.08$ is obtained. The occurrence of other progressions, namely of the fundamentals of 383, 458, and 653 cm⁻¹ is also indicated (Fig. 1.32). However, progressions are not observed for each totally symmetric fundamental. These might exhibit still smaller S parameters, although even for a similar Huang–Rhys parameter of $S \approx 0.08$, most of the corresponding overtone satellites would be hidden in the noise of the spectrum.

The occurrence of only small Huang–Rhys parameters means that the shifts of the equilibrium positions for all vibrational coordinates is small – that is, the triplet geometry of Pt(thpy)₂ is only slightly perturbed with respect to the electronic ground state, at least for the applied rigid low-temperature matrix. An equivalent conclusion can be drawn for almost all triplet emitters hitherto studied by our group [70]. This result implies, indirectly, that the coupling of the excited state(s) of the emitter molecule to its host environment is small. It should be noted that this property may depend on the applied host material; hence, care must be taken when selecting adequate matrix–emitter combinations.

1.9.2.3 Time-Resolved Emission and Franck–Condon/Herzberg–Teller Activities

In Section 1.7.2 and Fig. 1.21 it was shown that the emission of Pt(thpy)₂ decays at $T=1.3$ K biexponentially, with time constants of 600 ns and 110 μs, when the compound is excited non-selectively, for example in the ultraviolet. This behavior is a consequence of a population of substate **II** by very fast ISC processes and of the depletion of this state **II** with a time constant of 600 ns. This decay is mainly determined by the SLR from substate **II** to substate **I**. State **I** is also populated directly by the fast ISC routes and emits with its intrinsic decay time of 110 μs. Thus, during the first about two microseconds after the laser pulse, substate **II** is still populated, and superimposed emissions stemming from both states **I** and **II** with strongly different decay times are obtained. According to the large difference of these time constants, discrimination of the two emission spectra will be possible by applying time-resolved spectroscopy.

Indeed, this is successful, and has been demonstrated in Ref. [245]; the results are illustrated in Fig. 1.33. Figure 1.33a reproduces the emission spectrum detected immediately after the exciting laser pulse ($\lambda_{\text{exc}} = 337.1$ nm, pulse width 0.5 ns) with no time delay ($t=0$ ns) and integrated during a time window of $\Delta t = 500$ ns. Hence, the *fast* and non-delayed emission spectrum which predominantly results from substate **II** is obtained. A totally different spectrum results, when the emission is monitored after a time being long compared to the decay time of 600 ns. For example, with a delay of $t=10$ μs after the laser pulse and an integration time of

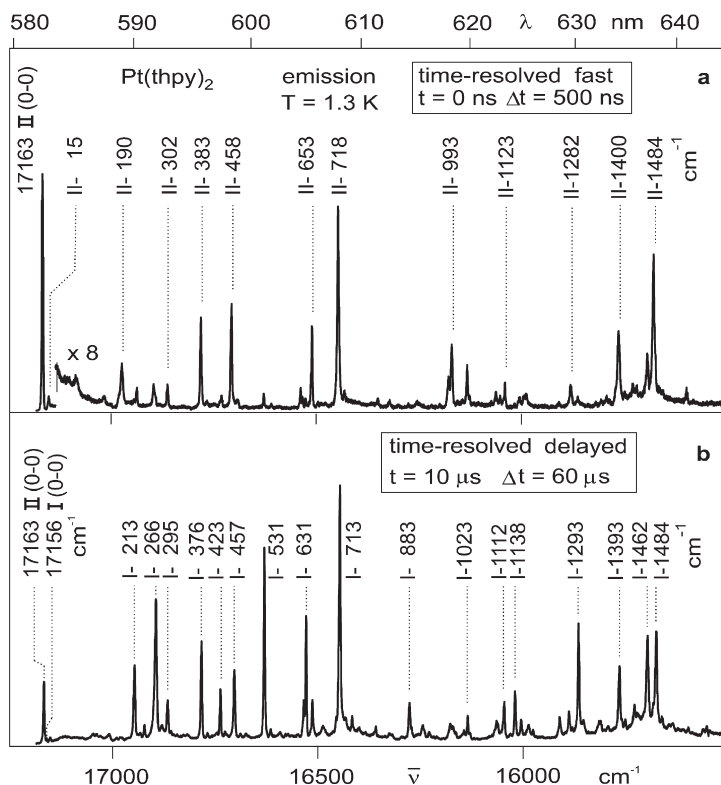


Fig. 1.33 Time-resolved emission of $\text{Pt}(\text{thpy})_2$ dissolved in *n*-octane (ca. $\approx 10^{-5} \text{ mol L}^{-1}$) and monitored at $T = 1.3 \text{ K}$. Excitation: $\lambda_{\text{exc}} = 337.1 \text{ nm}$; pulse width $\approx 0.5 \text{ ns}$; repetition rate 100 Hz . (a) The emission is detected without any delay and integrated over $\Delta t = 500 \text{ ns}$. (b) Detection of the emission after a delay of $t = 10 \mu\text{s}$ and integrated over $\Delta t = 60 \mu\text{s}$. The energies of the vibrational satellites are given in cm^{-1} relative to the electronic origin $\text{II}(0-0)$ (a) and origin $\text{I}(0-0)$ (b), respectively (compare Ref. [245]).

$\Delta t = 60 \mu\text{s}$ (time window), the emission spectrum as reproduced in Fig. 1.33b, is obtained. This spectrum represents the emission of substate I.

The delayed emission spectrum is very similar to the time-integrated emission spectrum measured at $T = 1.3 \text{ K}$ (compare Fig. 1.33b and Fig. 1.31.) Therefore, this delayed spectrum is similarly assignable, as described in Section 1.9.2.1. In particular, all vibrational satellites that are marked in Fig. 1.33b represent false origins, and their intensities are vibronically (Herzberg–Teller) induced. Also, this delayed emission spectrum does not reveal any intensity at the position of the electronic 0-0 transition from $\text{I} \rightarrow 0$.³³⁾

33) The occurrence of the electronic origin $\text{II}(0-0)$ in the time-delayed spectrum (Fig. 1.33b) is not expected at first sight. However, its appearance is a consequence of a thermal repopulation of substate II, according to a

Boltzmann distribution which applies after a sufficiently long delay time and according to the relatively large transition probability of the $\text{II} \rightarrow 0$ transition.

The fast and non-delayed emission spectrum (Fig. 1.33a) shows nearly the same structure as the time-integrated spectrum measured at $T=20$ K (Fig. 1.32). However, the satellites that result from substate **III** (9 cm^{-1} higher-lying peaks of the “doublet” structure in the 20 K emission spectrum) do not occur in the fast spectrum. Obviously, at $T=1.3$ K, an emission of substate **III** is not observed. This is due to very fast SLR processes from substate **III** to the lower lying substates **II** and **I** (compare also Section 1.7). Thus, the fast spectrum represents the non-thermalized emission spectrum of state **II**. The Boltzmann distribution does not apply immediately after the excitation pulse, as the thermal equilibration is relatively slow. (This behavior has been studied in detail also for $[\text{Ru}(\text{bpy})_3]^{2+}$; compare Refs. [74, 185].) The emission spectrum displayed in Fig. 1.33a (fast spectrum) is assigned similarly as discussed in Section 1.9.2.2. In particular, the electronic 0-0 transition **II** \rightarrow **0** (origin **II**(0-0)) strongly dominates the spectrum (note the factor of 8 in Fig. 1.33a), and very probably almost all vibrational satellites are induced by Franck–Condon active vibrations.

In conclusion, it is possible for $\text{Pt}(\text{thpy})_2$, to separate the emission spectra which are superimposed in time-integrated spectra by time-resolved emission spectroscopy. It is important that a low-temperature (1.3 K) emission spectrum from a higher-lying state with the corresponding high spectral resolution can be obtained. This possibility is a consequence of the relatively slow SLR. Vice versa, as the monitored time-resolved emission spectra are clearly assignable to different triplet substates, these results nicely support the concept of a slow SLR, as developed above. Moreover, the results presented clearly reveal the triplet substate selectivity with respect to Franck–Condon and Herzberg–Teller vibrational activity.

To summarize, the vibronic properties are related to the different allowednesses of the purely electronic transitions. The 0-0 transitions from substates **III**, **II** to the ground state **0** are (sufficiently) allowed. Thus, Franck–Condon activity becomes possible. On the other hand, substate **I** represents an almost pure triplet, and therefore, the 0-0 transition to the singlet ground state is forbidden. Moreover, the specific symmetry of substate **I** of $\text{Pt}(\text{thpy})_2$ probably leads additionally to a symmetry forbiddenness (see Section 1.5.2). Nevertheless, radiative deactivation can occur due to the action of molecular vibrations (i.e., due to vibronic coupling). Such a coupling route can provide the adequate symmetry and SOC, and thus can open the vibrational satellite channels. It should be noted that the 0-0 transition still remains forbidden. This model is strongly supported by investigations under the application of high magnetic fields. Due to the field-induced mixing of the wavefunctions of the three triplet substates, the *B*-field-perturbed lowest triplet substate I_B gains relatively high radiative allowedness of the 0-0 transition to the electronic ground state (see Fig. 1.15g). Accordingly, Franck–Condon activity should become possible. Indeed, this behavior of tuning in Franck–Condon activity has been demonstrated in particular for $[\text{Os}(\text{bpy})_3]^{2+}$ [74, 177, 206, 207], for $\text{Pt}(\text{thpy})_2$ [149], $\text{Ir}(\text{btp})_2(\text{acac})$ [246], and indirectly for several other compounds, such as $\text{Ir}(\text{ppy})_3$ [115] and $[\text{Ru}(\text{bpy})_3]^{2+}$ [205] (compare also Refs. [247–249]).

1.9.3

Ir(btp)₂(acac) Emission: Low-Temperature Vibrational Satellite Structure

In this section, the aim is to discuss the low-temperature vibrational satellite structure of the Ir(btp)₂(acac) emission. Figure 1.34 shows the 1.5 K spectrum of the selectively excited site, which is in the focus of Section 1.8 (site H in Section 1.10). The frame on the left-hand side displays the two electronic 0-0 transitions I(0-0) and II(0-0) separated by $\Delta E_{\text{II-I}} = 2.9 \text{ cm}^{-1}$. The II(0-0) transition strongly dominates, due to the much higher transition probability of $\text{II} \leftrightarrow \mathbf{0}$ as compared to $\text{I} \leftrightarrow \mathbf{0}$ and due to the very slow SLR time of $\tau_{\text{SLR}} = 22 \mu\text{s}$ between the two substates (see Section 1.7.2 and Table 1.1). As consequence of this property, the emission from substate II cannot be frozen out (compare Fig. 1.24 and Ref. [203]). Accordingly, both substates emit, and thus the usual (time-integrated) emission spectrum is superimposed of two spectra. However, as depicted in Fig. 1.34, the different vibrational satellites can still be specified with respect to the corresponding electronic origins. This is possible by use of three independent methods:

- Substate II and I, respectively, exhibit different decay times at low temperature due to the effect of SLR. Thus, time-resolved spectroscopy allows separation of the different spectra in the regions of the electronic origins and the vibrational satellites, in a similar manner as described for Pt(thpy)₂ in Section 1.9.2.3 [246].
- With a temperature increase to $T = 4.2 \text{ K}$, the emission results dominantly from substate II, and vibrational

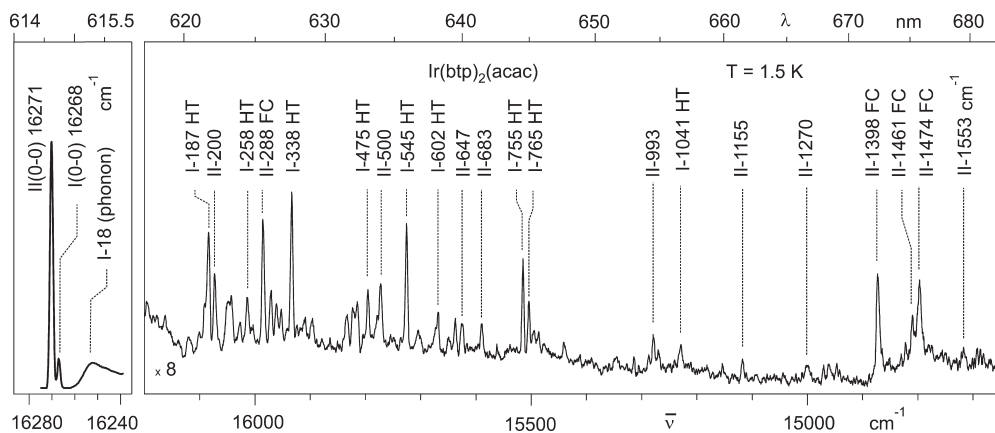


Fig. 1.34 Emission spectrum of site H of Ir(btp)₂(acac) doped into CH₂Cl₂ (ca. $\approx 10^{-5} \text{ mol L}^{-1}$). The frame on the left-hand side shows the region of the two lowest electronic 0-0 transitions on an enlarged scale (compare Fig. 1.24). The spectra were monitored at $T = 1.5 \text{ K}$ under selective excitation of substate

III with an energy of 16293 cm^{-1} . The vibrational satellite lines are labeled according to the electronic origins I(0-0) and II(0-0), and are assigned with respect to the Herzberg–Teller (HT) or Franck–Condon (FC) activity of the corresponding vibrational mode.

satellites from substate I become less important (compare the 4.2 K spectrum in Fig. 1.24).

- Under the application of high magnetic fields, and according to the field-induced admixtures of wavefunctions of the substates II and III to substate I, the resulting perturbed substate I_B changes its properties significantly. In particular, it gains allowedness for the $I_B(0-0)$ transition. The resulting emission spectrum at a high magnetic field, for example at $B=10$ T, corresponds largely to the spectrum of the perturbing states II and III. Consequently those vibrational satellites, which grow in with B -field increase, correspond to vibrational modes which are active in the radiative deactivation of substate II at zero magnetic field [147, 246].

Interestingly, also for $\text{Ir}(\text{btp})_2(\text{acac})$ the different vibrational modes exhibit different activities with respect to the vibronic mechanisms. All vibrational satellites, which belong to the substate I emission, are induced by Herzberg–Teller activity. This conclusion is possible, as the electronic origin transition $I(0-0)$ carries only very little oscillator strength and since no progression is found in the emission spectrum of substate I. On the other hand, for several vibrational satellites, which belong to the substate II emission, also the second members of Franck–Condon progressions are observed, for example for the 288, 1398, 1461, and 1474 cm^{-1} modes. The largest Huang–Rhys parameter for these progressions is estimated by use of Eq. (22) to $S=0.08$. Presumably, almost all other vibrational satellites found in the emission spectrum of substate II are also FC induced, though with smaller Huang–Rhys parameters. In many cases, the second members of vibrational progressions may be hidden in the noise of the spectrum.

In conclusion, the vibrational satellite structure of the $\text{Ir}(\text{btp})_2(\text{acac})$ emission can be described in accordance to the behavior of $\text{Pt}(\text{thpy})_2$. In particular, it is found also for $\text{Ir}(\text{btp})_2(\text{acac})$ (in a rigid low-temperature matrix) that the geometry of the lowest triplet state T_1 is only very slightly perturbed with respect to the geometry of the electronic ground state S_0 .

1.10

Environmental Effects on Triplet State Properties: Case Studies Applied to $\text{Ir}(\text{btp})_2(\text{acac})$

In the preceding sections, we have introduced to photophysical properties of organo-transition metal compounds without addressing specifically the differences of the individual sites – that is, the influence of the specific matrix cage on the electronic behavior of the emitter molecule. Studies show that important properties can be dissimilar, such as transition energies, ZFSs, emission decay times, SLR times, and vibrational satellite structures. These properties vary over specific ranges, which depend on the individual energy state of the emitter and its

host environment. In the following sections, the aim is to outline these dissimilarities on the example of different sites of $\text{Ir}(\text{btp})_2(\text{acac})$ doped into a low-temperature CH_2Cl_2 matrix.

1.10.1

Energy Distribution of Sites

Figure 1.35 shows the low-temperature emission spectrum of $\text{Ir}(\text{btp})_2(\text{acac})$ in CH_2Cl_2 in the region of the electronic 0-0 transitions. This spectrum, which corresponds to the 4.2 K spectrum shown in Fig. 1.23, is characterized by several narrow lines of halfwidths of a few cm^{-1} and a broad background. Both the narrow lines as well as the background can be explained by taking into account that the $\text{Ir}(\text{btp})_2(\text{acac})$ dopants experience dissimilar interactions with their respective environments in the host. Different orientations of the dopants within the host cage and/or a different number of host molecules that are replaced cause dissimilar shifts of the electronic states, splittings, and couplings to the matrix. Since specific energy minima exist for the dopants, discrete sites result and narrow lines occur. Almost each of the narrow lines is related to one specific site. On the other hand, a large number of dopants is inhomogeneously distributed. This leads to the broad background in the emission spectrum (compare also Section 1.11.1).

The different discrete sites of $\text{Ir}(\text{btp})_2(\text{acac})$ are labeled with capital letters in Fig. 1.35. The distribution of sites spans over a width of about 450 cm^{-1} , the most

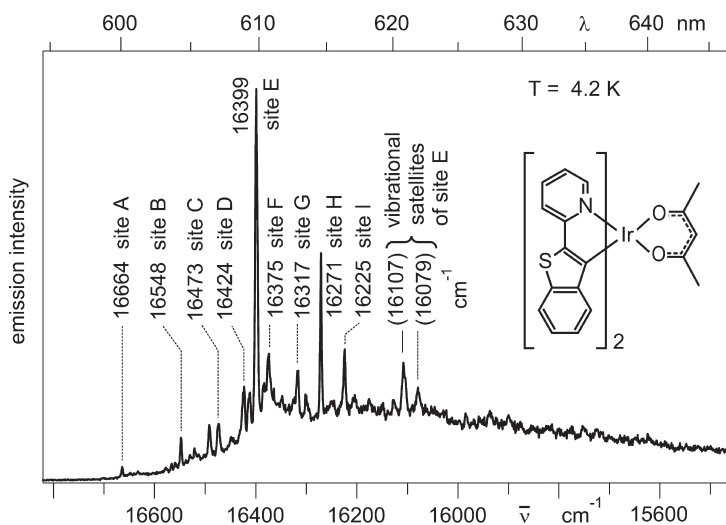


Fig. 1.35 Emission of $\text{Ir}(\text{btp})_2(\text{acac})$ in CH_2Cl_2 in the region of the electronic origins, monitored under UV excitation at $T = 4.2 \text{ K}$. The spectrum consists of resolved electronic 0-0 lines ($\text{II} \rightarrow \text{0}$) of the different sites and of an inhomogeneous background. The different sites are labeled with capital letters.

Table 1.2 Transition energies and zero-field splittings (ZFS) for various sites of Ir(btp)₂(acac) doped into CH₂Cl₂ and *n*-octane, respectively, and for single crystals of Ir(btp)₂(acac). Properties of the sites **E** and **H** are discussed in detail (see text).

Matrix	Site	Relative intensity	Spectral position (cm ⁻¹)			ZFS (cm ⁻¹)	
			I	II	III	ΔE _{II-I}	ΔE _{III-I}
CH ₂ CH ₂	A	0.03	–	16 664	–	–	–
	B	0.09	–	16 548	16 566	–	≈21
	C	0.08	16 470	16 473	16 488	3.2 ± 0.5	17.5 ± 1
	D	0.14	16 422	16 424	16 445	2.2 ± 0.5	23.0 ± 0.5
	E	1	16 396	16 399	16 411	2.9 ± 0.2	14.8 ± 0.5
	F	0.12	–	16 375	≈16 395	–	≈23
	G	0.12	16 314	16 317	16 333	3.7 ± 1	19 ± 3
	H	0.49	16 268	16 271	16 293	2.9 ± 0.2	25.0 ± 0.5
	I	0.19	16 221	16 225	16 247	3.6 ± 0.3	26.5 ± 1
<i>n</i> -Octane	A	0.89	16 198	16 201	16 224	2.5 ± 0.2	25.3 ± 0.5
Single crystal	–	–	16 293	16 296	16 312	3.4 ± 0.4	19 ± 1

dominant site being located at 16 399 cm⁻¹ (site **E**). Sites with weaker intensities are found at higher energies than the main site at least up to 16 664 cm⁻¹, and lower energies at least down to 16 225 cm⁻¹, respectively (Table 1.2).

Most of the lines represent electronic 0-0 transitions from substate **II** of the lowest triplet state **T**₁ to the ground state **O**(**S**₀). This has been confirmed by detailed investigations under selective excitation, variation of temperature, and the application of high magnetic fields (compare Fig. 1.24 and Refs. [147, 203]).

It should be noted that the distribution of transition energies of the different sites due to dissimilar dopant–matrix interactions is a well-known phenomenon in the spectroscopy of organic molecules doped into Shpol'skii or Shpol'skii-like matrices [175, 176, 179]. Organo-transition metal compounds have also been investigated in this respect, though less frequently. For example, different sites were studied of Pt(thpy)₂ [144], Pd(thpy)₂ [244], Pt(II)-phthalocyanines [250, 251], and of the related compounds [Ru(bpy)₃]²⁺ [74, 252] and [Os(bpy)₃]²⁺ [74, 177, 253].

1.10.2

Zero-Field Splittings at Different Sites

The investigation of an individual site can be achieved by site-selective spectroscopy. For Ir(btp)₂(acac) in CH₂Cl₂, emission and excitation spectra have been monitored under selective excitation and detection, respectively. Additionally, variation of temperature and high magnetic field have been applied to ensure a

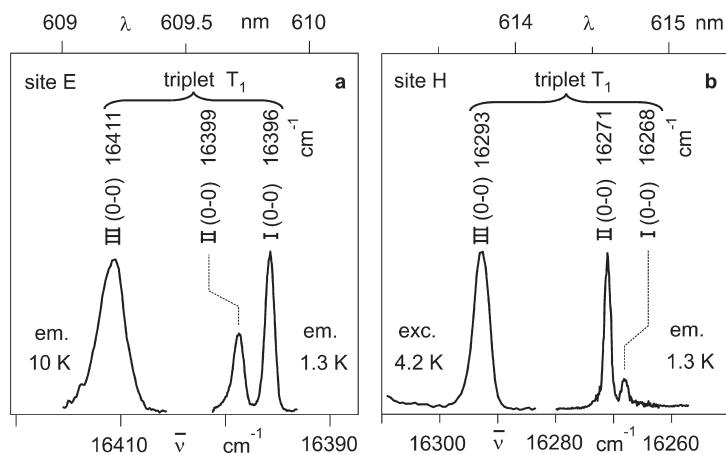


Fig. 1.36 Region of the electronic origins (0-0) transitions of two major sites **E** and **H** of $\text{Ir}(\text{btp})_2(\text{acac})$ in CH_2Cl_2 , as specified in Fig. 1.35. The emission spectra of site **E** and **H** were obtained by exciting into the vibrational satellite of substate **III** at 16775 cm^{-1} ($16411\text{ cm}^{-1} + 364\text{ cm}^{-1}$) and at 16742 cm^{-1} ($16293\text{ cm}^{-1} + 449\text{ cm}^{-1}$), respectively. The

excitation spectrum of site **H** was measured by detection at the electronic origin **II**(0-0) at 16271 cm^{-1} . Note that the intensity ratio of the lines **II**(0-0) to **I**(0-0) is significantly different for the two sites (compare Ref. [203]). This is mainly a consequence of different spin-lattice relaxation times between substates **II** and **I** (see Section 1.10.3).

reliable interpretation of the observed data. Figure 1.36 shows site-selective spectra of the regions of electronic origins for the two specific sites **E** and **H** (Table 1.2). These sites are especially suited for detailed studies due to the high intensities of the corresponding lines compared to the broad background.

The obtained data clearly show that the two sites exhibit distinctly different total zero-field splittings of the T_1 substates. The total ZFS $\Delta E_{\text{III-I}}$ amounts to 14.8 cm^{-1} for site **E** and to 25.0 cm^{-1} for site **H**. The splitting $\Delta E_{\text{II-I}}$ between the two lower substates of 2.9 cm^{-1} is identical for these specific sites, but – as shown in Table 1.2 – this is not the general case. A study of the ZFSs of sites **A** to **I** of $\text{Ir}(\text{btp})_2(\text{acac})$ in CH_2Cl_2 reveals that the total ZFS $\Delta E_{\text{III-I}}$ is distributed from 14.8 cm^{-1} to 26.5 cm^{-1} . Additional investigations of $\text{Ir}(\text{btp})_2(\text{acac})$ in *n*-octane and as a single crystal result in $\Delta E_{\text{III-I}}$ values of 25.3 cm^{-1} and 19 cm^{-1} , respectively. The splitting $\Delta E_{\text{II-I}}$ varies from 2.2 cm^{-1} to 3.7 cm^{-1} for the different sites and matrices. A correlation to the $\Delta E_{\text{III-I}}$ variation does not exist. The ZFS values are summarized in Table 1.2, together with the relative intensities of the lines corresponding to the different sites.

The variation of $\Delta E(\text{ZFS})$ by almost 100% indicates a strong influence of the host on the T_1 state. In Section 1.4, it was shown that the ZFS may be regarded as a measure of the MLCT character of the emitting T_1 state. Presumably, the amount of MLCT admixture to the T_1 state is susceptible to the environment of the complex.

1.10.3

Emission Decay and Spin–Lattice Relaxation Times

Investigations of the decay dynamics between the three substates of T_1 and from the substates to the ground state S_0 show again distinct differences for the different sites of $\text{Ir}(\text{btp})_2(\text{acac})$ doped into CH_2Cl_2 . By using site-selective spectroscopy and varying the temperature, it is possible to determine the emission decay times of the transitions from the substates **I**, **II**, and **III** to the ground state. This procedure is carried out similarly as described in Section 1.6. Whilst for site **H** the values amount to $\tau = 150 \mu\text{s}$, $\tau_{\text{II}} = 58 \mu\text{s}$, and $\tau_{\text{III}} = 2 \mu\text{s}$, one finds for site **E** $\tau_{\text{I}} = 62 \mu\text{s}$, $\tau_{\text{II}} = 19 \mu\text{s}$, and $\tau_{\text{III}} = 3 \mu\text{s}$ [203]. These dissimilarities can result from different radiative allowednesses of the respective transitions and/or from different radiationless deactivation rates to the ground state. The radiative rate might be altered due to different singlet admixtures to the T_1 substates, while the non-radiative deactivation might vary according to different coupling strengths of the electronic states to the lattice. Further studies in this respect are necessary.

The times of SLR between the substates **I** and **II** are, at $T = 1.5 \text{ K}$, $\tau_{\text{SLR}} = 4 \mu\text{s}$ and $22 \mu\text{s}$ for sites **E** and **H**, respectively (compare Section 1.7 and Ref. [203]). This different relaxation behavior manifests itself also in the emission spectra at $T = 1.5 \text{ K}$. As seen in Fig. 1.36, the emission of site **E** is dominated by the transition from the lowest triplet substate **I** to the ground state, while the emission of site **H** stems mainly from substate **II**. For site **H**, substate **II** is only depopulated *slowly* into substate **I** and therefore, a more intense emission stems from **II** [203].

Furthermore, the temperature dependence of the SLR rate is different for the two sites. For site **E**, the SLR rate increases significantly faster with temperature, than for site **H** (not depicted). This is due to the fact that the energy separation $\Delta E_{\text{III-II}}$ is distinctly smaller for site **E** (12 cm^{-1}) than for site **H** (22 cm^{-1}). Therefore, the *Orbach process* of SLR, which depends on this energy separation, has its onset at lower temperature for site **E** (see Section 1.7 and Ref. [203]).

The data in Table 1.3 summarize the decay times of the T_1 substates and the SLR times at 1.5 K for the two major sites **E** and **H** of $\text{Ir}(\text{btp})_2(\text{acac})$ in CH_2Cl_2 ,

Table 1.3 Decay times of the T_1 substates **I**, **II**, and **III** and spin–lattice-relaxation times determined for $\text{Ir}(\text{btp})_2(\text{acac})$ at different sites in CH_2Cl_2 , in *n*-octane, and in a neat single crystal.

Matrix	Site	τ_{I} (μs)	τ_{II} (μs)	τ_{III} (μs)	τ_{SLR}^1 (μs)
CH_2Cl_2	E	62	19	3	4
	H	150	58	2	22
<i>n</i> -Octane	A	105	51	–	57
Single crystal	–	140	–	–	–

1) $T = 1.5 \text{ K}$.

and also provides decay times for the complex in *n*-octane and in a single crystal.

In conclusion, photophysical properties of organo-transition metal complexes can distinctly depend on the individual environment or matrix cage which hosts the emitter complex. The specific interactions between the complex and the environment lead to a variation of the transition energy, the emission decay times, and the ZFSs. It is the subject of further investigations to study the importance of the environmental influence on triplet emitters doped into amorphous polymeric matrices by use of the spectroscopic method of hole burning [254]. It is also intended to analyze to what extent the spread of photophysical properties, as studied at low temperature, survives when the material is used as emitter at ambient temperature and applied in an OLED.

1.11

Emission Linewidths and Spectral Broadening Effects

Detailed information about photophysical properties of the lowest excited states of organo-transition metal compounds can usually only be obtained at cryogenic temperatures, when highly resolved spectra can be recorded. However, in all OLED applications, the compounds are used at ambient temperature. In this situation, the spectral information is smeared out and only broad absorption or emission spectra can be measured. Nevertheless, the photophysical properties determined at low temperature from highly resolved spectra also often govern the emission behavior under ambient conditions. In this section, the aim is to discuss spectral broadening effects which are already present at low temperature, and those broadening effects which occur with temperature increase. Further, it will be shown that emitters with large MLCT character of the triplet state experience specific emission broadening effects.

1.11.1

Inhomogeneous Linewidths

Molecules doped into a solid matrix are always influenced by inhomogeneous interactions with their environments. This occurs also at low temperature in both crystalline and amorphous hosts though usually to a different extent. The electronic and vibrational states of the dopants experience dissimilar shifts, which depend on the individual matrix cage, i.e. – for a given matrix – on the position and orientation of the dopant and the number of matrix molecules in the environment. Consequently, the spectra are shifted with respect to each other, and this results in superimposed spectra. Especially in amorphous matrices such as glasses, the resulting inhomogeneous distribution (which is usually Gaussian-like) is very broad and can reach hundreds of wavenumbers. The width of such a distribution is not easily predictable, as several mechanisms of host–guest interaction can

take effect [255]. On the other hand, the inhomogeneous Gaussian-like width can become relatively small for dopants in crystalline or polycrystalline matrices, such as Shpol'skii matrices. In these hosts, inhomogeneous linewidths may be as small as only 1 or 2 cm^{-1} (compare Sections 1.5, 1.8, and 1.9). In many cases, specific minima exist for dopants in the crystalline hosts, and these give rise to the formation of discrete sites. This leads to the specific lines with the small halfwidths. Often, many different discrete sites are present, as found for $\text{Ir}(\text{btp})_2(\text{acac})$ doped into CH_2Cl_2 (see Table 1.2). Additionally, for the example of the $\text{Ir}(\text{btp})_2(\text{acac})/\text{CH}_2\text{Cl}_2$ combination, many dopants are quasi-continuously distributed over a large number of only slightly different minima. This results in a broad background with a halfwidth of about 400cm^{-1} (Fig. 1.25). In other dopant/matrix combinations, one specific site can dominate clearly. For example, for $\text{Pt}(\text{thpy})_2$ doped into an *n*-octane Shpol'skii matrix, one site carries 98% of the line emission (see Section 1.5.1 and Ref. [144]).

Importantly, for the situations discussed above it is often possible to measure highly resolved spectra of individual sites by applying the well-established methods of site-selective spectroscopy (e.g., see Sections 1.5 and 1.7–1.10), of luminescence line-narrowing (e.g., see Refs. [256, 257]), and of spectral hole burning (e.g., see Ref. [258]), respectively. The application of these methods will, however, only be successful, if the homogeneous line broadening effects do not dominate.

1.11.2

Homogeneous Linewidths

The Heisenberg uncertainty principle correlates an energy uncertainty to the lifetime of a state. This energy uncertainty is identified by the so-called homogeneous linewidth $\Delta\bar{\nu}_{\text{hom}}$ (often referred as Γ_{hom}). It can be expressed by [259, 260]:

$$\Delta\bar{\nu}_{\text{hom}} = \frac{1}{2\pi c\tau_2} \quad (24)$$

wherein c is the velocity of light, and τ_2 is the full dephasing time

$$\frac{1}{\tau_2} = \frac{1}{2\tau_1} + \frac{1}{\tau_2^*} \quad (25)$$

where τ_1 is the excited state lifetime, which for an emission process, is determined by *all* radiative and non-radiative depopulation processes. Therefore, τ_1 is often called *population* or *energy relaxation time*. τ_2^* represents the *pure dephasing time*; this is strongly temperature-dependent and can become very large when zero temperature is approached (see below). In this situation, pure dephasing can be neglected and the homogeneous halfwidth $\Delta\bar{\nu}_{\text{hom}}$ can easily be estimated. (For a

further discussion of τ_2^* , see below.) For example, for an emission decay time of $\tau_1 = 1 \mu\text{s}$, a homogeneous linewidth of $\Delta\bar{\nu}_{\text{hom}} = 2.6 \times 10^{-6} \text{cm}^{-1}$ is obtained. This value is about six orders of magnitude smaller than the inhomogeneous widths found for highly resolved spectra discussed in this contribution.

It should be noted that Eq. (24) is derived under the assumption of an infinite lifetime of one of the involved states. Thus, the presented estimate is well applicable to purely electronic 0-0 transitions. On the other hand, a transition which involves a vibrationally excited state as final state (e.g., a vibrational or phonon satellite line) usually exhibits homogeneous linewidths which are several orders of magnitude larger than those of purely electronic transitions of triplet emitters. This is due to the fast depopulation of the vibrational state, being of the order of 1 ps; consequently, it results an additional uncertainty of the transition energy. Indeed, the vibrational satellite lines of highly resolved emission or excitation spectra exhibit, at low temperature, homogeneous halfwidths of typically 3 to 5cm^{-1} and even up to 10cm^{-1} for vibrational combinations and higher members of progressions. Thus, these linewidths are substantially broader than the inhomogeneously broadened purely electronic origin lines of triplet emitters in suitable hosts or at suitable sites.

With temperature increase, the homogeneous linewidth of a *purely electronic transition* broadens significantly due to the involvement of phonons. In particular, processes of pure dephasing become important [compare τ_2^* in Eq. (25)]. These processes induce phase shifts of the wavefunction of an involved (populated) state, and result in a so-called dephasing of the originally excited situation [98, 261]. Thus, τ_2^* becomes shorter and $\Delta\bar{\nu}_{\text{hom}}$ increases. If, for example, a Raman scattering process of phonons is taken into account, it can be derived that τ_2^* increases with a T^7 temperature dependence [98, 262]. Further, for triplet substates with thermally accessible higher-lying substates, the Orbach process is also expected to be of importance. (In this context, it is referred to elastic up-and-down processes that involve the same two energy substates.) In general, such processes can occur not only by scattering of phonons, but also by interactions of any other kind of elementary excitations with the dopant [259].

The above discussion refers only to the homogeneous broadening of a purely electronic 0-0 line – that is, the electronic zero-phonon line (ZPL). However, important homogeneous broadening effects result additionally from the involvement of specific phonons, for example, of low-energy vibrations or librations³⁴⁾ of the dopant in its lattice cage (local phonons) in the optical transition. This leads to the occurrence of phonon satellites, which lie in a range of less than about 100cm^{-1} from the electronic origin [compare Fig. 1.15b,c (Section 1.5.1) and Fig. 1.31 (Section 1.9.2.1)]. In several cases, some of these local phonon satellites, with phonon energies of 15 or 18cm^{-1} , for example, are resolvable for organo-transition metal complexes dissolved in crystalline matrices. However, mostly only unresolved phonon wings or *phonon sidebands* are found [98]. At low temperature, the phonon sidebands are

34) Librations are hindered rotational motions of the dopant molecule in the cage of the surrounding matrix.

situated at the low energy side of the electronic ZPL. The structure and width of a phonon sideband depend on the local situation – that is, on the number of coupling (local) phonons and on the coupling strength of the electronic transition to the phonons, the so-called electron-phonon coupling.

These latter properties are directly related to the effects of the Franck–Condon activity of a specific mode (see Section 1.9.1.1). For example, a large geometry change with respect to a local phonon coordinate according to an electronic transition (large electron–phonon coupling) leads to a large $\Delta Q(\text{phonon})$ value and thus to a large Huang–Rhys parameter $S(\text{phonon})$ for the specific local phonon mode [Eq. (21)]. This results in a distinct phonon progression and a shift of the emission intensity from the purely electronic line (ZPL) to the local phonon satellites (compare Fig. 1.29). As discussed above, the phonon satellites have homogeneous linewidths, which are orders of magnitude broader than those of the electronic ZPL. Furthermore, usually different local phonon modes of different energies couple to the electronic transition. All of the resulting phonon satellites overlap and lead to the broad phonon sidebands.

With temperature increase, an emission can also occur from a thermally populated higher-lying phonon state, and this leads to an energetically higher lying sideband (anti-Stokes phonon sideband). As consequence, the intensity of an emission spectrum is redistributed. It is moved from the ZPL to its phonon sideband mainly at the anti-Stokes side (Fig. 1.37). If the temperature dependence of non-radiative relaxation processes can be neglected, the total intensity of ZPL and sideband is constant. At higher temperatures – mostly already below 77 K (but see the exception of Pt(thpy)₂; Section 1.11.3) – the emission intensity is found only in the phonon sideband and no longer in the ZPL (the spectrum at the right-hand side of Fig. 1.37).

For completeness, it should be noted that the considerations presented above for the purely electronic transitions and their coupling properties to local phonon modes, apply similarly to all vibrational satellites of metal–ligand or ligand vibrational character (compare Section 1.9). In this sense, the vibrational satellite lines

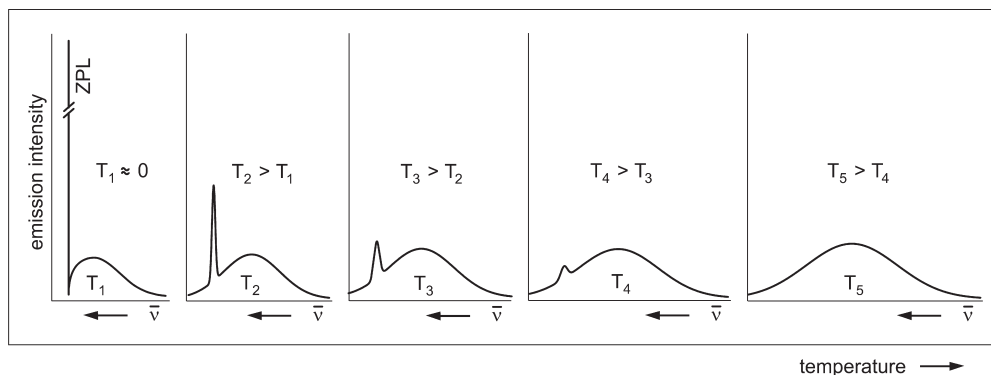


Fig. 1.37 Temperature dependence of a zero-phonon line (ZPL) and the accompanying phonon sideband in emission (compare Ref. [259]).

represent ZPL. The intensity of the phonon side-band is given by the individual coupling of the respective vibrational satellite transition to the local phonons.

1.11.3

Line Broadening Effects on the Example of Pt(thpy)₂

Here, the aim is to illustrate the temperature-broadening effects of the purely electronic origin (electronic ZPL) of Pt(thpy)₂ doped into *n*-octane. At $T=10$ K, the dominating emission line at $17\,163\text{ cm}^{-1}$ represents the purely electronic transition from triplet substate II to the electronic ground state 0 (Fig. 1.38a). Weak lines corresponding to a local phonon satellite of 15 cm^{-1} and the purely electronic III(0-0) line are also observed in this spectral range (compare also Fig. 1.15). The line II(0-0) is inhomogeneously broadened to about 3 cm^{-1} . With a temperature increase to 77 K, the halfwidth of the electronic ZPL is broadened to $\approx 20\text{ cm}^{-1}$, and the intensity is reduced and distributed to the associated phonon sideband. With further temperature increase, the ZPL becomes even weaker, and above ≈ 130 K can no longer be distinguished from the phonon sideband. The integrated intensity stays largely constant from 10 K to 90 K, and decreases only slightly above 90 K.

At a temperature higher than ≈ 90 K, the width of the observed phonon sideband is of the order of 100 cm^{-1} (Fig. 1.38b). Thus, it becomes clear that high-resolution spectroscopy is only possible at low temperatures, usually below 30 to 40 K in the case of Shpol'skii matrices. Below this temperature, homogeneous broadening is weak then and the spectra are dominated by electronic and vibrational satellite ZPLs. This is especially important for organo-transition metal compounds, for which the vibrational satellite lines lie close in energy, with an average separation below 50 to 100 cm^{-1} . Therefore, the appearance of phonon sidebands at higher temperatures leads to a smearing out of the spectrum and to a loss of information.

In general, it is not predictable at which temperature the homogeneous line broadening becomes dominant. For Pt(thpy)₂ in *n*-octane, even at 110 K a weak ZPL is observable and, due to the occurrence of only one single site, comparatively

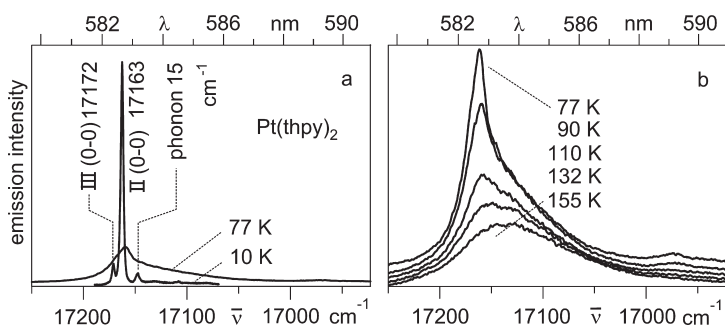


Fig. 1.38 Emission spectra in the region of the electronic origins of Pt(thpy)₂ in *n*-octane (ca. $\approx 10^{-5}\text{ mol L}^{-1}$) at different temperatures. Excitation at 355 nm. Upon increase of temperature, a decrease of the ZPL intensity and an intensity distribution to the broad phonon sideband is observed.

well-resolved spectra can be obtained. However, mostly – also in Shpol'skii matrices – spectra of several discrete sites will occur. The spectra will be superimposed and then smeared out due to the homogeneous effects. Depending on the importance of homogeneous and inhomogeneous broadenings and the extent of site distributions, a broad and unresolved or a well structured spectrum, as in the case of $\text{Pt}(\text{thpy})_2$, can result.

To summarize, at low temperature, a typical emission spectrum of an organo-transition metal compound consists of a purely electronic transition (electronic ZPL) which is accompanied by phonon satellites or, if smeared out, by phonon sidebands. Further, the electronic transition is also associated with vibrational satellites (vibrational satellite ZPL) which are also accompanied by phonon sidebands. In case of an occurrence of different sites and/or of an inhomogeneous distribution, a number of spectra will be superimposed. However, by use of the methods of site-selective spectroscopy or of luminescence line-narrowing, a well defined site can still be investigated. However, if electron–phonon coupling is large [large phonon Huang–Rhys parameter $S(\text{phonon})$], the ZPLs might no longer be detectable. In this situation, the spectrum is homogeneously broadened and application of high-resolution methods is unsuccessful, even at low temperature.

When the temperature is increased, homogeneously broadened phonon sidebands gain intensity, and the electronic as well as the vibrational satellite ZPLs disappear (Fig. 1.37) and consequently the whole spectrum becomes broad. High-resolution methods would not be applicable successfully in this situation. The corresponding temperature at which any resolution is lost lies at about 60 K for $\text{Ir}(\text{btp})_2(\text{acac})$ in CH_2Cl_2 and at 110 K for $\text{Pt}(\text{thpy})_2$ in *n*-octane (see above).

At this point, attention should be drawn to an interesting broadening mechanism which especially applies to compounds with emitting triplet states of high MLCT character. These compounds are of special attraction for OLED applications. At low temperature, the emission spectra can often be very well resolved, even for a typical MLCT emitter such as $[\text{Os}(\text{bpy})_3]^{2+}$ [177, 253]. The emission spectra are characterized by the occurrence of many particularly pronounced vibrational satellites of metal–ligand vibrational character. These modes have energies below $\approx 600\text{ cm}^{-1}$, and thus the corresponding ZPLs lie between the ZPLs of the ligand modes and the ZPL of the purely electronic transition. With temperature increase, the homogeneous broadening mechanisms become effective and smear out the whole spectrum. Consequently, the spectra are usually much broader than those corresponding to typical ligand-centered transitions.

1.11.4

Phenomenological Simulation of Spectral Broadening

At very low temperature, it is frequently possible to obtain highly resolved spectra of organo-transition metal complexes and to elucidate photophysical properties. The question arises, however, of whether these properties remain relevant for the emission behavior at 77 K or even at 300 K; that is, for example, for a complex, which is incorporated in an OLED. This question is addressed here simply on a

spectral basis; that is, it is checked whether it is possible to simulate the high-temperature spectra from the low-temperature, highly resolved spectra. The corresponding spectral modifications can, in principle, be accomplished by performing a convolution of the highly resolved line spectrum with the shape function determined by the different mechanisms of temperature broadening. However, the physically relevant function which takes into account overlapping spectra of different sites and homogeneous broadening effects cannot be given. Thus, as a simple approach, it makes sense to apply a Gaussian function, i.e. to convolve the highly resolved spectra with a broadening Gaussian distribution function of a halfwidth of $\Delta\bar{\nu}(\text{FWHM}) = 2.35\sigma$, wherein σ represents the well-known Gaussian σ . (FWHM: full width at half maximum) The parameter σ has to be adapted to reproduce the measured spectra.

Figure 1.39 shows that this procedure is successful, when applied to the highly resolved 4.2 K spectra of $\text{Pt}(\text{thpy})_2$. By using a Gaussian width of 65 cm^{-1} (FWHM),

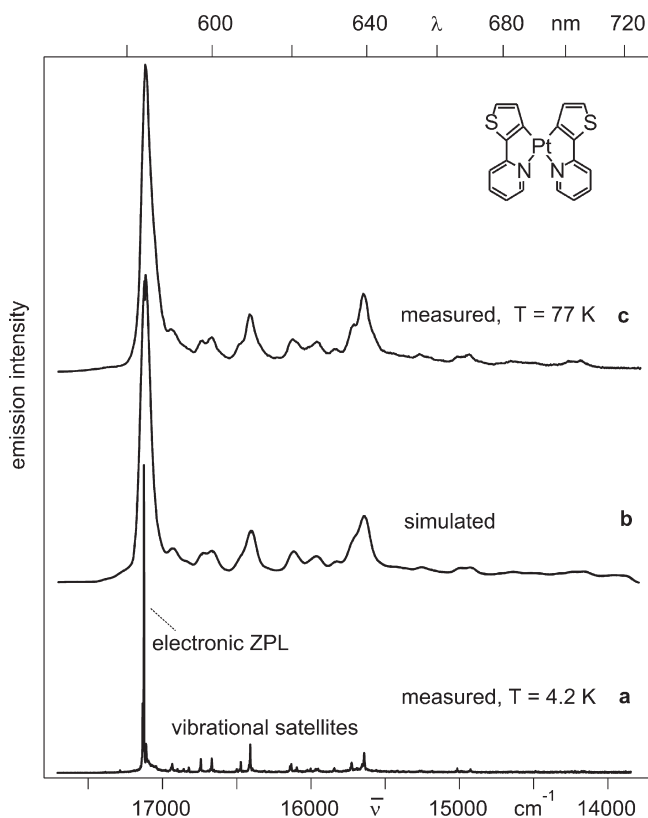


Fig. 1.39 Emission spectra of $\text{Pt}(\text{thpy})_2$ in *n*-octane. (a) Spectrum measured at $T = 4.2\text{ K}$ under non-selective excitation at 457.9 nm . The spectrum has been red-shifted by 43 cm^{-1} to be able to simulate also the spectral position of the 77 K spectrum. (b) Simulated spectrum using a Gaussian distribution function with $\Delta\bar{\nu} = 65\text{ cm}^{-1}$ ($\sigma = 27.6\text{ cm}^{-1}$). (c) Spectrum measured at $T = 77\text{ K}$, excitation wavelength as in (a).

the procedure simulates the measured 77 K spectrum nicely. All spectral features are reproduced, and even the relative intensities of the simulated bands match closely to those of the measured spectrum.

The simulation can also be carried out to obtain a 300 K spectrum. In a physical model, additional line broadenings due to dynamic effects in the liquid solvent must be considered. The phenomenological simulation, however, takes these effects into account simply by using a Gaussian width of $\Delta\bar{\nu}(\text{FWHM}) = 500\text{ cm}^{-1}$. The resulting simulation shows a very good agreement with the measured 300 K emission spectrum (Fig. 1.40). This fitting procedure reflects the enormous broadening of the spectrum, even when compared to the 77 K spectrum. In the resulting spectrum, only three bands are recognized: the maximum at 17100 cm^{-1} represents mainly the broadened phonon sideband of the electronic origin, while the two features at 15710 cm^{-1} and 14220 cm^{-1} correspond to overlapping (sidebands of) vibrational satellites, which result from combinations and progressions of modes lying in the 1400 to 1500 cm^{-1} range.

In conclusion, the high-temperature spectra of many organo-transition metal compounds, and in particular of $\text{Pt}(\text{thpy})_2$, can be traced back to low-temperature, highly resolved spectra. Consequently, the information elucidated for the emitting

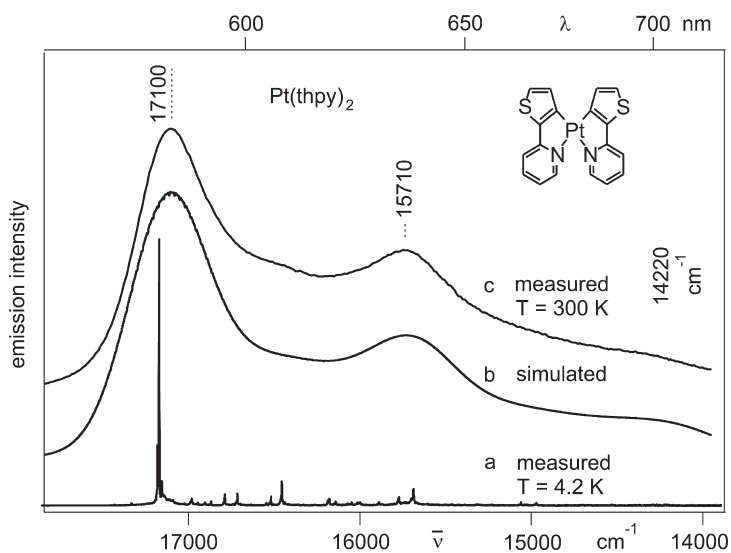


Fig. 1.40 Emission spectra of $\text{Pt}(\text{thpy})_2$ in *n*-octane. (a) Spectrum measured at $T = 4.2\text{ K}$ (for further data, see Fig. 1.39). (b) Simulated spectrum using a Gaussian distribution function with $\Delta\bar{\nu} = 500\text{ cm}^{-1}$ ($\sigma = 213\text{ cm}^{-1}$). (c) Spectrum measured at $T = 300\text{ K}$.

states at low temperatures retains relevance also for emission properties at ambient temperature.

1.12 Conclusions

For many years, a deeper understanding of the triplet state properties of organo-transition metal compounds has been in the focus of fundamental research. However, within the past decade these activities have been greatly stimulated by the beginning application of these compounds as OLED emitters. Nonetheless, many questions remain unanswered. Clearly, OLEDs are applied at ambient or higher temperatures, but even when the technical application is in the focus of interest, the required detailed characterization and insight into the compound's properties cannot be obtained by using only high-temperature studies. This is due to the fact that the emission processes are always averaged or smeared out and, as a consequence, much information is lost. Therefore, it is required to investigate these emitter materials down to low temperature, for example to $T=1.3$ K. Indeed, such studies reveal that the emitting triplet (usually) splits into three substates, and thus access to the individual substate emission becomes possible. In particular, information is obtained regarding the magnitude of the splitting (the ZFS), emission decay dynamics and decay times, radiative deactivation paths as purely electronic transitions or under involvement of internal vibrations and/or low-energy phonon modes, geometry changes of the emitter compound due to excitation of the triplet state, etc.. Most of these properties also show a dependence on the direct environment of the complex. Of particular interest are the discovered trends between the magnitude of ZFS and the photophysical properties of the emitter materials. Thus, the amount of ZFS represents a very valuable parameter.

One of these trends is of particular concern for OLED applications. This is due to the fact that the magnitude of ZFS is determined by SOC to higher-lying singlet and triplet MLCT states. Specifically, the occurrence of a significant ZFS indicates pronounced admixtures of 1 MLCT components to the triplet substates. Such singlet admixtures usually lead to short emission decay times and can result in high photoluminescence quantum yields; also quenching effects of triplet-triplet annihilation can become less important. It is well known that these properties are crucial for emitters applied in OLEDs. As a rule of thumb, it is found that emitter materials, which are successfully applied in OLEDs, have ZFSs of not less than about 10 cm^{-1} . However, those emitters which are employed at high current densities in high-brightness applications, should exhibit even larger ZFSs and strong singlet admixtures to further reduce the emission decay time. Interestingly, it has been shown that the relevant SOC routes can be significantly more efficient in quasi-octahedral than in quasi-square planar compounds. For example, whilst large ZFSs (i.e., $>40\text{ cm}^{-1}$) have not yet been observed for quasi-square planar Pt(II) compounds, but frequently occur in Ir(III), Os(II), or even Ru(II) complexes. Clearly, the success of the quasi-octahedral Ir(ppy)₃ as OLED emitter material is related to this trend.

In particular, these latter results show that detailed studies of the emission processes in organo-transition metal complexes can indeed lead to a better understanding of the correlation between molecular structures and photophysical properties which are of interest for a specific application as emitter material, for example in an OLED.

Acknowledgements

The authors thank the “Bundesministerium für Bildung und Forschung” for providing funding.

References

- 1 J. Shinar (Ed.), *Organic Light-Emitting Devices*, Springer, AIP Press, Berlin, 2004.
- 2 Z. H. Kafafi (Ed.), *Organic Electroluminescence*, Taylor and Francis, CRC Series, Boca Raton, 2005.
- 3 K. Müllen, U. Scherf (Eds.), *Organic Light-Emitting Devices – Synthesis, Properties, and Applications*, Wiley-VCH, Weinheim, 2006.
- 4 J. Kalinowski, *Organic Light-Emitting Diodes: Principles, Characteristics, and Processes*, CRC Press, Boca Raton, 2004.
- 5 H. Yersin, *Top. Curr. Chem.* **2004**, 241, 1.
- 6 R. C. Evans, P. Douglas, C. J. Winscom, *Coord. Chem. Rev.* **2006**, 250, 2093.
- 7 K. Walzer, B. Maennig, M. Pfeiffer, K. Leo, *Chem. Rev.* **2007**, 107, 1233.
- 8 A. Tsuboyama, S. Okada, K. Ueno, this volume, pp. 163.
- 9 A. van Dijken, K. Brunner, H. Börner, B. M. W. Langeveld, this volume, pp. 311.
- 10 X.-H. Yang, F. Jaiser, D. Neher, this volume, pp. 221.
- 11 D. Tanaka, H. Sasabe, Y.-J. Li, S.-J. Su, T. Takeda, J. Kido, *Jap. J. Appl. Phys.* **2007**, 46, L10.
- 12 S. Watanabe, N. Ide, J. Kido, *Jap. J. Appl. Phys.* **2007**, 46, 1186.
- 13 T. Sajoto, P. I. Djurovich, A. Tamayo, M. Yousufuddin, R. Bau, M. E. Thompson, R. J. Holmes, S. R. Forrest, *Inorg. Chem.* **2005**, 44, 7992.
- 14 Y. Sun, N. C. Giebink, H. Kanno, B. Ma, M. E. Thompson, S. R. Forrest, *Nature* **2006**, 440, 908.
- 15 C. Borek, K. Hanson, P. I. Djurovich, M. E. Thompson, K. Aznavour, R. Bau, Y. Sun, S. R. Forrest, J. Brooks, L. Michalski, J. Brown, *Angew. Chem. Int. Ed.* **2007**, 46, 1109.
- 16 S. C. F. Kui, I. H. T. Sham, C. C. C. Cheung, H.-W. Ma, B. Yan, N. Zhu, C.-M. Che, W.-F. Fu, *Chem. Eur. J.* **2007**, 13, 417.
- 17 Y.-Y. Lin, S.-C. Chan, M. C. W. Chan, Y.-J. Hou, N. Zhu, C.-M. Che, Y. Liu, Y. Wang, *Chem. Eur. J.* **2003**, 9, 1263.
- 18 Y. Ma, H. Zhang, J. Shen, C.-M. Che, *Synth. Met.* **1998**, 94, 245.
- 19 C.-H. Yang, Y.-M. Cheng, Y. Chi, C.-J. Hsu, F.-C. Fang, K.-T. Wong, P.-T. Chou, C.-H. Chang, M.-H. Tsai, C.-C. Wu, *Angew. Chem. Int. Ed.* **2007**, 46, 2418.
- 20 P.-T. Chou, Y. Chi, *Chem. Eur. J.* **2007**, 13, 380.
- 21 E. B. Namdas, A. Ruseckas, I. D. W. Samuel, S.-C. Lo, P. L. Burn, *J. Phys. Chem. B* **2004**, 108, 1570.
- 22 R. N. Bera, N. Cumpstey, P. L. Burn, I. D. W. Samuel, *Adv. Funct. Mater.* **2007**, 17, 1149.
- 23 J. Ding, J. Gao, Y. Cheng, Z. Xie, L. Wang, D. Ma, X. Jing, F. Wang, *Adv. Funct. Mater.* **2006**, 16, 575.
- 24 L. Chen, H. You, C. Yang, D. Ma, J. Qin, *Chem. Commun.* **2007**, 1352.
- 25 R. Meerheim, K. Walzer, M. Pfeiffer, K. Leo, *Appl. Phys. Lett.* **2006**, 89, 061111.

- 26 G. Schwartz, K. Fehse, M. Pfeiffer, K. Walzer, K. Leo, *Appl. Phys. Lett.* **2006**, *89*, 083509.
- 27 Y. Kawamura, K. Goushi, J. Brooks, J. Brown, H. Sasabe, C. Adachi, *Appl. Phys. Lett.* **2005**, *86*, 071104.
- 28 X. H. Yang, F. Jaiser, S. Klinger, D. Neher, *Appl. Phys. Lett.* **2006**, *88*, 021107.
- 29 F.-I. Wu, X.-H. Yang, D. Neher, R. Dodda, Y.-H. Tseng, C.-F. Shu, *Adv. Funct. Mater.* **2007**, *17*, 1085.
- 30 A. J. Wilkinson, H. Puschmann, J. A. K. Howard, C. E. Foster, J. A. G. Williams, *Inorg. Chem.* **2006**, *45*, 8685.
- 31 M. Cocchi, D. Virgili, V. Fattori, D. L. Rochester, J. A. G. Williams, *Adv. Funct. Mater.* **2007**, *17*, 285.
- 32 M. S. Lowry, S. Bernhard, *Chem. Eur. J.* **2006**, *12*, 7970.
- 33 E. L. Williams, K. Haavisto, J. Li, G. E. Jabbour, *Adv. Mater.* **2007**, *19*, 197.
- 34 T. Tsuzuki, S. Tokito, *Adv. Mater.* **2007**, *19*, 276.
- 35 E. Holder, B. M. W. Langeveld, U. S. Schubert, *Adv. Mater.* **2005**, *17*, 1109.
- 36 K. Brunner, A. van Dijken, H. Börner, J. J. A. M. Bastiaansen, N. M. M. Kiggen, B. M. W. Langeveld, *J. Am. Chem. Soc.* **2004**, *126*, 6035.
- 37 G. Zhou, W.-Y. Wong, B. Yao, Z. Xie, L. Wang, *Angew. Chem.* **2007**, *119*, 1.
- 38 X. Wang, J. Li, M. E. Thompson, J. I. Zink, *J. Phys. Chem. A* **2007**, *111*, 3256.
- 39 C.-H. Fang, Y.-L. Chen, C.-H. Yang, Y. Chi, Y.-S. Yeh, E. Y. Li, Y.-M. Cheng, C.-J. Hsu, P.-T. Chou, C.-T. Chen, *Chem. Eur. J.* **2007**, *13*, 2686.
- 40 L.-L. Wu, C.-H. Yang, I.-W. Sun, S.-Y. Chu, P.-C. Kao, H.-H. Huang, *Organometallics* **2007**, *26*, 2017.
- 41 R. Schlaf, B. A. Parkinson, P. A. Lee, K. W. Nebesny, G. Jabbour, B. Kippelen, N. Peyghambarian, N. A. Armstrong, *J. Appl. Phys.* **1998**, *84*, 6729.
- 42 X. Ren, J. Li, R. J. Holmes, P. I. Djurovich, S. R. Forrest, M. E. Thompson, *Chem. Mater.* **2004**, *16*, 4743.
- 43 Y.-H. Niu, M. S. Liu, J.-W. Ka, A. K.-Y. Jen, *Appl. Phys. Lett.* **2006**, *88*, 093505.
- 44 M. E. Thompson, private communication.
- 45 C. Adachi, M. A. Baldo, M. E. Thompson, S. R. Forrest, *J. Appl. Phys.* **2001**, *90*, 5048.
- 46 M. A. Baldo, C. Adachi, S. R. Forrest, *Phys. Rev. B* **2000**, *62*, 10967.
- 47 (a) S. Reineke, K. Walzer, K. Leo, *Phys. Rev. B* **2007**, *75*, 125328; (b) W. Staroske, M. Pfeiffer, K. Leo, M. Hoffmann, *Phys. Rev. Lett.* **2007**, *98*, 197402.
- 48 G. He, M. Pfeiffer, K. Leo, M. Hofmann, J. Birnstock, R. Pudzich, J. Salbeck, *Appl. Phys. Lett.* **2004**, *85*, 3911.
- 49 H. J. Peng, X. L. Zhu, J. X. Sun, X. M. Yu, M. Wong, H. S. Kwok, *Appl. Phys. Lett.* **2006**, *88*, 033509.
- 50 T. Canzler, A. G. Novald, Oral Presentation at: *Photonics China*, Shanghai, **2005**.
- 51 T.-Y. Cho, C.-L. Lin, C.-C. Wu, *Appl. Phys. Lett.* **2006**, *88*, 111106.
- 52 H. Peng, J. Sun, X. Zhu, Y. Yu, M. Wong, H.-S. Kwok, *Appl. Phys. Lett.* **2006**, *88*, 073517.
- 53 J. Y. Lee, *Appl. Phys. Lett.* **2006**, *88*, 073512.
- 54 Q. Huang, K. Walzer, M. Pfeiffer, V. Lyssenko, G. He, K. Leo, *Appl. Phys. Lett.* **2006**, *88*, 113515.
- 55 Y. Y. Yuan, S. Han, D. Grozea, Z. H. Lu, *Appl. Phys. Lett.* **2006**, *88*, 093503.
- 56 B. C. Krummacher, V.-E. Choong, M. K. Mathai, S. A. Choulis, F. So, F. Jermann, T. Fiedler, M. Zachau, *Appl. Phys. Lett.* **2006**, *88*, 113506.
- 57 S. W. Kim, J. H. Park, S. S. Oh, D. Y. Kim, E. H. Choi, G. S. Cho, Y. H. Seo, S. O. Kang, B. Park, Y. Saito, N. Watanabe, H. Takezoe, J. Watanabe, *Appl. Phys. Lett.* **2006**, *89*, 213511.
- 58 K. Fehse, K. Walzer, G. He, M. Pfeiffer, K. Leo, W. Loevenich, A. Elschner, *Proc. SPIE (Organic Optoelectronics and Photonics II) Vol. 6192*, **2006**, 61921Z.
- 59 J. H. Park, S. S. Oh, S. W. Kim, E. H. Choi, B. H. Hong, Y. H. Seo, G. S. Cho, B. Park, *Appl. Phys. Lett.* **2007**, *90*, 153508.
- 60 X. Yang, D. C. Müller, D. Neher, K. Meerholz, *Adv. Mater.* **2006**, *18*, 948.
- 61 S. Lamansky, R. C. Kwong, M. Nugent, P. I. Djurovich, M. E. Thompson, *Org. Electron.* **2001**, *2*, 53.

- 62 X. Gong, W. Ma, J. C. Ostrowski, G. C. Bazan, D. Moses, A. J. Heeger, *Adv. Mater.* **2004**, 16, 615.
- 63 P. A. Lane, L. C. Palilis, D. F. O'Brien, C. Giebeler, A. J. Cadby, D. G. Lidzey, A. J. Campbell, W. Blau, D. D. C. Bradley, *Phys. Rev. B* **2001**, 63, 235206.
- 64 K.-H. Hellwege, *Einführung in die Festkörperphysik*, Springer-Verlag, Berlin, p. 509, 1976.
- 65 J. Kalinowski, in: Z. H. Kafafi (Ed.), *Organic Electroluminescence*, Taylor and Francis, CRC Series, Boca Raton, **2005**, p. 23.
- 66 M Schott, *C. R. Acad. Sci. Paris*, tome 1, Série IV, **2000**, 381.
- 67 M. J. Walter, J. M. Lupton, this volume, p. 99.
- 68 M. Reufer, J. J. Walter, P. G. Lagoudakis, A. B. Hummel, J. S. Kolb, H. G. Roskos, U. Scherf, J. M. Lupton, *Nature Mater.* **2005**, 4, 340.
- 69 H. Yersin, *Proc. SPIE* 5214, 124, 2004 Oral presentation at the SPIE conference 5214, San Diego, August, **2003**.
- 70 H. Yersin, D. Donges, *Top. Curr. Chem.* **2001**, 214, 81.
- 71 D. Donges, J. K. Nagle, H. Yersin, *Inorg. Chem.* **1997**, 36, 3040.
- 72 W. Humbs, H. Yersin, *Inorg. Chem.* **1996**, 35, 2220.
- 73 H. Yersin, W. Humbs, J. Strasser, *Coord. Chem. Rev.* **1997**, 159, 325.
- 74 H. Yersin, W. Humbs, J. Strasser, *Top. Curr. Chem.* **1997**, 191, 153.
- 75 M. Klessinger, *Elektronenstruktur organischer Moleküle*, Verlag Chemie, Weinheim, **1982**.
- 76 C. Cohen-Tannoudji, B. Diu, F. Laloë, *Quantum Mechanics*, Vol. I, p. 109, Wiley, New York, **1977**.
- 77 S. P. McGlynn, T. Azumi, M. Kinoshita, *Molecular Spectroscopy of the Triplet State*, Prentice-Hall, Englewood Cliffs, New Jersey, **1969**.
- 78 N. J. Turro, *Modern Molecular Photochemistry*, Benjamin-Cummings, Menlo Park, Calif. p. 31, **1978**.
- 79 N. Mataga, T. Kubota, *Molecular Interactions and Electronic Spectra*, Marcel Dekker, New York, p. 187, **1970**.
- 80 M. Maestri, D. Sandrini, V. Balzani, L. Chassot, P. Jolliet, A. von Zelewsky, *Chem. Phys. Lett.* **1985**, 122, 375.
- 81 N. E. Geacintov, C. E. Swenberg, in: M.D. Lumb (Ed.), *Luminescence Spectroscopy*, Academic Press, London, p. 239, **1978**.
- 82 T. Azumi, H. Miki, *Top. Curr. Chem.* **1997**, 191, 1.
- 83 M. Glasbeek, *Top. Curr. Chem.* **2001**, 213, 96.
- 84 Y. Komada, S. Yamauchi, N. Hirota, *J. Phys. Chem.* **1986**, 90, 6425.
- 85 H. Yersin, D. Donges, J. K. Nagle, R. Sitters, M. Glasbeek, *Inorg. Chem.* **2000**, 39, 770.
- 86 D. Donges, J. K. Nagle, H. Yersin, *Inorg. Chem.* **1997**, 36, 3040.
- 87 W. J. Finkenzeller, P. Stössel, H. Yersin, *Chem. Phys. Lett.* **2004**, 397, 289.
- 88 R. Czerwieńiec, A. Strasser, A. Starukhin, T. Hofbeck, A. Wedel, W. Finkenzeller, H. Yersin, submitted, First results have been presented at the SPIE Optics and Photonics, Conference 5937, San Diego (USA), August, **2005**.
- 89 A. Vogler, H. Nikol, *Comments Inorg. Chem.* **1993**, 14, 245.
- 90 G. Blasse, *Progr. Solid State Chem.* **1988**, 18, 79.
- 91 A. Vogler, H. Kunkely, *Top. Curr. Chem.* **2001**, 213, 143.
- 92 G. H. Dieke, *Spectra and Energy Levels of Rare Earth Ions in Crystals*, Interscience Publishers, New York, **1968**.
- 93 D. R. Gamelin, H. U. Güdel, *Top. Curr. Chem.* **2001**, 214, 1.
- 94 H. Yersin, D. Trümbach, J. Strasser, H. H. Patterson, Z. Assefa, *Inorg. Chem.* **1998**, 37, 3209.
- 95 Z.-Q. Bian, C.-H. Huang, this volume, pp. 391.
- 96 J. Yu, L. Zhou, H. Zhang, Y. Zheng, H. Li, R. Deng, Z. Peng, Z. Li, *Inorg. Chem.* **2005**, 44, 1611.
- 97 P. Kiliuk, C. A. Moore, *Phys. Rev.* **1967**, 160, 307.
- 98 B. Henderson, G. F. Imbusch, *Optical Spectroscopy of Inorganic Solids*, Oxford Science Publ., Clarendon Press, Oxford, **1989**.
- 99 G. B. Porter, H. L. Schäfer, *Z. Phys. Chem. (NF)* **1963**, 37, 109.

- 100 R. Dingle, *J. Chem. Phys.* **1969**, *50*, 1952.
- 101 H. Yersin, P. Huber, G. Gietl, D. Trümbach, *Chem. Phys. Lett.* **1992**, *199*, 1.
- 102 M. Wrighton, D. Ginley, *Chem. Phys.* **1974**, *4*, 295.
- 103 G. A. Crosby, *Acc. Chem. Res.* **1975**, *8*, 231.
- 104 H. Yersin, H. Otto, J. I. Zink, G. Gliemann, *J. Am. Chem. Soc.* **1980**, *102*, 951.
- 105 W. Tuszynski, G. Gliemann, *Z. Naturforsch.* **1979**, *34a*, 211.
- 106 F. A. Cotton, G. Wilkinson, *Anorganische Chemie*, Verlag Chemie, Weinheim, **1980**.
- 107 D. F. Shriver, P. W. Atkins, C. H. Langford, *Inorganic Chemistry*, Oxford University Press, Oxford, **1991**.
- 108 H. L. Schläfer, G. Gliemann, *Einführung in die Ligandenfeldtheorie*, Akademische Verlagsgesellschaft Frankfurt/Main, **1967**.
- 109 C. J. Ballhausen, *Molecular Electronic Structures of Transition Metal Complexes*, McGraw-Hill, New York, **1979**.
- 110 A. Gilbert, J. Baggot, *Essentials of Molecular Photochemistry*, Blackwell Scientific Publications, Oxford, **1991**.
- 111 R. Czerwieniec, W. Finkenzeller, T. Hofbeck, X. H. Yang, D. Neher, A. Starukhin, A. Wedel, H. Yersin, XXII International Conference on Organometallic Chemistry, Zaragoza, Spain Vol. 2, p. 882, **2006**.
- 112 F. Li, M. Zhang, G. Cheng, J. Feng, Y. Zhao, Y. Ma, S. Liu, J. Shen, *Appl. Phys. Lett.* **2004**, *84*, 148.
- 113 J. Breu, P. Stößel, S. Schrader, A. Starukhin, W. J. Finkenzeller, H. Yersin, *Chem. Mater.* **2005**, *17*, 1745.
- 114 H. Yersin, W. Humbs, *Inorg. Chem.* **1999**, *38*, 5820.
- 115 W. J. Finkenzeller, H. Yersin, *Chem. Phys. Lett.* **2003**, *337*, 299.
- 116 P. J. Hay, *J. Phys. Chem. A* **2002**, *106*, 1634.
- 117 A. Ceulemans, L. G. Vanquickenborne, *J. Am. Chem. Soc.* **1981**, *103*, 2238.
- 118 E. M. Kober, T. J. Meyer, *Inorg. Chem.* **1982**, *21*, 3967.
- 119 K. Pierloot, A. Ceulemans, M. Merchán, L. Serrano-Andrés, *J. Phys. Chem. A* **2000**, *104*, 4374.
- 120 Z. Abedin-Siddique, Y. Yamamoto, T. Ohno, K. Nozaki, *Inorg. Chem.* **2003**, *42*, 6366.
- 121 L. Yang, A.-M. Ren, J.-K. Feng, X.-D. Liu, Y.-G. Ma, H.-X. Zhang, *Inorg. Chem.* **2004**, *43*, 5961.
- 122 S. Obara, M. Itabashi, F. Okuda, S. Tamaki, Y. Tanabe, Y. Ishii, K. Nozaki, M. Haga, *Inorg. Chem.* **2006**, *45*, 8907.
- 123 E. Jansson, B. Minaev, S. Schrader, H. Ågren, *Chem. Phys.* **2007**, *333*, 157.
- 124 K. Nozaki, *J. Chinese Chem. Soc.* **2006**, *53*, 101.
- 125 K. Nozaki, K. Takamori, Y. Nakatsugawa, T. Ohno, *Inorg. Chem.* **2006**, *45*, 6161.
- 126 M.-F. Charlot, Y. Pellegrin, A. Quaranta, W. Leibl, A. Aukauloo, *Chem. Eur. J.* **2006**, *12*, 796.
- 127 T. Liu, B.-H. Xia, X. Zhou, H.-X. Zhang, Q.-J. Pan, J.-S. Gao, *Organometallics* **2007**, *26*, 143.
- 128 A. V. Vlček, S. Zláliš, *Coord. Chem. Rev.* **2007**, *251*, 258.
- 129 M. G. Colombo, A. Hauser, H. U. Güdel, *Inorg. Chem.* **1993**, *32*, 3088.
- 130 M. G. Colombo, T. C. Brunold, T. Riedener, H. U. Güdel, M. Förtsch, H.-B. Bürgi, *Inorg. Chem.* **1994**, *33*, 545.
- 131 M. G. Colombo, A. Hauser, H. U. Güdel, *Top. Curr. Chem.* **1994**, *171*, 143.
- 132 G. Calzaferri, R. Rytz, *J. Phys. Chem.* **1995**, *99*, 12141.
- 133 P. I. Djurovich, M. E. Thompson, this volume, pp. 131.
- 134 Z. Abedin-Siddique, T. Ohno, K. Nozaki, *Inorg. Chem.* **2004**, *43*, 663.
- 135 T. Yutaka, S. Obara, S. Ogawa, K. Nozaki, N. Ikeda, T. Ohno, Y. Ishii, K. Sakai, M. Haga, *Inorg. Chem.* **2005**, *44*, 4737.
- 136 H. Miki, M. Shimada, T. Azumi, J. A. Brozik, G. A. Crosby, *J. Phys. Chem.* **1993**, *97*, 11175.
- 137 A. Szabo, N.S. Ostlund, *Modern Quantum Chemistry*, McGraw-Hill, **1989**.
- 138 J. Westra, M. Glasbeek, *Chem. Phys. Lett.* **1991**, *180*, 41.
- 139 M. Glasbeek, R. Sitters, E. van Veldhoven, A. von Zelewsky, W. Humbs, H. Yersin, *Inorg. Chem.* **1998**, *37*, 5159.

- 140 D. Donges, J. K. Nagle, H. Yersin, *J. Luminescence* **1997**, 72–74, 658.
- 141 H. Yersin, D. Donges, W. Humbs, J. Strasser, R. Sitters, M. Glasbeek, *Inorg. Chem.* **2002**, 41, 4915.
- 142 K. P. Balashev, D. Donges, P. C. Ford, W. Humbs, M. M. Mdeleleni, J. Strasser, H. Yersin, *12th International Symposium on the Photochemistry and Photophysics of Coordination Compounds*, Vermont, USA, Book of Abstracts, P 97, **1997**.
- 143 H. Yersin, A. F. Rausch, P. I. Djurovich, M. E. Thompson, *SPIE Optics and Photonics*, San Diego, USA, August, **2007**.
- 144 H. Wiedenhofer, S. Schützenmeier, A. von Zelewsky, H. Yersin, *J. Phys. Chem.* **1995**, 99, 13385.
- 145 S. W. Lai, C.-M. Che, W. J. Finkenzeller, A. F. Rausch, H. Yersin, submitted.
- 146 C. Kratzer, M. Koulikowa, H. Yersin, *14th International Symposium on the Photo-chemistry and Photophysics of Coordination Compounds*, Veszprém, Hungary, Book of Abstracts p. 83, **2001**.
- 147 W. J. Finkenzeller, T. Hofbeck, M. E. Thompson, H. Yersin, *Inorg. Chem.* **2007**, 46, 5076.
- 148 H. Wiedenhofer, PhD Thesis, Universität Regensburg, **1994**.
- 149 H. Yersin et al., unpublished results.
- 150 D. R. Striplin, G. A. Crosby, *Coord. Chem. Rev.* **2001**, 211, 163.
- 151 H. Yersin, D. Braun, *Chem. Phys. Lett.* **1991**, 179, 85.
- 152 M. Kato, S. Yamauchi, N. Hirota, *Chem. Phys. Lett.* **1989**, 157, 543.
- 153 D. Pentlechner, I. Grau, T. Hofbeck, H. Yersin, *Chem. Phys. Lett.*, submitted.
- 154 T. Fischer, R. Bauer, R. Fortte, J. Schwaiger, J. Kroeber, M. Holbach, H. Vestweber, H. Yersin, in preparation.
- 155 H. Backert, Diplomarbeit, Universität Regensburg, **1996**.
- 156 H. Yersin, E. Gallhuber, G. Hensler, *Chem. Phys. Lett.* **1987**, 140, 157.
- 157 A. Juris, V. Balzani, F. Barigelletti, S. Campagna, P. Belser, A. von Zelewsky, *Coord. Chem. Rev.* **1988**, 84, 85.
- 158 C. Daul, E. J. Baerends, P. Vernooijs, *Inorg. Chem.* **1994**, 33, 3538.
- 159 E. M. Kober, T. J. Meyer, *Inorg. Chem.* **1984**, 23, 3877.
- 160 T. Ziegler, J. K. Nagle, J. G. Snijders, E. J. Baerends, *J. Am. Chem. Soc.* **1989**, 111, 5631.
- 161 T. Schönherr, private communication about angular overlap model calculations, University of Düsseldorf, **2007**.
- 162 H. Yersin, S. Schützenmeier, H. Wiedenhofer, A. von Zelewsky, *J. Phys. Chem.* **1993**, 97, 13496.
- 163 J. Schmidt, H. Wiedenhofer, A. von Zelewsky, H. Yersin, *J. Phys. Chem.* **1995**, 99, 226.
- 164 J. N. Demas, B. A. De Graff, *Coord. Chem. Rev.* **2001**, 211, 317.
- 165 H. Yersin, P. Huber, H. Wiedenhofer, *Coord. Chem. Rev.* **1994**, 132, 35.
- 166 D. Braun, P. Huber, J. Wudy, J. Schmidt, H. Yersin, *J. Phys. Chem.* **1994**, 98, 8044.
- 167 P. Huber, H. Yersin, *J. Phys. Chem.* **1993**, 97, 12705.
- 168 M. Cocchi, V. Fattori, D. Virgili, C. Sabatini, P. DiMarco, M. Maestri, J. Kalinowski, *Appl. Phys. Lett.* **2004**, 84, 1052.
- 169 M. Cocchi, D. Virgili, C. Sabatini, V. Fattori, P. DiMarco, M. Maestri, J. Kalinowski, *Synth. Met.* **2004**, 147, 253.
- 170 S. Lamansky, R. C. Kwong, M. Nugent, P. I. Djurovich, M. E. Thompson, *Organic Electronics* **2001**, 2, 53.
- 171 S. Bonafede, M. Ciano, F. Bolletta, V. Balzani, L. Chassot, A. von Zelewsky, *J. Phys. Chem.* **1986**, 90, 3836.
- 172 M. Maestri, D. Sandrini, V. Balzani, L. Chassot, P. Jolliet, A. von Zelewsky, *Chem. Phys. Lett.* **1985**, 122, 375.
- 173 V. Balzani, M. Maestri, A. Melandri, D. Sandrini, L. Chassot, C. Cornioley-Deuschel, P. Jolliet, U. Maeder, A. von Zelewsky, In: H. Yersin, A. Vogler (Eds.), *Photochemistry and Photophysics*, Springer-Verlag, Berlin, **1987**.
- 174 M. Maestri, V. Balzani, C. Deuschel-Cornioley, A. von Zelewsky, *Adv. Photochem.* **1992**, 17, 1.
- 175 E. V. Shpol'skii, *Sov. Phys. Usp. (Engl. Transl.)* **1960**, 3, 372.
- 176 Ph. Garrigues, H. Budzinski, *Trends Anal. Chem.* **1995**, 14, 231.

- 177 H. Yersin, C. Kratzer, *Coord. Chem. Rev.* **2002**, 229, 75.
- 178 J. Breu, K.-J. Range, A. von Zelewsky, H. Yersin, *Acta Crystallogr. C* **53**, 562, 1997.
- 179 R. N. Nurmukhametov, *Russian Chemical Reviews* **1969**, 38, 180.
- 180 J. A. Salthouse, M. J. Ware, *Point group character tables and related data*, Cambridge University Press, London.
- 181 R. W. Harrigan, G. A. Crosby, *J. Chem. Phys.* **1973**, 59, 3468.
- 182 J. Strasser, H. H. H. Homeier, H. Yersin, *Chem. Phys.* **2000**, 255, 301.
- 183 D. R. Striplin, G. A. Crosby, *Chem. Phys. Lett.* **1994**, 221, 426.
- 184 T. Azumi, C. M. O'Donnel, S. P. McGlynn, *J. Chem. Phys.* **1966**, 45, 2735.
- 185 H. Yersin, J. Strasser, *Coord. Chem. Rev.* **2000**, 208, 331.
- 186 T. Hofbeck, PhD thesis, Universität Regensburg; in preparation.
- 187 K. Dedeian, P. I. Djurovich, F. O. Garces, G. Carlson, R. J. Watts, *Inorg. Chem.* **1991**, 30, 1685.
- 188 K. A. King, P. J. Spellane, R. J. Watts, *J. Am. Chem. Soc.* **1985**, 107, 1431.
- 189 M. G. Colombo, T. C. Brunhold, T. Riedener, H. U. Güdel, M. Förtsch, H.-B. Bürgi, *Inorg. Chem.* **1994**, 33, 545.
- 190 I. Waller, *Z. f. Physik* **1932**, 79, 370.
- 191 R. L. de Kronig, *Physica* **1939**, 6, 33.
- 192 J. H. van Vleck, *Phys. Rev.* **1940**, 57, 426.
- 193 P. L. Scott, C. D. Jeffries, *Phys. Rev.* **1962**, 127, 32.
- 194 A. A. Manenkov, R. Orbach, *Spin-Lattice-Relaxation in Ionic Solids*, Harper & Row, New York, **1966**.
- 195 A. Abragam, B. Bleaney, *Electron Paramagnetic Resonance of Transition Ions*, Clarendon Press, Oxford, **1970**.
- 196 M. B. Walker, *Can. J. Phys.* **1968**, 46, 1347.
- 197 M. B. Walker, *Phys. Rev. Lett.* **1967**, 162, 199.
- 198 R. Orbach, M. Blume, *Phys. Rev. Lett.* **1962**, 8, 478.
- 199 V. A. Andreev, Y. I. Prilutskii, *Phys. Solid State* **1993**, 35, 1624.
- 200 V. A. Andreev, Y. I. Prilutskii, *Sov. Phys. Solid State (engl. Translation)* **1992**, 34, 1178.
- 201 H. H. H. Homeier, J. Strasser, H. Yersin, *Chem. Phys. Lett.* **2000**, 316, 280.
- 202 T. Hofbeck, Diplomarbeit, Universität Regensburg, **2007**.
- 203 W. J. Finkenzeller, M. E. Thompson, H. Yersin, *Chem. Phys. Lett.* **2007**, 444, 273.
- 204 A. Rausch, T. Hofbeck, W. J. Finkenzeller, M. E. Thompson, H. Yersin, in preparation.
- 205 E. Gallhuber, G. Hensler, H. Yersin, *J. Am. Chem. Soc.* **1987**, 109, 4818.
- 206 D. Braun, G. Hensler, E. Gallhuber, H. Yersin, *J. Phys. Chem.* **1991**, 95, 1067.
- 207 H. Yersin, C. Kratzer, *Chem. Phys. Lett.* **2002**, 362, 365.
- 208 G. Gliemann, *Comments Inorg. Chem.* **1986**, 5, 263.
- 209 G. Gliemann, 31st International Congress Pure Applied Chemistry (Proceedings) Sofia, Bulgaria, Pergamon Press, Oxford, p. 11, **1987**.
- 210 D. C. Baker, G. A. Crosby, *Chem. Phys.* **1974**, 4, 428.
- 211 G. A. Crosby, K. R. Kendrick, *Coord. Chem. Rev.* **1998**, 171, 407.
- 212 N. van Dijk, M. Noort, S. Voelker, G. W. Canters, J. H. Van der Waals, *Chem. Phys. Lett.* **1980**, 71, 415.
- 213 W.-H. Chen, K. E. Rieckhoff, E.-M. Voigt, *Molecular Physics* **1987**, 62, 541.
- 214 A. Zilian, H. U. Güdel, *J. Luminescence* **1992**, 51, 237.
- 215 A. P. Marchetti, J. C. Deaton, R. H. Young, *J. Phys. Chem. A* **2006**, 110, 9828.
- 216 Y. Kawamura, K. Goushi, J. Brooks, J. J. Brown, H. Sasabe, C. Adachi, *Appl. Phys. Lett.* **2005**, 86, 071104.
- 217 A. Tsuboyama, H. Iwawaki, M. Furugori, T. Mukaide, J. Kamatani, S. Igawa, T. Moriyama, S. Miura, T. Takiguchi, S. Okada, M. Hoshino, K. Ueno, *J. Am. Chem. Soc.* **2003**, 125, 12971.
- 218 I. Tanaka, Y. Tabata, S. Tokito, *Jap. J. Appl. Phys.* **2004**, 43, L1601.
- 219 J. Thompson, V. Arima, F. Matino, S. Berkebile, G. Koller, F. P. Netzer, M. G. Ramsey, R. Cingolani, R. I. R. Blyth, *Synth. Met.* **2005**, 153, 233.
- 220 N. R. Evans, L. S. Devi, C. S. K. Mak, S. E. Watkins, S. I. Pascu, A. Köhler, R. H. Friend, C. K. Williams, A. B. Holmes, *J. Am. Chem. Soc.* **2006**, 128, 6647.

- 221 Y. Kawamura, J. Brooks, J. J. Brown, H. Sasabe, C. Adachi, *Phys. Rev. Lett.* **2006**, *96*, 17404.
- 222 M. Sudhakar, P. I. Djurovich, T. E. Hogen-Esch, M. E. Thompson, *J. Am. Chem. Soc.* **2003**, *125*, 7796.
- 223 B. W. D'Andrade, M. E. Thompson, S. R. Forrest, *Adv. Mater.* **2002**, *14*, 147.
- 224 S. Tokito, T. Iijima, T. Tsuzuki, F. Sato, *Appl. Phys. Lett.* **2003**, *83*, 2459.
- 225 V. Maiorano, E. Perrone, S. Carallo, A. Biasco, P. P. Pompa, R. Cingolani, A. Croce, R. I. R. Blyth, J. Thompson, *Synth. Met.* **2005**, *151*, 147.
- 226 J.-H. Jou, M.-C. Sun, H.-H. Chou, C.-H. Li, *Appl. Phys. Lett.* **2005**, *87*, 043508.
- 227 S. Lamansky, P. I. Djurovich, D. Murphy, F. Abdel-Razzaq, H.-E. Lee, C. Adachi, P. E. Burrows, S. R. Forrest, M. E. Thompson, *J. Am. Chem. Soc.* **2001**, *123*, 4304.
- 228 F.-C. Chen, Y. Yang, M. E. Thompson, J. Kido, *Appl. Phys. Lett.* **2003**, *80*, 2308.
- 229 C. Adachi, M. A. Baldo, S. R. Forrest, S. Lamansky, M. E. Thompson, R. C. Kwong, *Appl. Phys. Lett.* **2001**, *78*, 1622.
- 230 S. Lamansky, P. I. Djurovich, F. Abdel-Razzaq, S. Garon, D. Murphy, M. E. Thompson, *J. Appl. Phys.* **2002**, *92*, 1570.
- 231 D. G. Moon, R. B. Pode, C. J. Lee, J. I. Han, *Mater. Sci. Eng. B* **2005**, *121*, 232.
- 232 F.-C. Chen, S.-C. Chang, G. He, S. Pyo, Y. Yang, M. Kurotaki, J. Kido, *J. Pol. Sci. B* **2003**, *41*, 2681.
- 233 S. Tokito, M. Suzuki, F. Sato, M. Kamachi, S. Shirane, *Org. Electr.* **2003**, *4*, 105.
- 234 X. Chen, J.-L. Liao, Y. Liang, M. O. Ahmed, H.-E. Tseng, S.-A. Chen, *J. Am. Chem. Soc.* **2003**, *125*, 636.
- 235 S. Tokito, M. Suzuki, F. Sato, *Thin Solid Films* **2003**, *445*, 353.
- 236 A. J. Sandee, C. K. Williams, N. R. Evans, J. E. Davies, C. E. Boothby, A. Köhler, R. H. Friend, A. B. Holmes, *J. Am. Chem. Soc.* **2004**, *126*, 7041.
- 237 T. C. Brunhold, H. U. Güdel, in: E. I. Solomon, A. B. P. Lever (Eds.), *Inorganic Electronic Structure and Spectroscopy*, Wiley, Vol. 1, 259, **1999**.
- 238 E. I. Solomon, *Comments Inorg. Chem.* **1984**, *3*, 225.
- 239 A. C. Albrecht, *J. Chem. Phys.* **1963**, *38*, 358.
- 240 G. Fischer, *Vibronic Coupling*, Academic Press, London, **1984**.
- 241 C. D. Flint (Ed.), *Vibronic Processes in Inorganic Chemistry*, NATO ASI Series C, Vol. 288, Kluwer Academic Publishers, Dordrecht, **1989**.
- 242 R. M. Hochstrasser, *Molecular Aspects of Symmetry*, Benjamin Inc., WA, New York, Amsterdam, **1966**.
- 243 N. Mataga, T. Kubota, *Molecular Interactions and Electronic Spectra*. Marcel Decker Inc., New York, **1970**.
- 244 D. Becker-Donges, H. Yersin, A. von Zelewsky, *Chem. Phys. Lett.* **1995**, *235*, 490.
- 245 J. Schmidt, J. Strasser, H. Yersin, *Inorg. Chem.* **1997**, *36*, 3957.
- 246 W. Finkenzeller, PhD Thesis, Universität Regensburg, in preparation.
- 247 L. Bär, G. Gliemann, *Chem. Phys. Lett.* **1984**, *108*, 14.
- 248 R. Dillinger, G. Gliemann, *Chem. Phys. Lett.* **1985**, *122*, 66.
- 249 G. Gliemann, H. Yersin, *Structure and Bonding*, Springer Berlin, *62*, 87, **1985**.
- 250 T.-H. Huang, K. E. Rieckhoff, E. M. Voigt, *Chem. Phys.* **1979**, *36*, 423.
- 251 T.-H. Huang, K. E. Rieckhoff, E. M. Voigt, *J. Chem. Phys.* **1982**, *77*, 3424.
- 252 D. Braun, H. Yersin, *Inorg. Chem.* **1995**, *34*, 1967.
- 253 J. Breu, C. Kratzer, H. Yersin, *J. Am. Chem. Soc.* **2000**, *122*, 2548.
- 254 R. Bauer, W. J. Finkenzeller, U. Bogner, M. E. Thompson, H. Yersin, submitted.
- 255 I. Renge, *J. Phys. Chem. A* **2001**, *105*, 9094.
- 256 W. M. Yen, P. M. Selzer (Eds.), *Laser Spectroscopy of Solids*, Springer Berlin, Topics in Applied Physics, Vol. 49, **1981**.
- 257 R. I. Personov, in: V. R. Agronovich, R. M. Hochstrasser (Eds.), *Spectroscopy and Excitation Dynamics of Condensed Molecular Systems*, North Holland, Amsterdam, p. 555, **1983**.
- 258 W. E. Moerner (Ed.), *Persistent Spectral Hole Burning: Science and Applications*, Springer, Berlin, **1988**.

- 259** K. K. Rebane, in: O. Sild, K. Haller (Eds.), *Zero-Phonon Lines and Spectral Hole Burning in Spectroscopy and Photochemistry*, Springer, Berlin, **1988**.
- 260** H. Riesen, *Coord. Chem. Rev.* **2006**, *250*, 1737.
- 261** W. H. Hesselring, D. A. Wiersma, *J. Chem. Phys.* **1980**, *73*, 648.
- 262** D. E. McCumber, M. D. Sturge, *J. Appl. Phys.* **1963**, *34*, 1682.

